INFORMATION TO USERS

This manuscript has been reproduced from the microfilm master. UMI films the text directly from the original or copy submitted. Thus, some thesis and dissertation copies are in typewriter face, while others may be from any type of computer printer.

The quality of this reproduction is dependent upon the quality of the copy submitted. Broken or indistinct print, colored or poor quality illustrations and photographs, print bleedthrough, substandard margins, and improper alignment can adversely affect reproduction.

In the unlikely event that the author did not send UMI a complete manuscript and there are missing pages, these will be noted. Also, if unauthorized copyright material had to be removed, a note will indicate the deletion.

Oversize materials (e.g., maps, drawings, charts) are reproduced by sectioning the original, beginning at the upper left-hand corner and continuing from left to right in equal sections with small overlaps.

Photographs included in the original manuscript have been reproduced xerographically in this copy. Higher quality 6" x 9" black and white photographic prints are available for any photographs or illustrations appearing in this copy for an additional charge. Contact UMI directly to order.

Bell & Howell Information and Learning
300 North Zeeb Road, Ann Arbor, MI 48106-1346 USA
800-521-0600

UMI®

OBSERVATIONS OF BLACK HOLE CANDIDATE GRS 1758–258 BY THE *GRATIS* BALLOON-BORNE TELESCOPE AND OTHER OBSERVATORIES

John William Keck

Submitted in partial fulfillment of the
requirements for the degree
of Doctor of Philosophy
in the Graduate School of Arts and Sciences.

COLUMBIA UNIVERSITY

2001

Bell & Howell Information and Learning Company
300 North Zeeb Road
P.O. Box 1346
Ann Arbor, MI 48106-1346

Abstract

OBSERVATIONS OF BLACK HOLE CANDIDATE
GRS 1758–258
BY THE
GRATIS BALLOON-BORNE TELESCOPE
AND OTHER OBSERVATORIES

John William Keck

The Gamma Ray Arcminute Telescope Imaging System (*GRATIS*) was flown from Alice Springs, Australia on October 17–18, 1995. The experiment consists of 35 individual one-dimensional coded-aperture telescopes with a field of view of 40 arcminutes in the imaging direction.

We review the basic design of *GRATIS*, concentrating on the electronics critical to data acquisition.

We survey the origins and types of background radiation that contaminate the data of *GRATIS*. We review previous work attempting to characterize the atmospheric gamma-ray background and combine the most dependable experimental results to model it. We calculate approximate magnitudes for all background components, and give the results of Monte Carlo simulations of the cosmic diffuse and atmospheric components using the COG radiation transport package.

Finally, we combine *GRATIS* data with previously published and archival data from *GRANAT*, *ROSAT*, *CGRO*, *RXTE*, *BeppoSAX*, *ASCA*, and the VLA to produce a long-term multi-wavelength light curve of Galactic black hole candidate GRS 1758–258. In light of divergent analyses of the 1991–1993 *ROSAT* observations, we have re-analyzed these data; we find the soft x-rays track the hard x-rays, and that the fits require no black-body component— indicating that GRS 1758–258 did not go to the high state in 1993. We offer two standard corona-disk interpretations of the emission and an interpretation based on the ADAF model for a system with $\dot{m} \lesssim \dot{m}_{\rm crit}$. We find the 1990–1993 co-eval hard and soft observations support the ADAF predictions. We discuss a new way to constrain black-hole mass with spectral data and the ADAF theory, and apply this technique to GRS 1758–258 to find $M_{\rm BH} \gtrsim 8 - 9\ M_{\odot}$ at an assumed distance of 8.5 kpc.

Further investigations of the ADAF model allow us to critically evaluate the model against the data and flux-flux diagram of Barret, McClintock, & Grindlay (1996) and to understand the limits of the latter's "X-ray burster box."

Contents

List of Tables vi

List of Figures ix

Acknowledgements xi

1 Introduction 1

1.1 Origins of Astrophysics 2

1.2 Overview of Dissertation 7

I *GRATIS* 8

2 Overview of *GRATIS* 9

2.1 Mechanical Assembly 10

2.2 Aspect and gondola control 12

2.3 Telescope Overview 14

2.4 Detectors 16

2.5 Data-acquisition Electronics 18

2.5.1 Scaler Event 23

2.5.2 Gamma-ray Event 25

2.5.3 LED Events 27

2.5.4 Other Kinds of Events 30

2.5.5 Data Pipeline 33
2.6 Calibration and Response Matrix 35
2.7 Outstanding Issues in Data Acquisition 40

3 Background modeling **44**
3.1 Types of background radiation 45
3.2 Cosmic-ray dependencies 48
3.3 Source function construction 53
3.3.1 Cosmic Diffuse Background 53
3.3.2 Atmospheric gamma-rays 55
Downward flux 58
Upward Flux 60
Horizontal Flux 62
Empirical Model 64
3.4 *GRATIS* Background Estimation 66
3.4.1 Diffuse Background 67
Cosmic Diffuse Background 67
Results 69
Galactic Diffuse Background 73
3.4.2 Atmospheric gamma-rays 75
Downward: $0° < \theta < 40°$ 76
Horizontal: $40° < \theta < 110°$ 77
Upward: $110° < \theta < 180°$ 79
Results 80
3.4.3 Locally produced photons 86
3.4.4 Neutron-induced background 89

3.4.5 Crystal activation 91
3.4.6 Summary 95
3.4.7 Possible improvements 97

II GRS 1758–258 **99**

4 Observations **102**
4.1 *GRATIS* 104
4.2 *GRANAT* 109
4.3 *ROSAT* 110
4.4 *CGRO* 117
4.5 *RXTE* 119
4.6 *BeppoSAX* 121
4.7 *Exosat* 122
4.8 Other X-ray Data 123
4.9 VLA 125

5 Results **130**
5.1 The Phenomenology of Black Holes 130
5.2 Black-body temperatures 133
5.3 High- and Low-energy Fluxes & Flux-Flux Diagram 135
5.4 Spectral Intensity and Shape 136
5.5 Timing Analysis 139
5.6 Radio and X-ray 141

6 Discussion **145**

6.1 Comptonizing Donut Model 146
6.2 Partial Disk Corona 149
6.3 Advection-Dominated Accretion Flow 151
6.4 Further Inquiries with the ADAF Model 160
6.5 Conclusion 167

References **170**

A Monte Carlo Simulations **188**
A.1 The COG version of *GRATIS* 189

List of Tables

2.1 Manifest of CAMAC modules and slot assignments 21

2.2 List processor triggers 22

2.3 Scaler triggers and registers 23

2.4 Event-type codes 24

2.5 Results of COG simulations of CsI crystal with indicated dead-layer thickness. 37

2.6 Results of 1995 alignment and shadow-mask calibrations 38

2.7 Results of Alignment '95 39

3.1 Parameters of the Empirical Atmospheric Model. 65

3.2 Results of cosmic diffuse Monte Carlo. 73

3.3 Results of atmospheric gamma-ray Monte Carlo. 82

3.4 Parameters of the time-dependent decay function $R(t)$. 93

3.5 Components of *GRATIS* background 95

4.1 Miscellaneous data points in figure 4.1 104

4.2 Unabsorbed 1.0–2.4 keV Fluxes from *ROSAT* 115

4.3 Previously Published VLA 6-cm data points 126

4.4 VLA data points 128

4.5 VLA Map Specifications 129

4.6 Other Sources in Radio Field 129

5.1 Black-body temperatures 134

List of Figures

2.1 Top and side views of the *GRATIS* payload taken from early drawings. 11

2.2 A schematic cross section of the *GRATIS* telescope (lying on its side). 11

2.3 The *GRATIS* payload in the high bay at Nevis 13

2.4 *Left:* Schematic view of the mask-plane of *GRATIS*. *Right:* The *GRATIS* mask pattern 15

2.5 *Left:* Coarse collimator response. *Right:* Fine collimator response. . . 16

2.6 Gamma-ray data acquisition schematic, from Keck *et al.* (1996). . . . 20

2.7 Decoding scaler event data 24

2.8 Decoding gamma-ray event data 27

2.9 *GRATIS* timing and logic after Alice Springs modifications 28

2.10 Gamma-ray event timing 29

2.11 ULD event timing 29

2.12 Decoding LED event data 30

2.13 Drift of 10-kHz clock for the Alice Springs flight. 31

2.14 *GRATIS* response matrix 40

2.15 *GRATIS* effective area 41

2.16 Telescope temperatures during the flight Alice Springs in October 1995. 43

3.1 Types of background radiation. 46

3.2 Trajectory-derived Effective Vertical Cutoff Rigidities for Epoch 1975.0 from Shea & Smart (1975) 51

3.3 Slant-depth factors compared to numerical integration of simple atmospheric model, cf. Zombeck (1990), p. 229. 56

3.4 Upward atmospheric gamma ray model compared to Imhof *et al.* (1976) and Ryan *et al.* (1977). 61

3.5 Comparison of present model's angular distribution to data of Ryan *et al.* (1977) and Schönfelder *et al.* (1977). 66

3.6 The mysterious *GRATIS* background spectrum. 67

3.7 Zenith-angular distribution of Monte Carlo-produced cosmic diffuse background photons for $E > 7$ keV. 69

3.8 Contour plot of distribution of Monte Carlo-produced cosmic diffuse background photons in zenith angle and energy. 70

3.9 Monte Carlo simulated PHA spectra from cosmic diffuse photons. . . 72

3.10 Zenith-angular distribution of Monte Carlo-produced atmospheric background photons for 40 keV $< E <$ 100 MeV. 81

3.11 Contour plot of the intensity distribution of Monte Carlo-produced atmospheric background photons in zenith angle and energy. 82

3.12 Monte-Carlo predicted angular distributions of the detected atmospheric photons. 84

3.13 Atmospheric gamma-ray spectra from the two tubes. 85

3.14 Background matrices of the two tubes. 86

3.15 Comparison of Monte-Carlo calculated atmospheric background to observed background spectrum 96

4.1 GRS 1758–258 lightcurve and spectral index history, 1985–2000. . . . 103

4.2 Raw count rate for GRS 1758–258 from *GRATIS* data. 106

4.3 Unfolded spectrum for GRS 1758–258 from *GRATIS* data. 108

4.4 PSPC image plane. Extracted regions for source and background are circled. 113

4.5 Confidence contours for fits to March 1993 *ROSAT*/PSP C data: *left* power-law fit; *right* black-body fit. 115

4.6 Unfolded spectrum from power-law fit to *ROSAT* data. 115

4.7 Unfolded spectra for 10–11 April 1997 *BeppoSAX* observation. 122

4.8 Maps from VLA observations sensitive to broad spatial frequencies. . 127

5.1 Barret, McClintock, and Grindlay-Style flux-flux diagram for GRS 1758–258 at an assumed distance of 8.5 kpc. 136

5.2 Hardness ratio *vs.* total count rate for 1990-2000 BATSE data. 138

5.3 Power spectra for 1992 and 1993 *ROSAT*/PSPC observations. 140

5.4 Radio/hard X-ray flux-flux diagram. 142

5.5 Putative bursts in radio data for Cyg X-1 and GRS 1758—258. 144

6.1 Schematic cross-sectional diagrams of two-temperature model and disk corona model. 146

6.2 ADAF model states 153

6.3 Results of the simple calculation of the multiplicative factor for the 1997 model. 158

6.4 BMG's original plot but with black holes normalized by mass. ADAF models overplotted 163

6.5 BMG's plot for GX 339–4 with overlaid ADAF models. 165

6.6 BMG's plot for Nova Muscae 1991 with overlaid ADAF models 166

A.1 Cross-sectional views of COG model of *GRATIS* tube shielding and fine collimator assembly. 190

Acknowledgments

Special thanks goes to my advisors, official and unofficial, Chuck Hailey and Bill Craig, and brother-in-arms Jaesub Hong. Thanks also goes to other people in the *GRATIS* collaboration: Irwin Rochwarger, Klaus Ziock, Dennis Carr, Ryan McLean, Mike Pivovaroff, Ron Wurtz, Fiona Harrison. Additional thanks to committee members Steve Kahn and Elena Aprile for their many helpful comments.

Thanks are also due to others of the *GRATIS* team who remained more or less in the background: Philip M. Lubin, Michael Seiffert, Chris Adams, Todd Decker, Jim Hughes, Greg Sprehn, Leigh Brookshaw, Craig Brooksby, Bob Priest, and Matt Fischer. Thanks to David Helfand for his help negotiating the tortuous AIPS package, and to the National Scientific Ballooning Facility for making the *GRATIS* flight possible.

And to people who have provided me valuable assistance: Rich Buck at Livermore and Richard Friedberg at Columbia. I remain eternally grateful to the Columbia libraries, especially Kathleen Kehoe, without whom I would have been unable to obtain many articles necessary for this research.

Thanks to the NASA Graduate Research Fellowship Program, which funded several years of my work. Thanks also to the NASA Astrophysics Data System Abstract Service, and the High Energy Astrophysics Science Archive Research Center Online Service, provided by the NASA/Goddard Space Flight Center.

The often lonely work of scientists is dependent on so many external factors: the insights of colleagues; a social and intellectual context conducive to science. In astrophysics, we are particularly blest by working in a community, but it handicaps specific citation: there are certainly many others whose unnoticed contributions I appreciate but am unable to name.

And I cannot omit those to whom I owe my existence: gratitude beyond all telling to my parents and

To him that by wisdom made the heavens;
for his mercy endureth for ever.

To Leona,
without whom I would not be here.

Chapter 1

Introduction

IN THE BEGINNING a gusty wind blew over the English countryside. A thoughtful youth sat in the garden of his mother's house when the fruit of a swaying apple tree dropped to the ground with a thud. Young Isaac pondered the fall of the apple and its displacement from the tree: *a wind strong enough could propel a falling body a much farther distance, perhaps even around the earth.* He thought of the moon and the mysterious force that keeps it moving around the earth. His lazy afternoon day-dreaming brought him to the realization that the same force that keeps the moon from flying off into space pulls apples to earth: *gravitation is universal.* The universe is not, as Aristotle had posited, divided into sublunar and translunar realms subject to different laws, but all of creation obeys the same physical laws.

The laws are universal, but terrestrial and celestial realms require approach from different sub-disciplines. While the rest of physics ponders the apple, astrophysics gazes at the moon in an attempt to apply earth-based laws to celestial phenomena, and to discover new universal laws in the special conditions of the heavens.

1.1 Origins of Astrophysics

Astrophysics then is a union of astronomical observations with the explanatory power of physics. Astronomy and astrology (the two words were synonymous as recently as three centuries ago, cf. OED, def. 1a) of course originate before history, when man sought meaning in the brilliant orbs so prominently placed in the vault of the sky. Man's knowledge of the processes governing the physical universe was scarce, so he could do little but observe, record and speculate.

Astronomy waited many centuries for the appearance of modern physics. The Greeks had had elements of modern science, as had the Chinese, the Indians, the Babylonians, the Egyptians, the Aztecs, the Incas, and the Maya, but none had been able to gather their disparate insights into a coherent self-sustaining whole (Jaki, 1990). Then somehow, at the climax of the European middle ages[1], faith began to

[1]That this train of thought long preceded Newton, Descartes, and even Galileo is shown by Jean Buridan's *impetus* theory, which adumbrated inertia, in 1330 (Butterfield, 1957; Hafner, 1996).

penetrate the clouded human intellect: faith in the contingency of the universe as a whole and in the rationality and intelligibility of the laws governing it[2]. This faith had consequences: it meant that the universe around us, being one of an infinite number of possibilities in the mind of God, could not be approached *a priori*, but only *a posteriori*; it meant that, God being the giver of rational laws and man being his son, insights from such investigation could build up into a coherent system of thought. For these assumptions (at least implicitly), men, such as Galileo and Huygens, would lay down their time to conduct tedious experiments, and in return gain the secrets of nature (Jaki, 1990; Hafner, 1996).

Astrophysics awaited the coming of age of physics in the nineteenth and twentieth centuries. Astronomy and physics have always been allied, as the work of Galileo, Newton, and others show, but astro*physics* require an understanding of radiation. The 19th century marked a turning point for astronomy. The field began to shift from measuring the positions and motions of bodies to probing their physical properties. The early 19th century began the investigation of Fraunhofer lines in the solar spectrum. Not everyone was convinced of the usefulness of this investigation. In 1864 distinguished amateur astronomer Admiral W.H. Smyth. commented in print:

[2] "The most incomprehensible thing about the universe is that it is comprehensible." —Albert Einstein

> With all my admiration of the marvelous and extensive power of Chemistry in disintegrating the nature and properties of the elements of matter, I really trust it will not be exerted among the Celestials to the disservice or detriment of measuring agency; and this I hope for the absolute maintenance of GEOMETRY, DYNAMICS and pure ASTRONOMY.

The new astronomy was generally held in low regard by the practitioners of the more traditional astronomy and closely identified with chemistry (Meadows, 1984). Thermodynamics and electromagnetism were key physical insights of the 19th century: the Stefan-Boltzmann law from thermodynamics allowed astronomers to measure the temperature of a star's "surface," and Maxwell's E-M theory explained the origin of light, but neither development was adequate to explain spectra lines, stellar or terrestrial. Christian Doppler discovered the eponymous effect in 1842, and its observation in stellar spectra in the latter part of the century produced a practical payoff to all the muddling around with blindingly faint lines (Motz & Weaver, 1995).

The 20th century brought the formulation of Einstein's theories of relativity, and the development of quantum mechanics. At last those enigmatic lines could be deciphered! In the middle of the century, history intervened to ripen the conditions for the growth of *high-energy* astrophysics.

Politics[3] being the art of doing as you please and making everyone else do what

[3] As lamentably practiced in our fallen world.

you want, politicians naturally tend to indulge their generals. After the spectacular success of the Manhattan Project, physics became the darling of the generals and their politicians. Vast influxes of government money followed, creating an unprecedented jump in the quantity of research possible in fields that had previously been regarded as the idiosyncratic hobbies of a few harmless gentleman.

Until 1945, astronomy was carried out more or less exclusively in the optical wave-band.[4] Since the earth's atmosphere absorbs x-rays and gamma-rays, these energy-bands could not be observed until the development of rockets with enough power to lift scientific payloads above its obscuration. The American acquisition of the German rocket program powered a giant leap in the power of launch vehicles. The first x-ray rocket flights were launched in June 1962 from White Sands Missile Range, New Mexico by Giaconni and collaborators. The rocket, an Aerobee carrying three Geiger counters, allowed only a few minutes of observation before plummeting back below the blanket of the atmosphere. The series of flights that continued into the next year discovered discrete x-ray sources in the Galaxy, for example Sco X-1 (Shapiro & Teukolsky, 1983). Early detections in the 1–10 keV band included the supernova remnant of the Crab Nebula, the radio galaxy M87, and the diffuse x-ray background.(Longair, 1992)

[4]One exception being Karl Jansky's discovery of extraterrestrial radio radiation in 1932.

On 12 December 1970, NASA launched from the coast of Kenya its first x-ray explorer satellite. As December 12 is Kenyan Independence Day, the satellite was nicknamed *Uhuru*, Swahili for "freedom" (Tucker & Giacconi, 1985). *Uhuru* was devoted to x-ray astronomy in the 2–10 keV band. Especially noteworthy among its discoveries is that the variability of some Galactic x-ray sources comes from the x-ray emitter being part of an eclipsing binary and taking matter from its larger partner through accretion.(Longair, 1992)

Uhuru gained an improved position for Cyg X-1, and verified that the source had a variability on the time-scale of weeks. Cyg X-1 is the first dynamically confirmed black hole, which is to say that it is deduced to have a mass above the maximum mass for a neutron star based on observations of the orbit of its companion, in this case the blue supergiant HDE 226868 (Tucker & Giacconi, 1985).

Another landmark x-ray telescope was the Einstein X-ray Observatory (HEAO-B), which NASA launched in November 1978. Its High Resolution Imager (HRI) instrument provided the first high resolution images ($\lesssim 4$ arcmin) of many sources. It discovered x-ray emission from all classes of stars. It also detected x-ray emission from all known classes of active galactic nuclei, including the most distant quasars.(Longair, 1992)

1.2 Overview of Dissertation

In part I we examine issues related to the *GRATIS* instrument. Chapter 2 reviews the basics of the instrument, concentrating especially on the data acquisition electronics. Chapter 3 reviews the forms of radiation that comprise the background signal that dominates the data and estimates the magnitude of their contribution to the *GRATIS* flight.

In part II we explore an astrophysical source, Galactic black-hole candidate GRS 1758–258, observed by *GRATIS* as part of its 17 October 1995 flight. Chapters 4 and 5 examine observations of the source by *GRATIS* and other high-energy missions. Chapter 6 discusses possible interpretations of the data.

Part I

GRATIS

Chapter 2

Overview of *GRATIS*

It is a truism of experimental high-energy astrophysics that gamma-rays ($E >$ 10 keV) cannot be focussed using standard techniques[1]. Without focusing, imaging with these elusive photons in the 20–200 keV (hard x-ray/soft gamma-ray) range presents formidable challenges. The venerable designers of *GRATIS* chose to surmount this obstacle with coded aperture imaging techniques.

Coded aperture imaging involves using a pseudo-random pattern of opaque and transparent sections— in other words a mask— to produce a shadow pattern on a detector: a sort of shadow camera. For the case of *GRATIS*, each of the sub-telescopes produces a one-dimensional image. Each of the 35 co-aligned telescopes is rotated five

[1]The successor to *GRATIS*, *HEFT*, uses a novel multi-layer coating technique to focus photons with $E > 20$ keV.

degrees with respect to its neighbor (cf. figure 2.4). Combining the one-dimensional images from each of the tubes produces a two-dimensional image with a circular field of view 40 arcminutes in diameter and an angular resolution of approximately two arcminutes.

It is this high-resolution imaging ability that drives the design of the entire *GRATIS* payload. In this chapter we first quickly review the mechanical assembly and the aspect control system. Then we turn to the workings of the telescope proper, especially the data acquisition system. Finally we describe some of the short-comings of the performance of *GRATIS* in its 1995 flight.

2.1 Mechanical Assembly

GRATIS consists of the *telescope*, which handles gamma-ray detection and data acquisition, and the *gondola*, which controls aspect and pointing of the telescope. These two sections are electrically isolated from each other.

The *GRATIS* payload, shown in figure 2.1, stands over 17 feet tall and weighs 3400 lbs. Figure 2.2 shows the basic components of the telescope.

Figure 2.1: Top and side views of the *GRATIS* payload taken from early drawings.

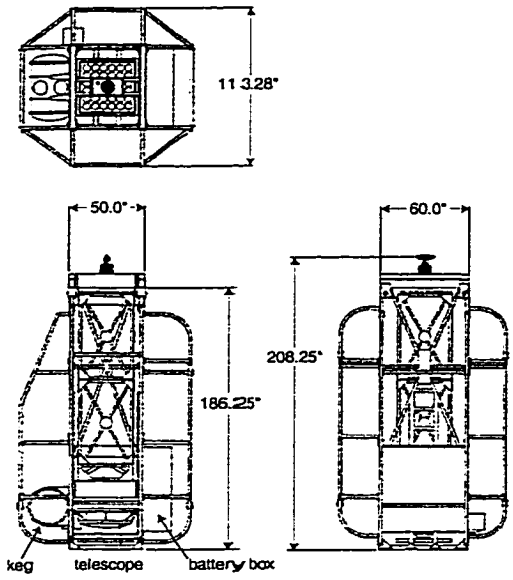

Figure 2.2: A schematic cross section of the *GRATIS* telescope (lying on its side).

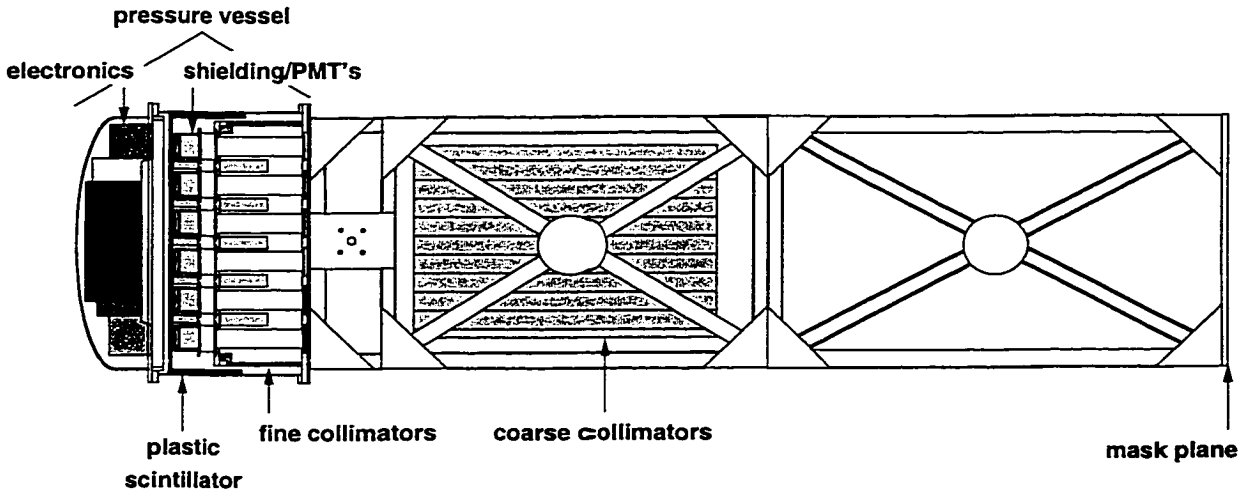

2.2 Aspect and gondola control

Whereas most balloon platforms at best require aspect reconstruction at the 5–10 arcminute level, the two-arcminute resolution of *GRATIS* requires aspect reconstruction at the 10–20 arc*second* level.

There are two sides to the aspect solution. Keeping the target within the field of view requires knowing the aspect at the arcminute level in real-time. Correcting the photons for imaging requires the full 10–20 arcsecond aspect reconstruction (after the fact).

A three-axis fiber-optic gyroscope (FOG) is the primary instrument for aspect determination. The FOG has 0.1-arcsecond resolution, $\sim$ 2-arcsecond noise, and potential drift rate of better than 0.1 degrees per hour. But even with a drift rate far less than the $\sim 1°/\mathrm{hr}$ of a mechanical gyroscope, the FOG requires periodic external correction. Two separate sets of systems provide this correction along the three rotational axes (viz. azimuth, elevation, and roll). A GPS-based attitude determination system corrects azimuthal drift, along with input from dual magnetometers. On the elevation axis, an encoder gives the telescope's position with respect to the gondola, and inclinometers give the gondola's position with respect to the vertical to enable

drift correction. Inclinometers and accelerometers correct the roll.

All aspect inputs are combined with a full error model and filtered to produce real-time 4-Hz aspect solution that has the accuracy of the FOG, with drift removed at the 1–2 arcminute level. The 4-Hz aspect solution is fed into a servo-control computer (located on the side of the gondola in a pressure vessel known as "the keg") that controls, via coupled PID loops[2], the elevation drive, the azimuthal flywheel and de-rotator, and the cross-mounted flywheel that damps induced pendulation. The corrections to gyroscope drift described above are only good on the sub-arcminute level.

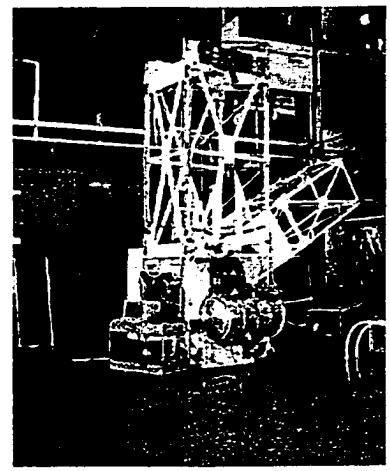

Figure 2.3: The *GRATIS* payload in the high bay at Columbia University's Nevis Laboratories in Irvington, NY. The telescope is slewed out as during an observation and the roll-bars are removed.

The more accurate 10–20 arcsecond determination, which is essential to final localization of a gamma-ray target, must use additional data from both sun- and star-trackers. The sun tracker is mounted near the connection point of the gondola to the balloon. The star tracker is a camera mounted on the side of the telescope. Finally, absolute attitude determination (that is, of the gamma-ray telescope relative to the sky) requires boresight information from ob-

[2]A PID loop is a control algorithm to keep the controlled quantity (e.g. temperature), x, at a desired value. output $= G\left(\epsilon + R\int \epsilon dt + D\frac{d\epsilon}{dt}\right)$, where output is the environment-changing parameter (e.g. rate of gas burn for temperature control), ϵ is the difference of the value x from target, G is the gain (proportional parameter), R is the reset parameter, D is the derivative parameter. G, R, D must be tuned to the particular system (Shaw, 2001, 1996).

servations of gamma-ray targets with well known positions to give the offset of the telescope's alignment axis from the intended target.

The workings of the attitude determination and control system (ADCS) are described in greater depth in Craig *et al.* (1998).

2.3 Telescope Overview

The *GRATIS* telescope consists of 36 co-aligned one-dimensional coded-aperture subtelescopes in a six-by-six array, each rotated five degrees with respect to its neighbor (Figure 2.4). Each telescope consists of a detector—cesium iodide crystal coupled to a position-sensitive photomultiplier tube (PSPMT; Hamamatsu 2485R)—, fine and coarse collimators, and a mask. The placement of masks and other functional parts of the telescope are labeled in Figure 2.2. Each mask is a one-dimensional pattern of transparent and opaque elements running parallel to the imaging direction (y-axis) of the detectors.

The passive shields surrounding each detector are made of a laminate of lead-tin-copper (Pb-Sn-Cu) layered with respective thicknesses 2, 1 & 1 mm. (The geometry of the shields and the fine collimators are described in more detail in §A.1.) The masks are made of the same laminate.

Figure 2.4: *Left:* Schematic view of the mask-plane of *GRATIS*. *Right:* The *GRATIS* mask pattern

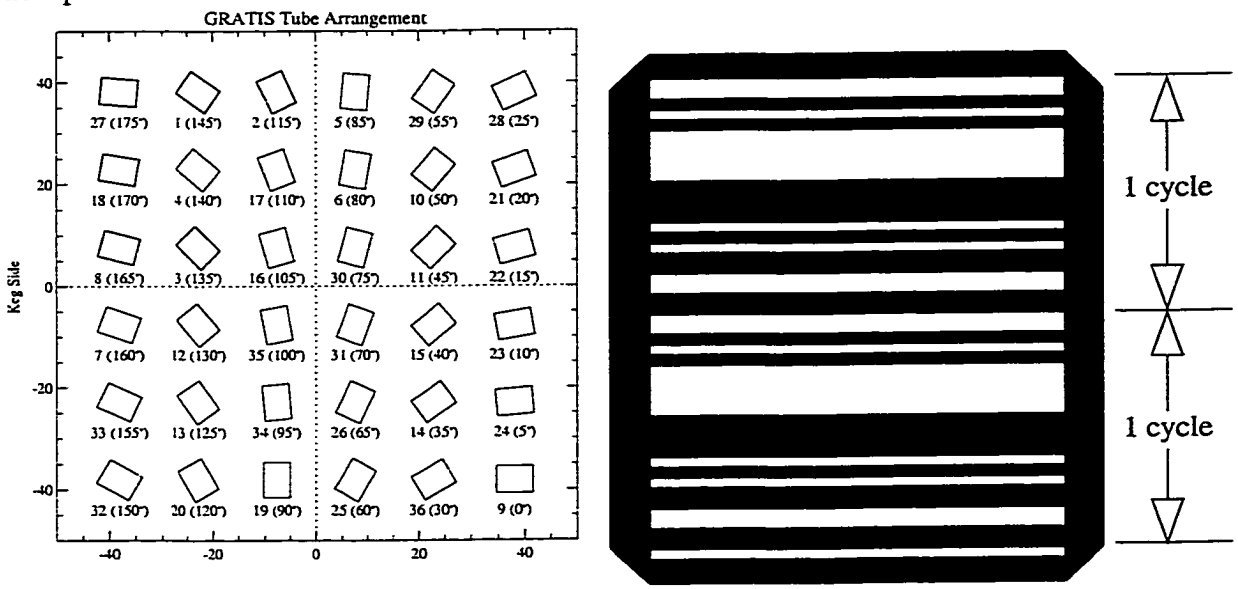

If the detectors' position resolution were perfect, the angular resolution would be determined by the size of the mask elements *vs.* the focal length:

$$\arctan\left(\frac{0.216\text{ cm}}{386.8\text{ cm}}\right) = 1.92'.$$

Along the imaging direction, fine collimators 29 cm long ensure that each part of the detector can see only one mask element. The fine collimators slats are made of Cu/Sn/Pb/Sn/Cu layered 1/1/3/1/1 mils thick. Incoming gamma-rays approach at a small angle with respect to the axis of the detector, so their path length through the fine collimators is large. The fine collimator assembly is surrounded by a rectangular tube of the ubiquitous Pb-Sn-Cu laminate, the same that surrounds the phototubes.

Figure 2.5: *Left:* Coarse collimator response. *Right:* Fine collimator response.

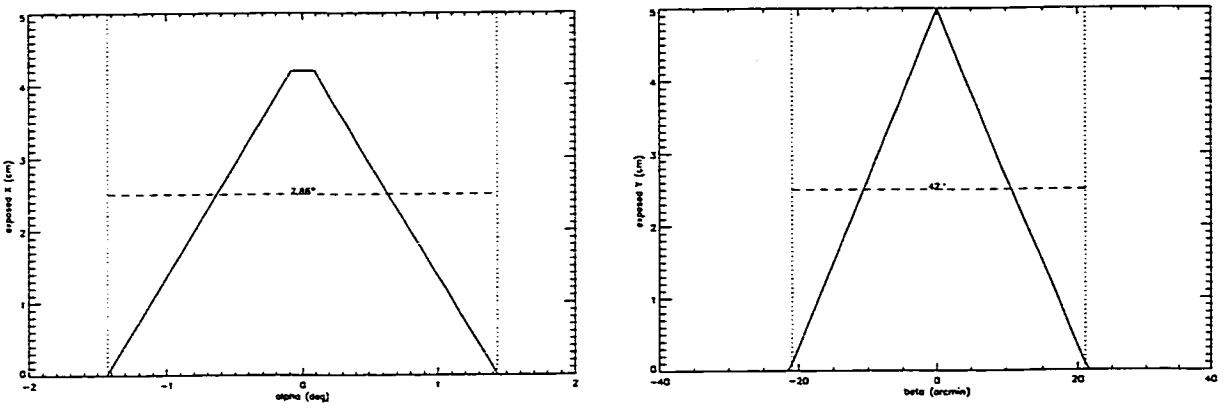

In the non-imaging direction, coarse collimators of Pb-Sn-Cu layered 12/6/6 mils thick restrict the field of view to

$$\arctan\left(\frac{1.875''/2}{46.5'' + 10.5'' + 0.75'' + 11.75''}\right) \times 2 = \boxed{1°32' \text{ FWHM}} \qquad (2.1)$$

2.4 Detectors

Each of the sub-telescopes consists of a number of components. The one-dimensional mask, constructed of a graded-Z (Pb/Sn/Cu) laminate, is collimated to five degrees in the non-imaging direction. In the imaging direction, a precise set of foils (the previously mentioned fine collimators) provide collimation to 40 arcminutes (cf. figure 2.5) and ensure that each pixel on the detector sees a complete mask pattern. The mask is located nearly four meters from the gamma-ray detectors. Each detector consists of a 36-cm^2 (5.22 cm $\times$ 6.909 cm; active area: 21 cm^2 = 5 cm $\times$ 4.2 cm) CsI(Na) crystal.

The crystal thickness, determined by angular resolution requirements, as well as the desired bandpass, is 2 mm (Harrison, 1993, chapter 4).

Gamma-rays scintillate in the crystal to produce visible light photons. This scintillation light from the crystal is detected by a two-dimensional position sensitive photomultiplier tube. The outputs from the tube include the "last dynode signal," which warns the discriminator of an incoming event, and four charges (x_1, x_2, y_1, y_2). The sum of these charges is roughly proportional to the energy of the event, while the position of the event is given roughly by

$$x \approx \frac{x_1}{x_1 + x_2}, \; y \approx \frac{y_1}{y_1 + y_2}$$

The detectors are described in greater depth in chapter 4 of Harrison (1993).

The four analog outputs from the PSPMT are amplified and fed into CAMAC-based electronics which do the discrimination, digitization, time tagging and preliminary logging of the events, as described in the next section. The electronics and detectors are mounted in a sealed pressure vessel to minimize the effect of ambient temperature variations. Even with the care taken, the light yield of the crystals, the gain of the PMTs, and the performance of the data-collection electronics change during the flight. Modeling or calibration of these effects is an important step in producing the most scientifically useful data set. The LED in-flight calibration system

checks the PMT gain, but the crystal conversion efficiency requires ground calibration.

To veto the overwhelming number of background event signals (around 3000/second) that would be created in the tubes by the immense flux of charged particles in the upper atmosphere, a one-cm-thick plastic scintillator shield effectively surrounds the gamma-ray detector collection on five sides (the top side was removed because it blocked gamma-rays without significantly improving charged particle rejection). A small percentage of events do elude veto by the shields, however, and can cause significant data contamination. Additionally, cosmic and atmospheric radiation along with radiation from other effects, such as crystal activation, dominate the paltry gamma-ray flux from most astronomically interesting sources. Since the sources of unwanted signal vary with payload attitude, modeling the background in light of the behavior of the payload is crucial to refining the data set. Efforts on that front are described in chapter 3.

2.5 Data-acquisition Electronics

These electronics reside in the CAMAC crate in the tail section of the *GRATIS* telescope, just under the curved end-cap (cf. Figure 2.2). The center of *GRATIS* data acquisition, the general as it were, is the gamma-ray computer, an Ampro "Little-

Board" 386. If the Ampro is the general commanding the small army of modules (listed in table 2.1), the list processor (LP) is its lieutenant, handling the immediate exigencies of data collection. (The crate controller acts as messenger between the general and its army, most especially the LP.) The LP accumulates data from the discriminators, scaler, and ADC's (cf. figure 2.6) in its internal data memory (separate from the instruction memory) and dumps the contents of its data memory to the Ampro at intervals correlated to the rate (typically somewhere between 0–10 seconds; controlled by a PID loop). The Ampro stores this data to its hard disks and also directs it to the DSP card, where it is processed to be telemetered to the ground.

The modules in the Ampro's data-collection army reside in the CAMAC crate that sits squarely in the center of the telescope's back end. The advantage of the CAMAC crate is that it allows use of less expensive, ready-made parts. Its major disadvantage is its heavy power-consumption. Figure 2.9 (p. 28) shows the logical arrangement of the *GRATIS* data acquisition electronics.

When *GRATIS* is first powered up, it must be prepared for data collection. The Ampro sets the voltages for the phototubes through the DAC, loads the correct register values and channel masks to the discriminators, and uploads the LP with its instructions. (All of these settings are taken from the flight code's configuration

Figure 2.6: Gamma-ray data acquisition schematic, from Keck *et al.* (1996).

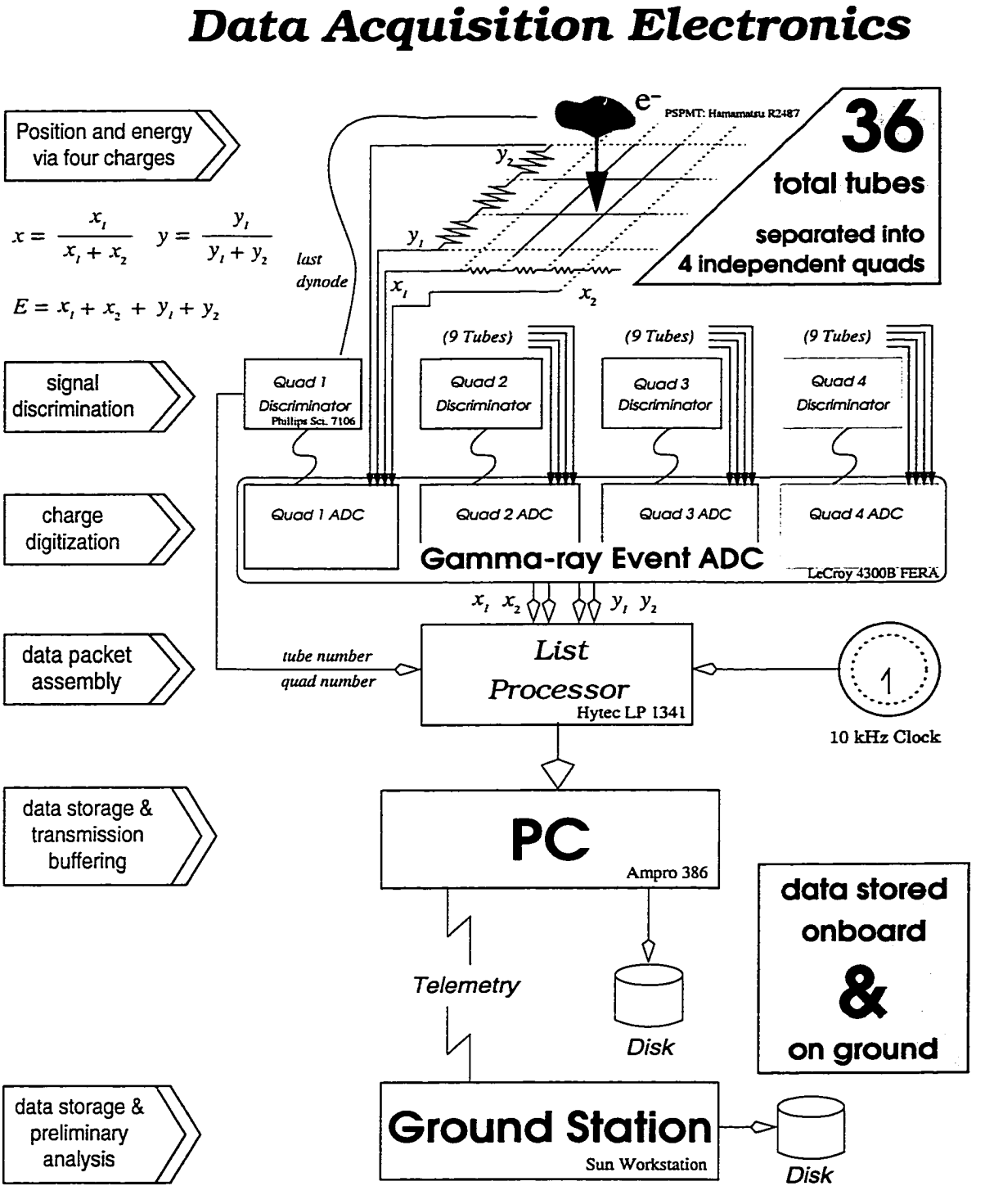

Table 2.1: Manifest of CAMAC modules and slot assignments

slot	name	make
1	*empty*	-
2	internal clock	*home-made*
3	DAC	HYTEC 645
4	*empty*	-
5	Gamma-ray ADC	LeCroy 4300B FERA
6	LED ADC	LeCroy 2259B
7	scaler	HYTEC 375-S
8	quad 1 discriminator (for tubes 1-9, coded blue)	Phillips 7106
9	quad 2 discriminator (for tubes 10-18, coded red)	Phillips 7106
10	quad 3 discriminator (for tubes 19-27, coded green)	Phillips 7106
11	quad 4 discriminator (for tubes 28-36, coded orange)	Phillips 7106
12	charged particle discriminator (no. 5, coded purple)	Phillips 7106
13	*empty*	-
14	*empty*	-
15	logic unit	LeCroy 4564
16 17	level translator	LeCroy 7126
18 19	gate/delay generator (ADC gate, LED LP, CP Veto, x-ray veto)	LeCroy 7194
20 21	quad gate/delay generator	LeCroy 7194
22	LP trig buffer ("Greg's box")	*homemade*
23	list processor (LP)	HYTEC 1341
24 25	crate controller (address: 3)	Jorway model 73

no.	signal
0	1-Hz clock
1	LED
2	quad 4
3	quad 3
4	quad 2
5	quad 1
6	GPS signal

Table 2.2: List processor triggers

file `inst.cfg`.) *GRATIS* is now ready to take data.

The end of data acquisition, naturally, is data. This data has within it—buried hopefully not too far below the surface—the positions and energies of gamma-rays from the target under observation. The data is encoded into the data stream that is stored on disk and transmitted to the ground. The data stream is divided into discrete units called *events*. There are several types of events (listed in table 2.4, p. 24). Each type of event has a set length that is an integral multiple of sixteen bytes (= 1 line, as viewed with the UNIX command `od -x`).

Each type of event belongs to one of two classes. The first class consists of events that are original to the data stream, that is to say, buffered through the LP. The second class consists of events that are added to the data stream by the Ampro.

When an event occurs, one of seven triggers (see table 2.2) cue the LP to execute

pin	name	registers (l & h)
1	Q1	0
2	Q2	1
3	Q3	2
4	Q4	3
8	LED LP	7
9	10-k out	8, 12
10	ULD	9, 13
11	X-ray	10, 14
12	CP	11, 15

Table 2.3: Scaler triggers and registers

the instructions appropriate to that event type, which record the relevant quantities.

In the rest of this section, we explain each type of event and how it is represented in the data stream.

2.5.1 Scaler Event

The scaler is a digital counter. When one of its triggers is pulsed, it increments the corresponding register. Each register has one or two 16-bit bytes, as shown in the table 2.3.

The LP reads the scaler registers once a second in response to the 1-Hz pulse on its pin zero (cf. table 2.2). Figure 2.7 unfolds the contents of a scaler event.

The x-ray count recorded by the scaler includes upper-level discriminator (ULD)

type	description
0x00	X-ray
0x01	LED
0x02	Scaler
0x03	GPS
0x08	Header
0x12	Telemetry
0x25	LED-start
0x69	LED-stop
0x80	Bad-bit

Table 2.4: Event-type codes

Figure 2.7: Decoding scaler event data

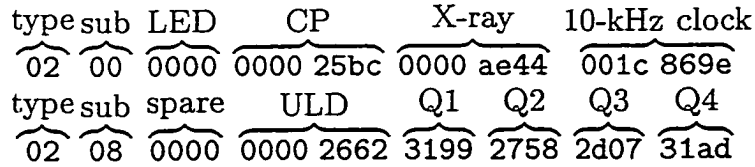

label	*value*	*meaning*
type	0x02	scaler event
subtype	0x00	first line
	0x08	second line
LED	lowest byte of LED-event count	
CP	charged particle event count	
X-ray	gamma-ray (data) event count	
spare	unused bytes	
ULD	upper-level discriminator event count	
Q1-Q4	event count for respective quadrant (LSBs)	

events, which are high-energy events usually caused by an ionizing particle that can temporarily blind *GRATIS* by saturating its amplifiers. To prevent this down-time, the upper-level discriminator in "Greg's box" (a homemade module) stops events whose last-dynode signal reaches a pre-determined high threshold from being passed along to the sum amplifiers (Harrison, 1993, figure 5.1, p. 78). The ULD also pulses scaler trigger 10.

Charged particle (CP) events are triggered when a pulse from the CP shield reaches a threshold determined by the CP discriminator (disc 5). The scaler also counts events on each quadrant (pins 1–4) and total x-ray events (pin 11). A 10-kHz clock pulses scaler trigger 9, effectively making it a clock counter.

2.5.2 Gamma-ray Event

List processor triggers 2–5 signal a gamma-ray event in one of the photomultiplier tubes. Before the LP ever receives this trigger, a chain of filters in the peripheral electronics decide if the event is worth recording.

The 36 tubes are divided into four independent quadrants of nine tubes apiece. Each quadrant has its own separate electronics chain (see figure 2.6, p. 20), consisting of a discriminator and a Fast-Encoding Read-out Analog-to-Digital Converter

(FERA/ADC). The gamma-ray event clock, incrementing at a rate of 10 kHz, gives a timing resolution of 100 microseconds.

Here is the sequence of events in recording a gamma-ray event (cf. figure 2.6, p. 20). The visible scintillation light from an incoming gamma-ray's interaction in a CsI(Na) crystal ejects photoelectrons off the cathode of the phototube to which it is coupled. The phototube amplifies the number of electrons. The ultimate stage of amplification (or dynode) pipes this pulse, known as the last dynode signal, to the discriminator for the respective quadrant (see figure 2.10 for a diagram of the timing sequence). If the pulse reaches a pre-set minimum level, the discriminator decides that the data represents a real event, and passes a digital 'true' to the FERA (Fast Encoding Readout ADC) to trigger its digitization of the phototube's four charges (x_1, x_2, y_1, y_2). (When the FERA is triggered, there is a brief delay, and then the CP/ULD veto is inhibited; this prevents an intervening CP or ULD event from stopping the processing of an event already in the acquisition chain, cf. signal 7 in figure 2.9, p. 28.)

The discriminator also signals the list processor (HYTEC LP1341). The signal to the LP first passes through a delay circuit in the 'LP Trigger Buffer' (in Greg's Box), so that the LP does not commence its execution until the FERA/ADC has had time

Figure 2.8: Decoding gamma-ray event data

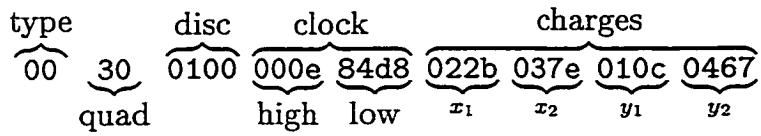

label	*value*	*meaning*
type	0x00	data (gamma-ray) event
quad	0x14	quadrant 1
	0x20	quadrant 2
	0x30	quadrant 3
	0x40	quadrant 4
disc	set bit gives tube no. w/in quadrant	
clock	high and low bytes of 10-kHz clock	
charges	$x \approx \frac{x_1}{x_1+x_2}$; $y \approx \frac{y_1}{y_1+y_2}$; $E \approx x_1 + x_2 + y_1 + y_2$	
	0x07ff	overflow

to finish digitizing (11 bits in 8.5 μsec). After the delay, the list processor (LP) grabs its own 'instruction pointer' to designate which quadrant flashed, the tube number (1–9) from the discriminator that triggered it, the high and low bytes of the 10-kHz scaler clock, and the four charges from the ADC (cf. figure 2.8). The LP stows these 16 bytes in its internal data memory, then clears the ADC to await further data.

2.5.3 LED Events

LP trigger 1 signifies a LED event. LED events are initialized by a signal from the ground and are part of *GRATIS*'s in-flight system for calibration of the PMT's.

Figure 2.9: *GRATIS* timing and logic after Alice Springs modifications. Circled numbers are keyed to figures 2.10 and 2.11.

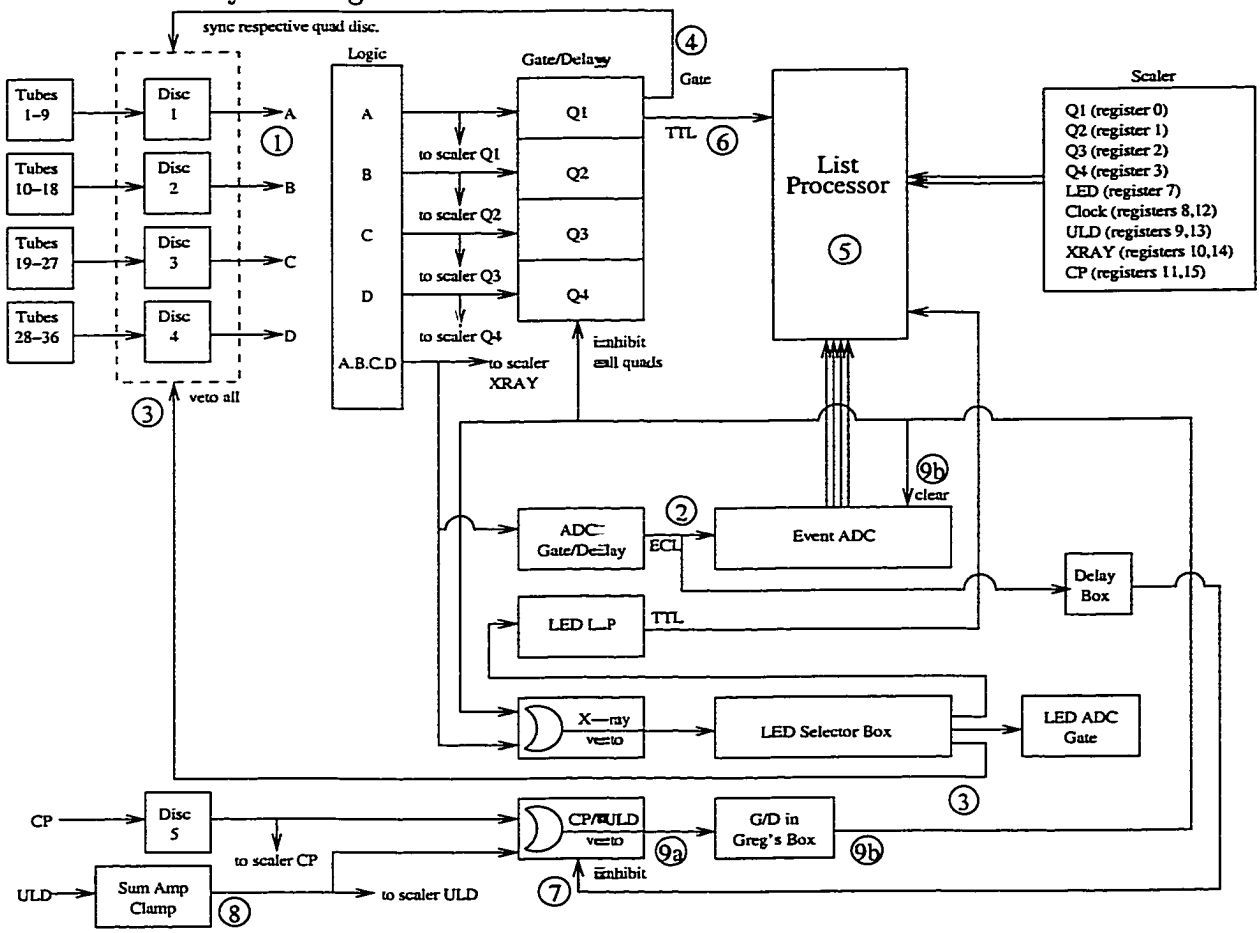

Figure 2.10: Gamma-ray event timing. Circled numbers are keyed to figure 2.9.

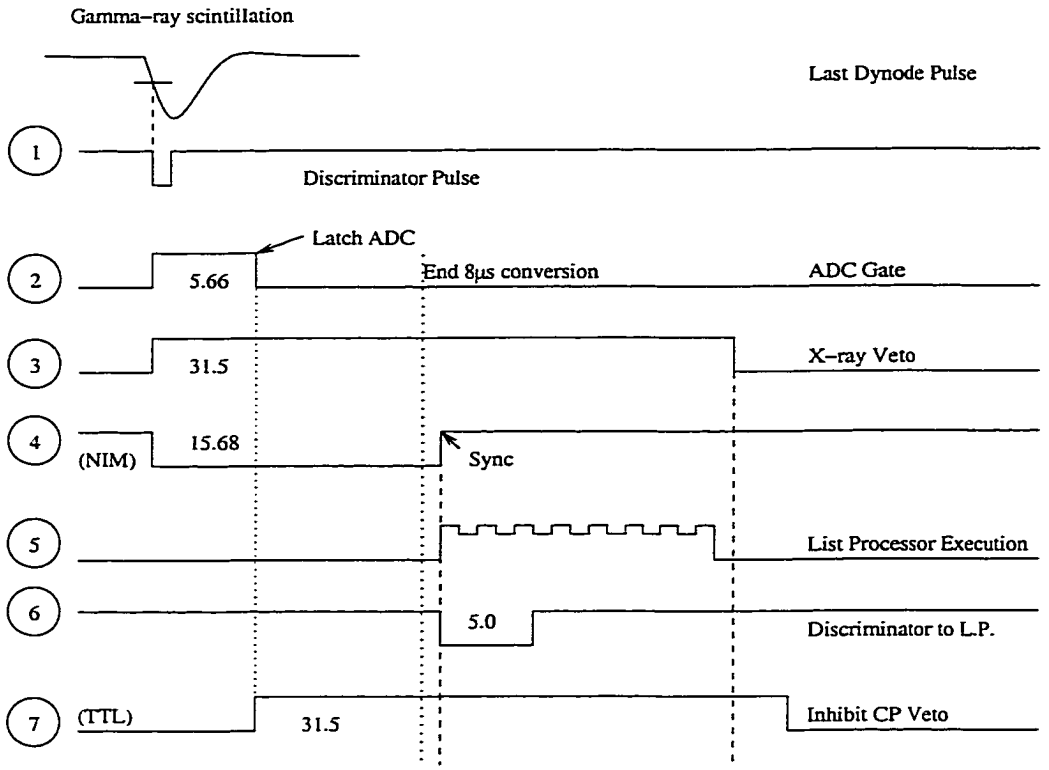

Figure 2.11: ULD event timing. Circled numbers are keyed to figure 2.9.

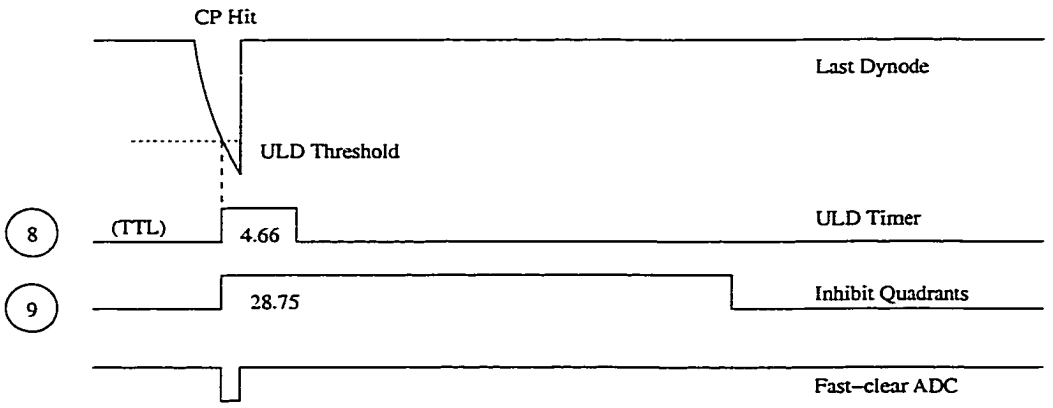

Figure 2.12: Decoding LED event data

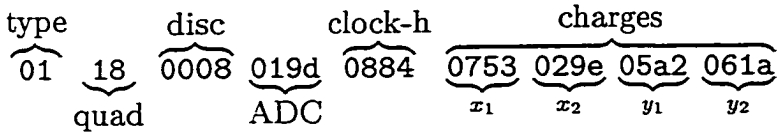

label	*value*	*meaning*
type	0x01	LED event
quad	0x18	quadrant 1
	0x24	quadrant 2
	0x30	quadrant 3
	0x3c	quadrant 4
disc	set bit gives tube no. w/in quadrant	
ADC	channel 0 of LED ADC	
clock	high byte of 10-kHz clock	
charges	$x \approx \frac{x_1}{x_1+x_2}$; $y \approx \frac{y_1}{y_1+y_2}$; $E \approx x_1 + x_2 + y_1 + y_2$	
	0x07ff	overflow

Figure 2.12 dissects a LED event.

2.5.4 Other Kinds of Events

LP trigger 6 signals a global positioning satellite (GPS) event. These are identical to scaler events, but have a type code of 0x03. Their purpose is mainly to record the value of the 10-kHz clock when *GRATIS* receives a signal from a GPS satellite. These values can be correlated later with Universal Time (UT) recorded by a computer in the keg to calibrate the 10-kHz clock. Figure 2.13 shows the clock drift throughout

Figure 2.13: Drift of 10-kHz clock for the Alice Springs flight.

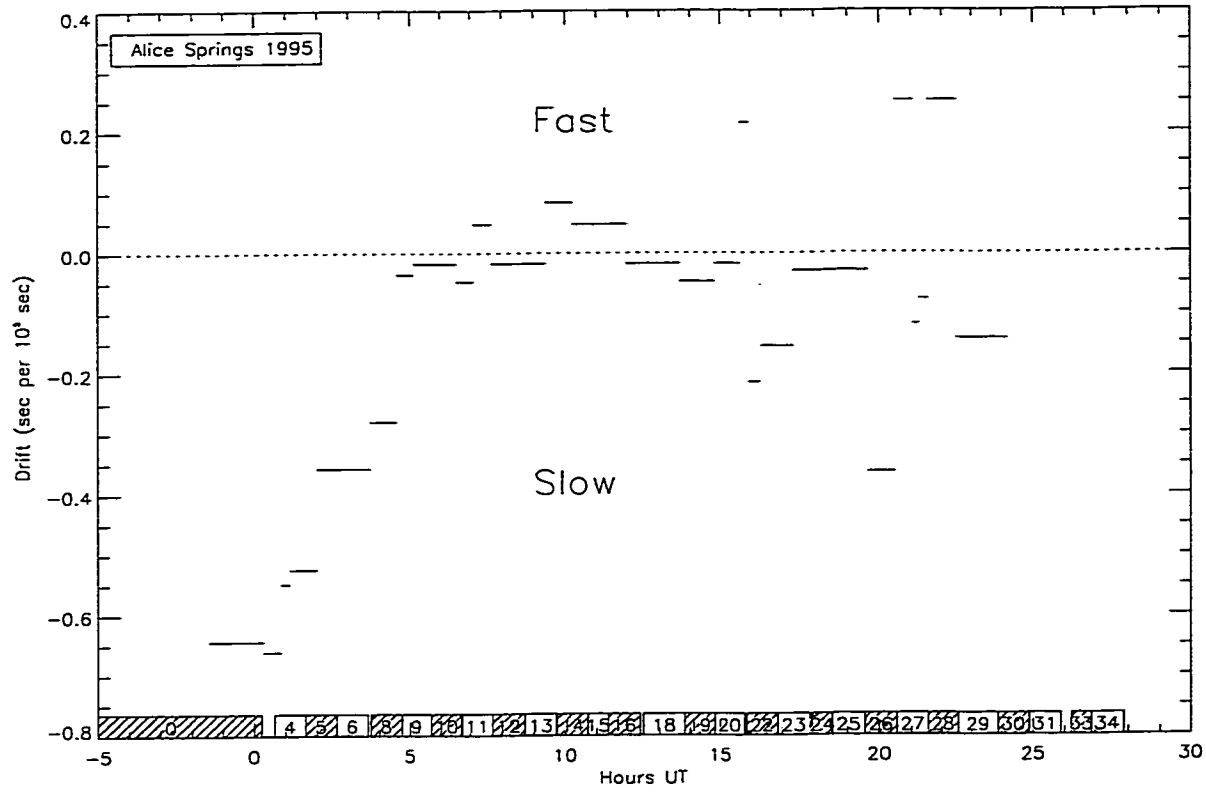

the last flight.

The GPS antennae sit on extensions from the four top corners of *GRATIS* and convey GPS signals to an Ampro computer in the keg that records the information in the signal, most notably the hours universal time (UT). The GPS signal is passed along to the telescope via a fiber-optic link, in order to preserve the electrical independence of the telescope from the gondola. (The same optical link box also passes

the DSP signal to the gondola for transmission to ground.) The LP trigger buffer receives the GPS signal and passes it to the LP to collect the proper data from the scaler.

Scaler, gamma-ray, LED, and GPS events are the only types of events recorded by the LP, but there are other event types that enter the telemetry data stream. All event types are summarized in table 2.4, p. 24.

The only significant type of event left to describe is the header event. A header is added to the data stream whenever the Ampro shuts down the LP to read its data memory. Data saved to on-board disk simply has the header data added directly to the data stream, without a type designation. Data telemetered to the ground has header data added that is pre-pended with the header type and a subtype. This pre-pended information occupies four bytes, leaving twelve bytes of each 16-byte line for actual header data. A full header event consists of 43 lines. The most useful thing header data contains is the values of the ADC pedestals (offsets). Other useful information includes the nine status bits (`xError`, `qError`, `cDriveError`, `dDriveError`, `LPMisaligned`, `DangerLimit`, `EventsTossed` plus two spare), and the P, I & D values of the PID loop. The exact contents are described in `instrumnt.h` of the flight code and `header.h` of the tel2nc code.

Some of the header data is also relayed to ground during data acquisition through the GRECV (=gondola receive) data that appears in a regular burst of ASCII characters on the screen of the ground-based Sun workstation. A number of point-and-click widgets decode and display this data to provide real-time information about the status of data-acquisition.

2.5.5 Data Pipeline

Once the data is successfully transferred to the ground, it must be analyzed. Raw disk data files (names of the form `d16h2233.000`) are converted to the Network Common Data Format (NetCDF or NCDF) using a program called `dsk2nc`. Raw telemetry files (names of the form `Mon16Oct22:33:52`) are converted with `tel2nc`. The resulting data files have names of the form `data_events_1.nc`, `data_events_2.nc`,.... Along with the data files, `dsk2nc` and `tel2nc` also produce a file called `header.nc` that contains the results of the periodic pedestal reads of the ADC, among other information. Files with names like `scalar_events_1.nc` contain the information from scaler events and `gps_events.nc` contains GPS event information.

The first processing step is to subtract the pedestals from the charges (x_1, x_2, y_1, y_2) recorded in the data. The pedestal is a charge periodically injected into the ADC, on

top of which the measured charge rides. The pedestals change over time— the most important dependence being temperature— and are subject to Poisson noise, so we fit a piecewise polynomial function to the pedestal values recorded in `header.nc` and store this information in a file called `pedestal.dat`. The program `ncadc` subtracts the fitted function from the four charge values of each event. It also culls any events that contain a charge of 0x07ff, the ADC's overflow indicator. The resulting file name has the form `data_events_1.nc~`.

The next step is to correct for the electronic offsets. The program `ncelec` uses a calibration file `electronic.dat` to apply this correction and store the resulting values (fx_1, fx_2, fy_1, fy_2) in a file named something like `data_events_1.nc~~`. The calibration procedure for `electronic.dat` is described in Harrison (1993), section 5.1.

The third processing step is to correct the positions of the photons. The program `ncwarp` uses the Oriel calibration of the tubes (described in Harrison (1993), §5.2) to correct the spatial variations. The original file name is appended with another tilda to derive the name of the output file, which contains the variables[3] x, y and E. However E is not yet the true energy.

[3]Jaesub Hong realized that a degree of freedom is discarded in this stage of the pipeline. He recovered it by constructing $r = (x_1 + x_2)/(y_1 + y_2)$. With this fourth variable removal of spurious CP-generated events becomes much simpler.

For the true energy, we must use `ncenergy` along with its calibration file `energy.dat` to shift the energies to their proper values. The final file has a name of the form `data_events_1.nc~~~~`.

These four processing steps make up the classical data pipeline. Irregularities in the pipelined calibration data taken before the 1995 flight in Alice Springs pointed to the need for additional pipeline steps. These steps will be described in Hong (2001).

2.6 Alice Springs Calibration and Response Matrix

To translate measured photon energies into spectra, we need to know how the detectors respond to photons of given energy. This information is encoded into a *response matrix*, which, given an incoming photon with a certain energy, tells the probability that the photon is detected at a given output energy. To construct the response matrix for *GRATIS*, I had to know two parameters, energy resolution and dead-layer thickness. (Dead-layer thickness effects the ratio of main-peak and escape-peak events.)

In tables 2.6 and 2.7 we print the results of the calibrations done on the ground before the Alice Springs flight. As tables show, the energy resolutions of the tubes range over 16–23%.

To estimate the dead-layer thicknesses, I ran simulations of a *GRATIS* detector using Lawrence Livermore National Laboratory's COG Monte-Carlo photon transport package (Buck & Lent, 1993; Wilcox & Lent, 1989, cf. appendix) with crystals of various dead-layer thicknesses. COG is a versatile package for simulating the transport of neutrons (10^{-4} eV to 30 MeV) and photons (10 eV to 100 GeV). We used version 8.0 and followed only photons, not neutrons (electrons are produced but not followed). We set electron-positron pair-production to result in two annihilation gammas that are transported, and for bremsstrahlung to be produced.

The simulation ran 2×10^5 photons at 59.5 keV (americium line) emitted normally from a 5.2-cm disk positioned four meters from the detector plane. A custom-written detector routine (`astrodet.F`, see appendix) recorded the energy each photon deposits in the crystal. The results allowed us to find the ratios of the escape peak counts to main peak counts for several dead-layer thicknesses. I fit these thickness-ratio pairs (table 2.5) to a second-degree polynomial that allows us to map the measured count ratios into anticipated dead-layer thicknesses, as shown in table 2.7.

Since the goal of all of this was to produce a single response matrix for XSPEC, we had to settle on one set of parameters. Our simple model predicted the vast majority of dead layers were $\sim 90 - 140$ μm, a range over which the output is not expected

Dead Layer (μm)	ratio	expected ratio
0	0.127	···
30	0.168	0.14
50	0.189	0.16
100	0.243	0.22
150	0.280	···

Table 2.5: Results of COG simulations of CsI crystal with indicated dead-layer thickness. The ratios are $(c_{\rm fluor} + c_{\rm esc})/c_{\rm main}$ for americium source. The expected ratios are from a simple linear interpolation of the same quantity for the $E = (46, 67)$ keV results of Harrison (1993, table 5.2).

to vary by much, so we chose 120 μm. By a similar argument we chose an FWHM energy resolution of 19% at 60 keV:

$$\frac{\Delta E(E)}{E} = \sqrt{\frac{60\ \text{keV}}{E}} \times 19\% \tag{2.2}$$

We used a COG simulation of a *GRATIS* detector to construct the response matrix (figure 2.14) given these parameters. The simulation ran $2{\times}10^6$ photons uniformly distributed over 7–300 keV and emitted normally from a 5.2-cm disk positioned four meters from the detector plane. As before `astrodet.F` recorded the energy deposited in the crystal and the original energy of each photon, and these were read into IDL. Since the results of the simulation are not subject to the finite energy resolution of the phototubes, they had to be blurred according to the average energy resolution (eqn. 2.2) before binning and construction of the FITS-formatted `.rmf` file for XSPEC.

Table 2.6: Results of 1995 alignment and shadow-mask calibrations. Tube 4 was too poor to fit, and tube 15 had been removed as noted in text.

tube no.	Alignment			Shadow		
	peak	FWHM	$\Delta E/E$	peak	FWHM	$\Delta E/E$
	keV			keV		
1	59.8475	10.34632	0.17288	63.6816	10.8437	0.17028
3	58.6284	12.84881	0.21916	62.2914	11.1742	0.17939
4	56.9628	11.91886	0.20924	58.0767	14.0774	0.24239
5	55.3530	9.88177	0.17852	67.3768	12.5761	0.18665
6	63.3006	10.77359	0.17020	60.9905	23.4707	0.38483
7	57.5513	10.25824	0.17825	55.2430	10.2632	0.18578
8	58.4380	11.95574	0.20459	60.7139	14.3946	0.23709
9	58.7590	13.19309	0.22453	61.5116	15.7734	0.25643
10	60.8292	10.84995	0.17837	64.5867	11.4862	0.17784
11	61.1133	10.42180	0.17053	60.5323	10.5695	0.17461
12	60.0783	11.44582	0.19052	59.5571	11.3484	0.19055
13	58.4030	10.29142	0.17621	65.7359	13.1234	0.19964
14	60.7632	9.86203	0.16230	69.9369	13.8221	0.19764
16	59.4097	11.08584	0.18660	58.1216	11.1344	0.19157
17	58.2542	13.05762	0.22415	57.9750	13.6686	0.23577
18	58.3802	13.26128	0.22715	59.5111	13.5366	0.22746
19	57.1737	13.06427	0.22850	70.6675	16.6943	0.23624
20	57.8492	10.36080	0.17910	62.9498	11.6008	0.18429
21	59.6984	9.98344	0.16723	60.2402	10.2372	0.16994
22	58.0836	10.02835	0.17265	61.6756	23.4366	0.38000
23	60.8469	11.35570	0.18663	59.8585	11.4865	0.19189
24	58.0988	11.41012	0.19639	65.3291	13.2856	0.20336
25	57.6413	9.48334	0.16452	66.0305	11.7219	0.17752
26	58.8208	9.38992	0.15964	63.0936	15.8774	0.25165
27	60.1635	13.45731	0.22368	58.1726	13.5101	0.23224
28	62.6231	11.81656	0.18869	59.3400	11.3705	0.19162
29	57.2505	10.67588	0.18648	58.3146	11.0293	0.18913
30	63.0466	13.28730	0.21075	60.7024	13.9011	0.22900
31	57.9710	12.34062	0.21288	59.6299	13.3336	0.22361
32	59.4970	13.99477	0.23522	65.2767	17.1716	0.26306
33	59.4060	9.57292	0.16114	59.7991	11.1086	0.18576
34	59.5788	10.23901	0.17186	63.9857	12.0084	0.18767
35	60.3983	10.60772	0.17563	54.5266	10.2112	0.18727
36	59.6056	11.63735	0.19524	64.6567	14.0382	0.21712

Table 2.7: Results of Alignment '95. Dead layers are calculated from a polynomial fit to the count ratios from the COG simulation of the alignment calibration.

tube	gain	$\Delta E/E$	ct. ratio	Dead Layer (μm)
1	1.03848	0.17417	0.25724	118.18370
2	0.51411	0.19349	0.15066	17.30416
3	1.05506	0.23053	0.20962	67.02234
5	1.09193	0.18407	0.25669	117.50071
6	1.49937	0.20171	0.24128	99.38279
7	0.93726	0.19281	0.25541	115.92050
8	1.03125	0.23158	0.22526	82.34053
9	1.06323	0.23266	0.22042	77.47186
10	1.09356	0.18254	0.21736	74.45930
11	1.08832	0.17691	0.28000	149.72214
12	1.06921	0.19755	0.25660	117.39243
13	1.04840	0.23439	0.23313	90.51521
14	1.15690	0.18378	0.13458	5.32365
15	1.06487	0.17848	0.24107	99.15409
16	1.01897	0.19716	0.22037	77.42791
17	1.03109	0.24761	0.16212	26.19683
18	1.04554	0.22418	0.24241	100.65739
19	1.08960	0.22212	0.24164	99.79377
20	1.00073	0.18369	0.28481	157.45453
21	1.01793	0.17515	0.25895	120.33466
22	1.50722	0.18293	0.29293	171.77473
23	1.04748	0.20164	0.27431	141.15399
24	1.05625	0.20070	0.27824	147.00877
25	1.05905	0.18754	0.25571	116.29450
26	1.01789	0.22393	0.25288	112.83306
27	1.01422	0.23819	0.23863	96.45389
28	1.02243	0.18781	0.27911	148.34415
29	1.04101	0.19695	0.26256	124.97002
30	1.07681	0.22554	0.25613	116.80709
31	1.05393	0.22647	0.24537	104.01093
32	1.07922	0.25649	0.29075	167.75208
33	1.02336	0.17379	0.21058	67.93353
34	1.02504	0.18859	0.25658	117.36053
35	0.98314	0.19201	0.26014	121.85357
36	1.02936	0.20481	0.24530	103.92970

Figure 2.14: *GRATIS* response matrix, assuming a 120μm-dead-layer on the CsI crystal (cf. Harrison, 1993, §5.4) and 19% FWHM energy resolution at 60 keV.

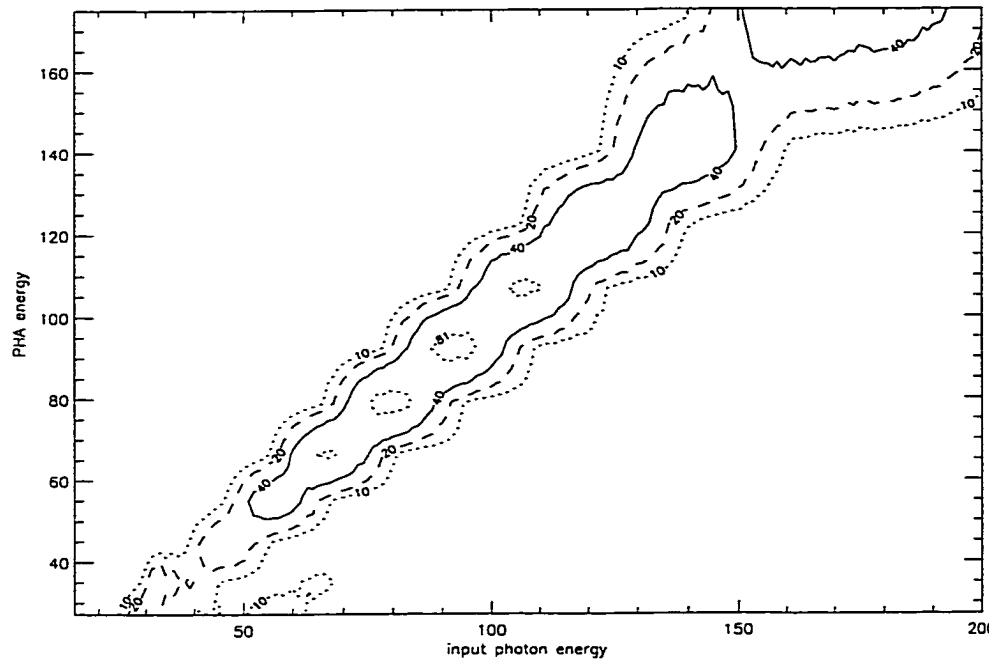

2.7 Outstanding Issues in Data Acquisition

GRATIS was designed with built-in redundancy so that small equipment breakdowns, as often occur in such complicated projects in an uncontrolled environment, would not ruin the entire experiment. Unfortunately a series of small problems compounded each other to compromise the quantity and quality of data from the 1995 Alice Springs flight.

The first error noticed was the incorrect partitioning of the on-board hard drive.

Figure 2.15: *GRATIS* effective area under same assumptions as figure 2.14.

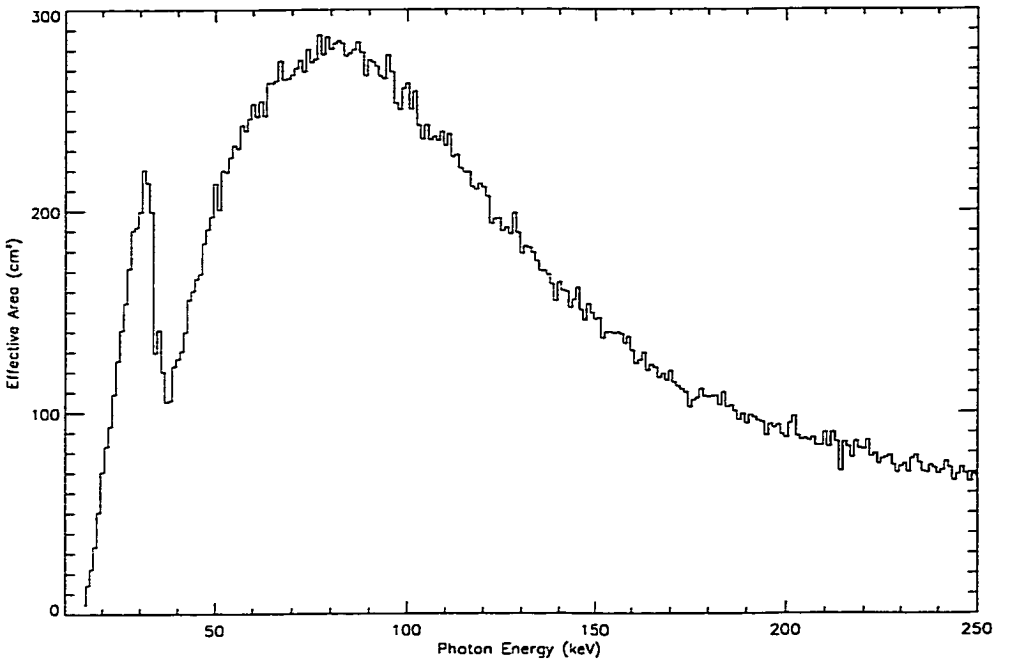

The drive had a capacity of two gigabytes—plenty of storage for a flight of any conceivable length. Sadly the hard drive was partitioned using the original MS-DOS file allocation table (FAT) configuration so that the Ampro computer could only address 512 megabytes, a fourth of its capacity. As a result, much of the data was over-written by new data, which is to say deleted from the drive.

In addition to being recorded to disk, data from *GRATIS* was telemetered to the ground, so drive problems would have done little harm to the experiment had the DSP card, which prepares the data for transmission to the ground, worked properly.

Unfortunately, a small mistake in the programming of the DSP card caused it, at sufficiently high data rates, to overwrite its own buffer, effectively discarding two-thirds of the telemetered data.

In the end, *GRATIS* delivered complete data on disk for eight pointings and part of another (yielding five astronomical sources) and partial data through telemetry for 26 pointings (another six sources).

Additionally, further tests have demonstrated low-level data mixing of unknown origin, involving switching of tube number between events, but this effect is several orders of magnitude weaker than the dominant errors.

GRATIS was an experiment on a limited budget. The hefty CAMAC crate was employed so that off-the-shelf components could be used instead of custom-designing electronics. The potentiometer-set gate width for the ADC (5.66 μsec) lies far above the listed product specifications: "Residual Pedestal: From 1 pC to 13 pC for gate width from 50 to 500 nsec, all inputs down." It is not clear what effect the large gate width should have on the measured charges; energy calibration would seem to indicate that, at least at the low data rates of ground calibration, the effect is minimal.

The data-collection hardware also responded poorly to the low temperatures early

Figure 2.16: Telescope temperatures during the flight Alice Springs in October 1995. The frame-top sensor measures the external temperature of the payload. The other three temperatures are inside the telescope pressure vessel.

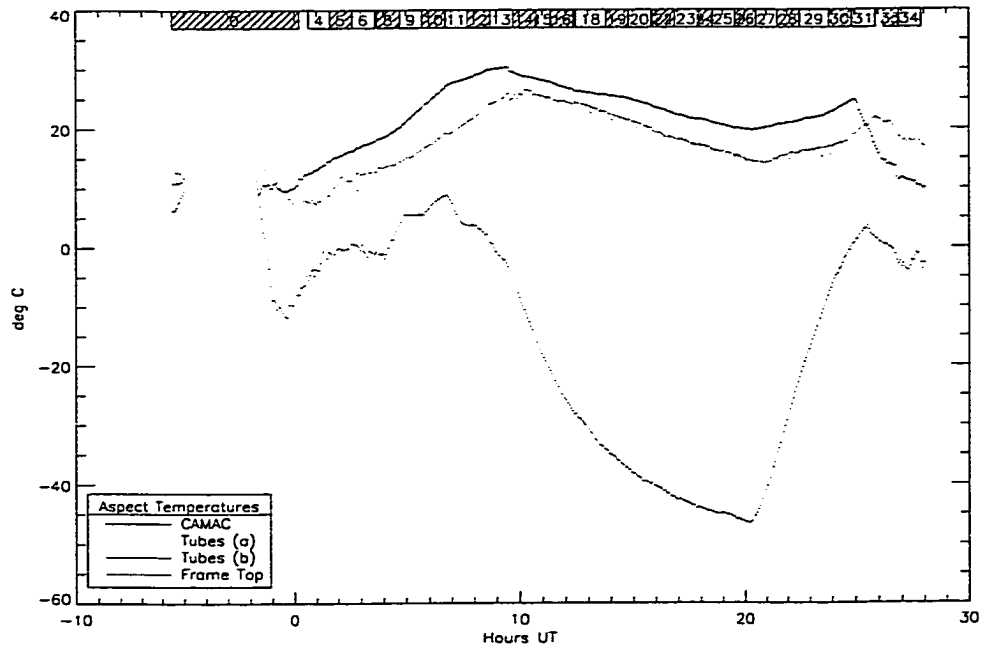

in the flight by discarding most of the data. Ground-based tests showed that at low temperatures the pedestal more frequently comes up with a value of zero—unusable, which makes sense with the ADC's specified operational temperature range being 0 to 40°C. Additionally the LP tends to misalign more frequently at low temperatures. Figure 2.16 shows the telescope temperatures during the Alice Springs flight in 1995.

The low-temperature effects were not a concern for the observation of GRS 1758–258 whose analysis we take up in chapter 4.

Chapter 3

Background modeling

BACKGROUND RADIATION is the most nettlesome problem in experimental gamma-ray astrophysics. For gamma-ray payloads in the upper atmosphere, background photons outnumber source photons a hundredfold. While long-duration missions (usually satellites) have much higher background levels (mostly due to activation), missions of limited duration lack the time to characterize precisely the particularities of their background radiation. Off-source pointings can be employed to measure background, but these consume precious time that could otherwise be used for astrophysical observations. For non-imaging missions[1] the only alternative is modeling the background signal, a time-varying quantity highly sen-

[1] As we saw in chapter 2, *GRATIS* images without focusing. Theoretically we can extract background information from on-source pointings. In practice, this procedure depends on exact knowledge of the position of the source and the boresighting of the telescope.

sitive to the materials and geometry of the instrument and its platform and to the mysterious radiation environment of the outer reaches of earth's atmosphere.

Large gaps persist in our knowledge of this radiation environment. We first briefly review the various types of radiation. Second we examine natural variations in the primary cosmic-ray flux, which drives most of these forms of radiation. Third, we survey previous empirical and theoretical work to develop improved analytic source functions for the two forms of background radiation that are not specific to payload geometry: the cosmic diffuse and atmospheric gamma-rays. Finally, we estimate the contribution of each form of background radiation to the background signal of *GRATIS*.

3.1 Types of background radiation

The gamma-rays in the upper atmosphere originate outside the atmosphere (primary photons) or in the interactions of cosmic rays and their progeny with the nuclei in the atmosphere (secondary photons). Additionally, cosmic rays can interact directly in the material of the detector to produce gamma-rays. Figure 3.1 schematically illustrates the types of background radiation.

The main source of primary photons, apart from the astronomical source under

Figure 3.1: Types of background radiation.

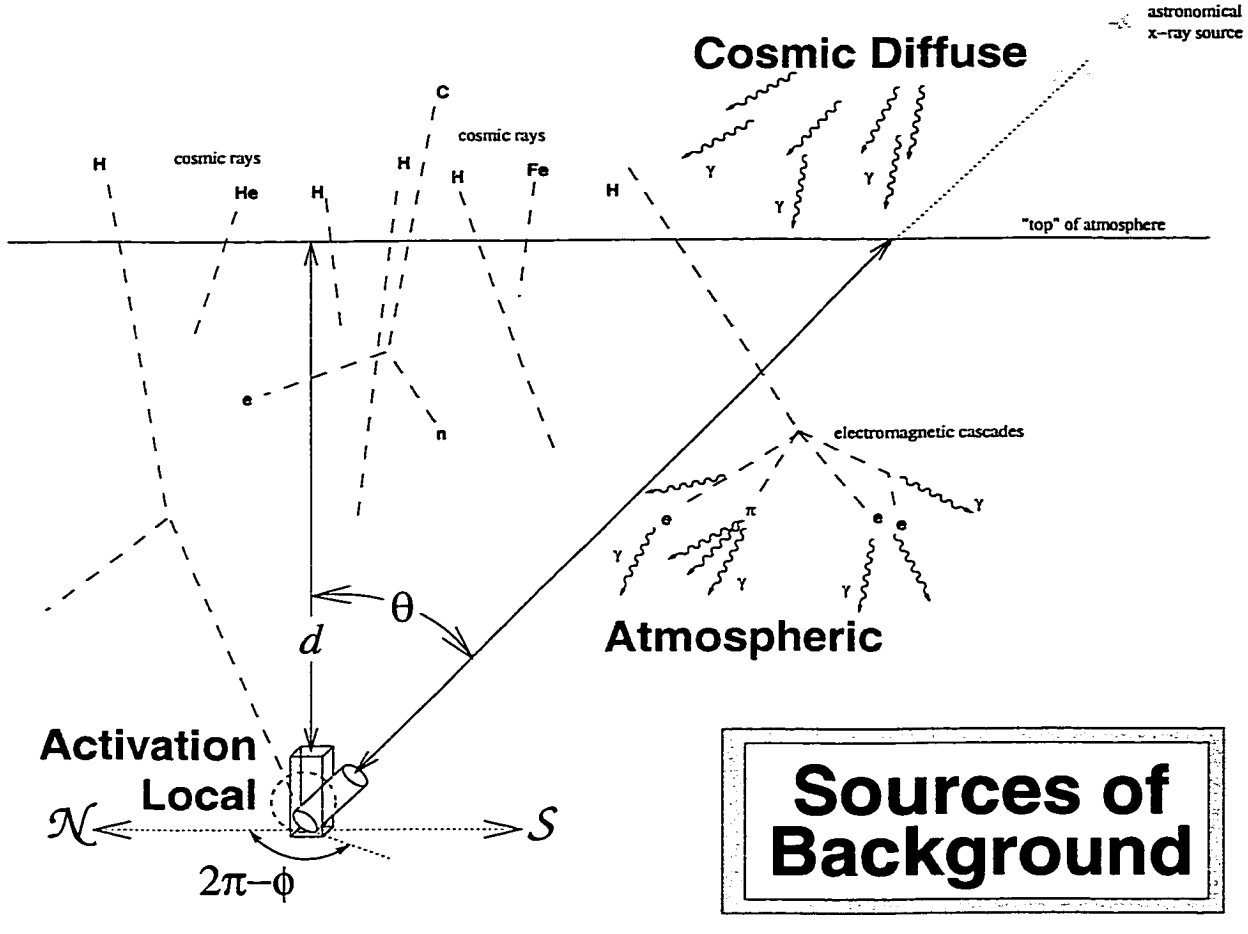

observation, is the *cosmic diffuse* background, which comes from all parts of the celestial sphere (§3.4.1). The plane of the Milky Way is an especially intense source of these photons known as the *Galactic diffuse emission.*

Secondary photons originate in several sources. Primary *cosmic* rays striking the atmosphere break up through hadronic and electromagnetic cascades into what are called *atmospheric gamma-rays* (§3.4.2) and secondary cosmic rays.

The primary and secondary cosmic rays can also spallate in materials of the payload itself. This component is called the *local gamma-ray background* (§3.4.3). Of particular concern among the cosmic ray secondaries is the *neutron background* (§3.4.4), which can slip undetected through charged particle veto shields to create spurious events in the detector. This source of background is a major concern for missions whose detectors have large neutron cross-sections and high mass.

Over time, the flux of cosmic rays can activate materials of the payload, particularly the scintillator crystal, causing the delayed (and therefore unshieldable) *activation* background (§3.4.5). This component is not important for balloon missions, which are presently constrained to short duration flights.

3.2 Cosmic-ray dependencies

With the exception of the cosmic diffuse flux, all forms of radiation in the upper atmosphere have their origin, at least remotely, in the flux of primary cosmic rays. Hence, it is important to understand the natural variations in this flux.

The ability of a cosmic ray to penetrate the earth's magnetic field without being deflected is quantified by its momentum per unit charge (viz. $P = pc/q$), called *rigidity*. The usual unit is gigavolts (GV).

At a given latitude and longitude and angle of incidence, the earth's magnetic field does not admit cosmic rays below a threshold, known as the cutoff rigidity. In most cases, when we refer to cutoff rigidity, we intend the *vertical cutoff rigidity*, because the vertical component is the most important contribution (Hayakawa, 1969, p. 321).

The atmospheric gamma-ray (and by extension, locally generated background) flux has a roughly inverse proportionality to a location's cutoff rigidity[2] to *vertical cutoff rigidity*. For example, the last flight of *GRATIS* was in Alice Springs where the cutoff rigidity is 8.5 GV (Ait-Ouamer *et al.*, 1988), whereas in Palestine, Texas (from where so many flights are launched that it has become the standard reference for

[2]The power-law index= -1.13 according to Thompson *et al.* (1981). Cf. Dean *et al.* (1991§2.1).

cosmic- and gamma-ray data) the rigidity is 4.5 GV. Thus the atmospheric gamma-ray flux should be about twice as strong in Palestine as in Alice Springs.

Figure 3.2 shows the vertical cutoff rigidities around the world. According to Dvornikov *et al.* (1985), diurnal variations in the cutoff rigidity are roughly sinusoidal, peaking at 2–4 hours local time. For an average rigidity of 4.3 GV, the amplitude is around 0.06 GV during periods of moderate geomagnetic activity and around 0.1 GV for periods of high geomagnetic activity. The amplitude of these variations are less for places with a higher average cutoff. In Alice Springs, even during periods of high geomagnetic activity, the variation will be less than 0.08 GV (the diurnal variation for 5.8 GV during high activity). This is less than a one percent effect.

Most cosmic rays are galactic in origin, but the flux is modulated by the sun's magnetic field (Duldig, 1994). The flux of cosmic rays itself has not only a diurnal variation (amplitude $\lesssim 0.5\%$), but also semi- and tri-diurnal variations, with amplitudes of $\lesssim 0.06\%$, and $\lesssim 0.02\%$, respectively (Ahluwalia, 1978).

Ahluwalia (1997) plots the yearly variation of cosmic ray intensities at high latitudes from 1937 to 1994: the maximum difference between any two years is less than five percent. There are also half-day and day-long periods in the cosmic-ray intensity (Hayakawa, 1969), but the amplitude of these is $\sim 0.1\%$ (Cranshaw, 1963).

Forbush decreases are reductions in cosmic-ray flux by $\sim 3-20\%$ over the timescale of hours, with a recovery of days to weeks (Duldig, 1994). The only such decrease on record for 1995 was October 16 with a magnitude of 3.7% (National Geophysical Data Center/NOAA, 1997). While this occurred the day prior to the last flight of *GRATIS*, the magnitude is much smaller than the expected margin of error for our background calculations.

White *et al.* (1988) report a north-south asymmetry in the atmospheric gamma-ray flux that comes from observing different parts of the atmosphere that have different cutoff rigidities, resulting in different incident flux of cosmic rays. This variation is only a factor of a few percent, so it is negligible for our purposes. (Ahluwalia (1978) reports two- and three-cycle per day harmonics, but at smaller magnitudes.)

In sum, none of the natural variations in cosmic-ray flux are more than a few percent, so they are negligible for the purpose of simulating background radiation, an endeavor in which a factor of two difference from observation is considered as doing rather well.

To eliminate the prompt signal from primary and secondary cosmic rays, the detector compartment of *GRATIS* is surrounded by plastic scintillator that triggers a charged particle (CP) veto when a cosmic ray passes through it, signaling the data

Figure 3.2: Trajectory-derived Effective Vertical Cutoff Rigidities for Epoch 1975.0 from Shea & Smart (1975). For most places on the earth, the secular variations over 25 years are not more than 0.2 GV.

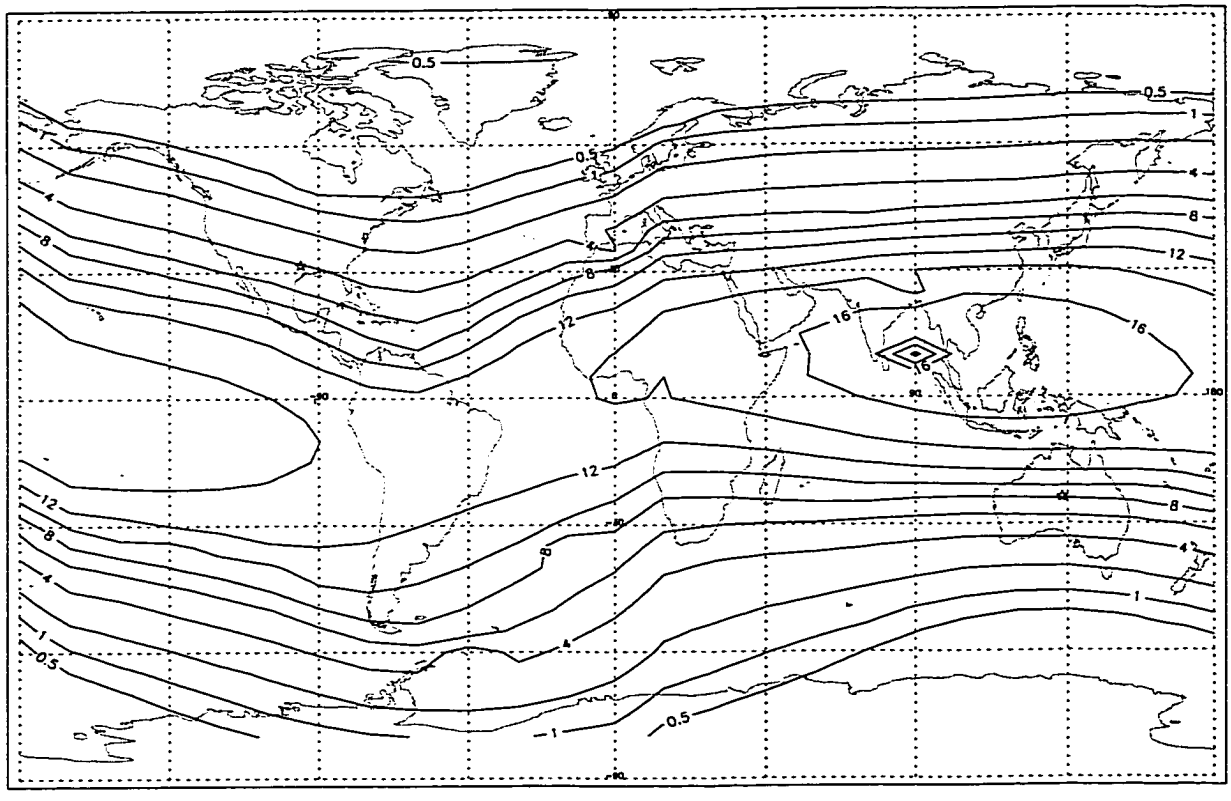

collection hardware to ignore the resultant spurious events. A channel of the *GRATIS* scaler is assigned to count these events (cf. table 2.3, p. 23).

We now find the approximate flux of charged particles through the immediate vicinity of the detectors and through the crystals themselves. We will use this number in our calculation of the neutron (§3.4.4) and activation (§3.4.5) backgrounds.

The at-float-altitude charged-particle (CP) rate measured by the veto shields for the Alice Springs flight was around 3000 cts s^{-1}. If we assume the CP flux is isotropic (as a first-order approximation), the ratio of the flux through the crystals to the flux through the CP shields is the ratio of the area of the crystals to the area of the shields.

There are five charged-particle (CP) shields. They form a top-open box of dimensions $40'' \times 40'' \times 22\frac{1}{8}''$:

		area	
no. slabs	dimensions	sq. inches	sq. cm
1	$40'' \times 40''$	1600	10323
4	$40'' \times 22\frac{1}{8}''$	885	5710

Since the configuration is a box, the four side panels are about equivalent to two orthogonal panels. We make the additional approximation of ignoring the shadows (overlap). Thus the area of the shields is 21742 cm^2 ($= 2 \times 5712\ cm^2 + 10323\ cm^2$).

The total area of the crystals is 1262 cm^2 (= 5.22 cm × 6.909 cm × 35 tubes = 36.06 cm^2 × 35). Their total volume, given a thickness of 2 mm, is 252.4 cm^3.

To find the flux through the crystals, we scale the number of veto-shield detected charged particles by the fraction that pass through both shields and crystals.

We now have an approximate ratio of areas to scale the charged particle flux:

$$3000 \text{ cts/s} \times (1262 \text{ cm}^2/21742 \text{ cm}^2) = 3000 \times 0.0580 = \boxed{174 \text{ particles/sec} = F_p}$$

So, in one second somewhere around 174 charged particles pass through the crystals. (For the ~ 30 hours of the flight this is $\sim 2.26 \times 10^7$ protons passing through the crystals.) These events, of course, are the ones that are vetoed.

3.3 Source function construction

3.3.1 Cosmic Diffuse Background

Zombeck (1990, p. 197) gives a multi-instrument fit for the energy spectrum of the cosmic diffuse background (keV cm^{-2} s^{-1} keV^{-1} sr^{-1}) for 2.0 keV < E < 1000 keV. Finding the photon flux ($\phi = I/E$) in photons cm^{-2} s^{-1} keV^{-1} sr^{-1} is a simple matter:

$$\phi(E) = \begin{cases} 8.5(E/1 \text{ keV})^{-1.40}, & E \leq 18.5 \text{ keV} \\ 167(E/1 \text{ keV})^{-2.38}, & E > 18.5 \text{ keV} \end{cases} . \quad (3.1)$$

For comparison Schönfelder *et al.* (1977) gives a multi-instrument fit to the diffuse gamma-ray spectrum 0.2 MeV $< E <$ 200 MeV: $\phi(E) = 1.1\times10^{-2}(E/1\text{ MeV})^{-2.3}$ photons cm^{-2} s^{-1} MeV^{-1} sr^{-1}.[3]

Atmospheric absorption marks the difference between the raw cosmic spectrum and that incident on *GRATIS*. We need an expression for the diffuse flux the telescope encounters as a function of zenith angle and photon energy that accounts for attenuation by the atmosphere at a given altitude (atmospheric depth).

The *slant depth*, or atmospheric depth along the line of sight, is proportional to the vertical depth d and to an angular factor $s(\theta)$. For small zenith angles, θ, $s(\theta) \sim \sec\theta$. Simple geometrical arguments give a more general expression for a finite atmosphere, which approximates the angular factor for the real atmosphere (cf. figure 3.3):

$$\begin{aligned} s(a,\theta) &= \sqrt{b^2\cos^2\theta + 2b + 1} - b\cos\theta \\ \text{with } b &= \tfrac{R_e+a}{h} \end{aligned} \tag{3.2}$$

where a is the altitude in km, $R_e = 6378.14$ km is the equatorial radius of the Earth and $h = 25$ km is the 'height' of the atmosphere, derived by fitting to Zombeck's plot of atmospheric depth *vs.* zenith angle (p. 229). (The angular factor for obtuse zenith angles is easily calculated after noting that the depth *beneath* a point and that above

[3]More recent work by Kinzer *et al.* (1997) rejects Compton telescope and high-energy scintillation-detector data, and fits HEAO1-A4 10 keV $< E <$ 400 keV data to $dN/dE = (2.62 \pm 0.05)\times10^{-3}(E/100\text{ keV})^{(-2.75\pm0.08)}$ photons cm^{-2} s^{-1} keV^{-1} sr^{-1}.

it sum to the depth at the Earth's surface, 1000 g/cm^2.) A simpler approximation to the same curve is given by

$$s(\theta) = \frac{a+1}{a+\cos\theta}, \text{ where } a \approx 0.03 \tag{3.3}$$

This is the form we use below. Figure 3.3 compares the two expressions for slant-depth factor against numerical integration of a simple atmospheric model.

So we have this expression for the flux the telescope receives through the atmosphere as a function of zenith angle and photon energy:

$$\begin{aligned} f(E,\theta;d) &= \exp\left(-\mu(E)d\tfrac{a+1}{a+\cos\theta}\right)\phi(E) \\ &\text{where} \\ d &= \text{atmospheric depth} \\ \theta &= \text{zenith angle} \\ \mu(E) &= \text{atmospheric absorption coefficient} \\ \phi(E) &= \text{cosmic diffuse flux, eqn. 3.1} \end{aligned} \tag{3.4}$$

We resume our consideration of the diffuse background in §3.4.1 in our estimation of its contribution to the background signal in *GRATIS*.

3.3.2 Atmospheric gamma-rays

The dominant channel for photon creation in the upper atmosphere for $E < 10$ MeV is bremsstrahlung from atmospheric and re-entrant albedo electrons. Gamma-rays from Compton-scattered π^0 decay constitute less than one percent in this energy range (Graser & Schönfelder, 1977).

Figure 3.3: Comparison of expressions for slant-depth factor s to numerical integration of simple atmospheric model $\rho(z) \propto \exp(-z/\lambda)$, where $\lambda = (39 \text{ km}/\ln(1000/3.5)$ and $z = r - R_e$. Equation 3.2 is plotted as a *dashed line* and is virtually coincident to the numerical result for $\theta \lesssim 60$. Equation 3.3 with $a = 0.03$ is plotted as a *dotted line*. *Inset* is a magnification of the plot for smaller angles. Note that the numerical integration results are practically independent of altitude for any altitude of interest to balloons payloads. Cf. Zombeck (1990), p. 229.

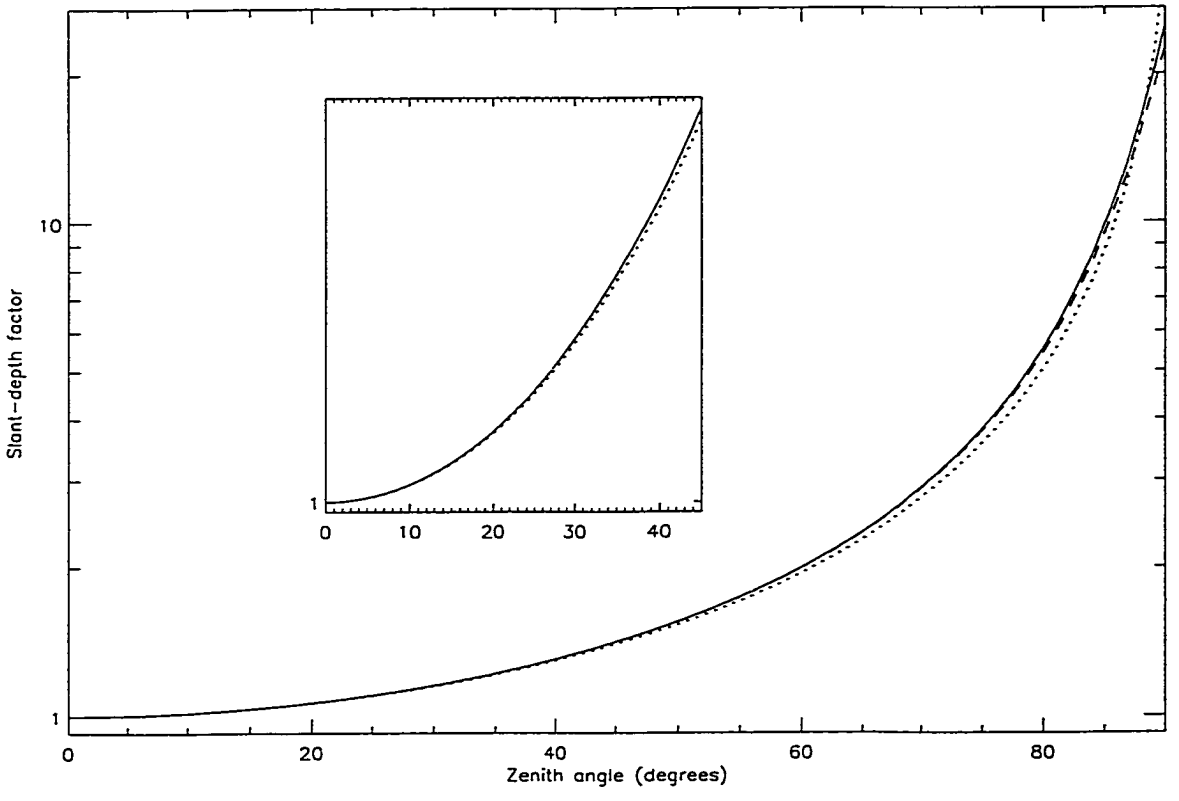

As with the cosmic diffuse background, we need an expression for the flux on the telescope as a function of zenith angle, θ, and photon energy, E, along with the depth dependence of the flux.

On the experimental level, the division of the sky into both energy and angular bins makes it difficult to accumulate enough data for good statistics in the relatively short duration of a balloon flight.

It is difficult to get a coherent theoretical picture of the atmospheric background as the complex particle interactions in the upper atmosphere are not well understood. Early theoretical work by Beuermann (1971) and Daniel & Stephens (1974) began to tackle the problem, but under-predicted photon fluxes in broad energy ranges. The work of Thompson (1974a) studied photons above 30 MeV and was able to generate the observed atmospheric depth dependences. A more mature Monte Carlo treatment by Graser & Schönfelder (1977) was able to reproduce the $\sim 120°$ maximum in the angular distribution, but fell short of the observed downward and upward fluxes. Despite limited successes, no one theoretical treatment has been able to assemble a comprehensive picture of gamma-radiation in the upper atmosphere.

An early effort sought to obviate this difficulty with a simple analytic theory. Ling's 1974 "Semiempirical Model" (cf. Peterson *et al.*, 1973; Ling, 1975) depends on

the simple ansatz of an isotropic source function to derive zenith-angle distributions, spectra, and growth curves for atmospheric gamma-rays. Unfortunately the only data available to test his model came from his own omnidirectional counter. It should not be surprising that Ling's shot in the dark misses, as most decisively shown by the angular distributions and growth curves of Ryan *et al.* (1979).

We now review the most pertinent published atmospheric background data in the downward, upward, and horizontal directions. The remainder of the chapter uses these data to derive a parametric approximation to atmospheric background for use in our simulation of the background radiation in *GRATIS*. This model is similar to that of Costa *et al.* (1984), but is unique in that it extends down to 20 keV and its construction depends exclusively on actual data, without relying on Ling's specious angular deconvolutions.

Downward flux

Gehrels (1985) fits the data of Kinzer *et al.* (1978), Schönfelder *et al.* (1980), Ryan *et al.* (1977), White *et al.* (1977) and the previously unpublished data of Kinzer between 24 and 31 keV to give the *total* downward gamma-ray flux in photons/cm^2 s

sr MeV for 5 g/cm^2 over Palestine, Texas[4]:

$$f(E) = \begin{cases} 1.20\times10^{3}(E/1\text{ MeV})^{1.28}, & E \leq 0.03781\text{ MeV} \\ 5.88\times10^{-2}(E/1\text{ MeV})^{-1.75}, & E > 0.03781\text{ MeV} \end{cases}$$

And the flux for 3.5 g/cm^2:

$$f(E) = \begin{cases} 2.19\times10^{2}(E/1\text{ MeV})^{0.7}, & E \leq 0.03586\text{ MeV} \\ 5.16\times10^{-2}(E/1\text{ MeV})^{-1.81}, & E > 0.03586\text{ MeV} \end{cases}$$

Subtracting the atmospherically attenuated diffuse flux gives this expression in photons/cm^2 s sr keV:

$$f(E) = \begin{cases} 4.92\times10^{-8}(E/1\text{ keV})^{3.38}, & E \leq 37.32\text{ keV} \\ 3.76(E/1\text{ keV})^{-1.66}, & E > 37.32\text{ keV} \end{cases} \tag{3.5}$$

for atmospheric flux alone, found by fitting the linearly interpolated flux points for 4.0 g/cm^2. This expression is consistent with the $1 < E < 30$ MeV spectrum in Schönfelder *et al.* (1980, figure 10).

For high altitudes, that is to say, atmospheric depths less than 100 g/cm^2, the downward vertical gamma-ray flux increases linearly with depth.[5] (By symmetry arguments, flux is proportional to slant depth for small zenith angles.)

[4]Recall that the intensity of atmospheric gamma rays varies inversely with the geomagnetic cutoff rigidity, so atmospheric background should be about half as strong in Alice Springs as Palestine.

[5]This is true at least down to a few MeV according to Ryan *et al.* (1979). In contrast the power-law fits of Gehrels (1985) give an exponent on the depth-dependence that hovers around 0.6, varying with energy and approaching unity only above 20 MeV. We prefer Ryan's explicit measurements of depth-dependence.

Upward Flux

There are several sources of data on the upward gamma-ray flux. Costa *et al.* (1984) reason that upward directed photons in the upper atmosphere have constant intensity with depth. The growth curves of Ryan *et al.* (1979) support this conclusion above 100 g/cm^2 for photon energies 3–5 MeV.

Imhof *et al.* (1976) have satellite data ($\pm 45°$ collimation) that gives the power-law index[6] for 40 keV $< E <$ 2.7 MeV and $\theta \approx 180°$:

$$\alpha = \begin{cases} 1.34 \pm 0.03, & \text{polar cap} \\ 1.39 \pm 0.08, & \text{equatorial region} \end{cases}$$

The balloon data of Ryan *et al.* (1977) for $3 < E < 20$ MeV at Palestine, Texas give a spectral index of $\alpha = 1.48 \pm 0.17$ for $140° < \theta < 170°$. The same data set gives $\alpha = 1.53 \pm 0.41$ for $160° < \theta < 170°$. Notwithstanding the fit of Ryan *et al.* (1979) to the data in their figure 7 to an index of $\alpha = 1.75 \pm 0.12$, the data of the same figure with $E < 10$ MeV can be fit with α as low as 1.40 in agreement with the 1977 fit.[7]

Since the satellite results have more precision and agree with both sets of Ryan's data, the spectral index of upward flux must be somewhere in the range 1.35 to 1.50.

[6] In this work, $\alpha \equiv -PLI$.

[7] Meanwhile, the index for his 10 MeV $\leq E \leq$ 20 MeV data is 3.08.

Figure 3.4: Upward atmospheric gamma ray model compared to fits of Imhof *et al.* (1976) and data of Ryan *et al.* (1977). Error bars on the fit lines are estimated from data points in figure 5 of the former, and merely give an idea of the possible fits.

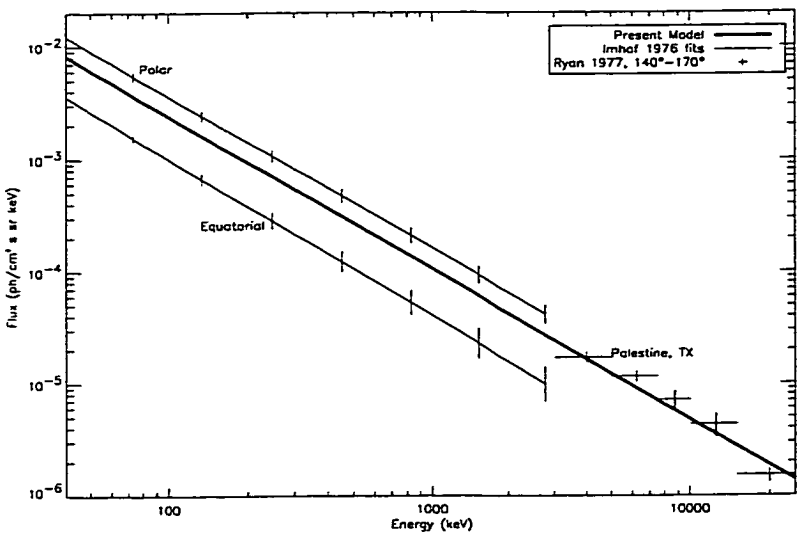

To approximate the upward flux at the middle latitude of Palestine, Texas, we perform a weighted average on the power-law fits to the polar and equatorial data of Imhof *et al.* (1976) to find in photons/cm^2 s sr keV:

$$f(E) = 1.2(E/1\text{ keV})^{-1.35}. \tag{3.6}$$

Figure 3.4 compares this expression to the Imhof *et al.* (1976) fits and to the $\gtrsim$ MeV data of Ryan *et al.* (1977) from Palestine. At higher energies ($E \gtrsim 10$ MeV), the power-law steepens, in agreement with the satellite data of Thompson *et al.* (1981) for $E > 35$ MeV.

Other published data (e.g. Graser & Schönfelder, 1977; Agrinier *et al.*, 1992) give slightly higher power-law indices ($\sim 1.7 - 1.8$). At higher energies, the spectrum falls off more steeply, which is consistent with the data of Ryan *et al.* (1979) for $E > 10$ MeV. Notice that the Ryan *et al.* (1977) data points in figure 3.4 also seem to fall off more sharply above this energy. Since the main concern of the present model is the lower energy part of the spectrum, the lower index of 1.35 allows for good compromise between simplicity and accuracy.

Horizontal Flux

Few data exist for the range $50° < \theta < 140°$, which is in the blind spot (annulus) of the Compton telescopes that produce the bulk of the data.

Schönfelder *et al.* (1977) used a pivoting Compton telescope to examine this angular region. Unfortunately the statistics of their data were not sufficient for a spectrum, but only a histogram of flux $1.5 < E < 10$ MeV binned in zenith angle (their figure 10). They *were* able to combine their 1.5–30 MeV data with the > 30 MeV data of Fichtel *et al.* (1969) to find $\alpha = 1.55$ for $\theta = 112°$. (Using the same technique they derived a power-law index for upward flux of 1.45.)

A fit to the theoretical predictions of Graser & Schönfelder (1977, figures 4, 5 and

6) is not helpful, as the power-law index fluctuates rapidly in the range ~ 1.4 to ~ 2.0. Also, their upward gamma-ray power-law index is ~ 1.7 (as is their downward index), which seems to indicate that they are missing some key elements from their simulation. (An interesting feature of the results is that the horizontal maximum shifts with increasing energy toward 90°, evidence of Compton scattering of the original gamma-rays.)

Agrinier *et al.* (1992) has data points for $\theta \approx 90°, 135°$ binned in 4–10 MeV, 10–25 MeV, and 24–45 MeV. For $\theta \approx 90°$, the power-law index to differential flux is 1.83, which would seem to imply that the index rises with zenith angle before falling. The fit to the upward flux of their experiment gives an index of 1.80—different from the preponderance of the other groups—which casts some doubt on their horizontal result.

So the extent of *dependable data* in the horizontal direction is figure 10 of Schönfelder *et al.* (1977).[8] Schönfelder *et al.* (1980) note that "between 3 and 10 MeV the previous [1977 downward] fluxes are lower [than the downward fluxes in the 1980 paper] by a factor of 1.5–2."

[8]Future work can perhaps deduce the total depth dependence of the horizontal distribution by subtracting the upward and downward fluxes from Peterson and Ling's published growth curves for total (over 4π sr) flux at various energies for 0.3 MeV $\leq E \leq$ 10.0 MeV (Ling, 1974, figure 2.2).

Comparing the 1.5–10-MeV flux in figure 8 of the 1977 paper to the same from table 5 of the 1980 paper gives us a factor of 2.46 to correct the 1977 downward flux.[9] In constructing our model, we assume the same factor holds for other zenith angles.

Empirical Model

For the model of atmospheric background employed in the present work, we adopt a form similar to that of Costa *et al.* (1984). Like Costa, we note the flux should be approximately constant for $\theta < 40°$ and that the maximum in the angular distribution from Schonfelder's data occurs at $\theta \approx 110°$.

For downward flux, we use equation 3.5. For upward flux, we use equation 3.6. We note that Ryan and Schonfelder's data sets both show an exponential increase in flux as the zenith angle decreases from 180°. Schonfelder's horizontal maximum is $\sim$ 2.5 times his upward flux, and for simplicity's sake we assume that this holds at all energies. We also assume that the power-law index remains constant with angle, analogous to the downward case.

For zenith angles between 40° and 110° we linearly interpolate the power-law depth

[9]The total of the downward flux in the 1.5–10-MeV range given from the data points in figure 8 of the 1977 paper is $\sim 6.21\times10^{-3}\gamma/cm^2$ s sr at 2.5 g/cm^2. The total in this range given by table 5 in the 1980 paper is 6.10×10^{-3} γ/cm^2 s sr (g/cm^2). Please note that the latter is depth-normalized, viz. $(g/cm^2)^{-1}$.

Table 3.1: Parameters of the Empirical Atmospheric Model.

Parameter	$E < 37.3$ keV	$E \geq 37.3$ keV
D_0	1.23×10^{-8}	0.940
D_1	3.38	-1.66
A_1	0.9025	
A_2	0.3087	
B_1	-17.51	-1.047
B_2	13.42	0.8023
C_1	4.269	-0.2798
C_2	0.1100	-1.446
U_0	1.2	
U_1	-1.35	
U_2	1.393	

dependence between the known dependences: linear (index=1) for the downward flux and constant (index=0) for the upward flux. We similarly interpolate the flux normalization and the spectral index to insure continuity.

The resulting model for atmospheric background gives the atmospheric flux in photons $\mathrm{cm}^{-2}\ \mathrm{s}^{-1}\ \mathrm{keV}^{-1}\ \mathrm{sr}^{-1}$:

$$f(E,\theta;d) = \begin{cases} D_0 d E^{D_1}, & 0^\circ \leq \theta \leq 40^\circ \\ D_0 d^{A_1 w + A_2} E^{C_1 w + C_2} e^{B_1 w + B_2} & 40^\circ \leq \theta \leq 110^\circ \\ U_0 E^{U_1} \exp\left[U_2(1+w)\right], & 110^\circ \leq \theta \leq 180^\circ \end{cases} \tag{3.7}$$

where E is the energy of the incident photons in keV, d is the atmospheric depth in $\mathrm{g/cm}^2$, $w = \cos\theta$, and θ is the zenith angle in radians. Using the empirical constraints derived in this section and requiring continuity in E-, θ-, and depth-dependence, we find the values of the parameters listed in table 3.1.

Figure 3.5: Comparison of the present model's angular distribution to data of Ryan *et al.* (1977) and Schönfelder *et al.* (1977). The zenith-angle distribution of the latter, plotted as a histogram, is multiplied by a correction factor of 2.46, as noted in text.

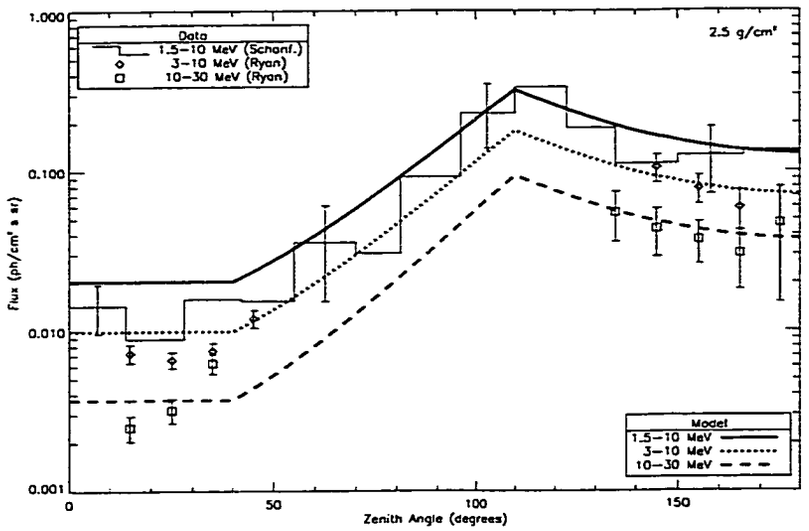

Figure 3.5 compares the model to the data of Ryan *et al.* (1977) and of Schönfelder *et al.* (1977).

We resume our consideration of the atmospheric gamma-ray background in §3.4.1 in our estimation of its contribution to the background signal in *GRATIS*.

3.4 *GRATIS* Background Estimation

We would like to find the contribution of each type of radiation to the background spectrum of *GRATIS*, as depicted in figure 3.6. We describe our estimation of each

Figure 3.6: The mysterious *GRATIS* background spectrum.

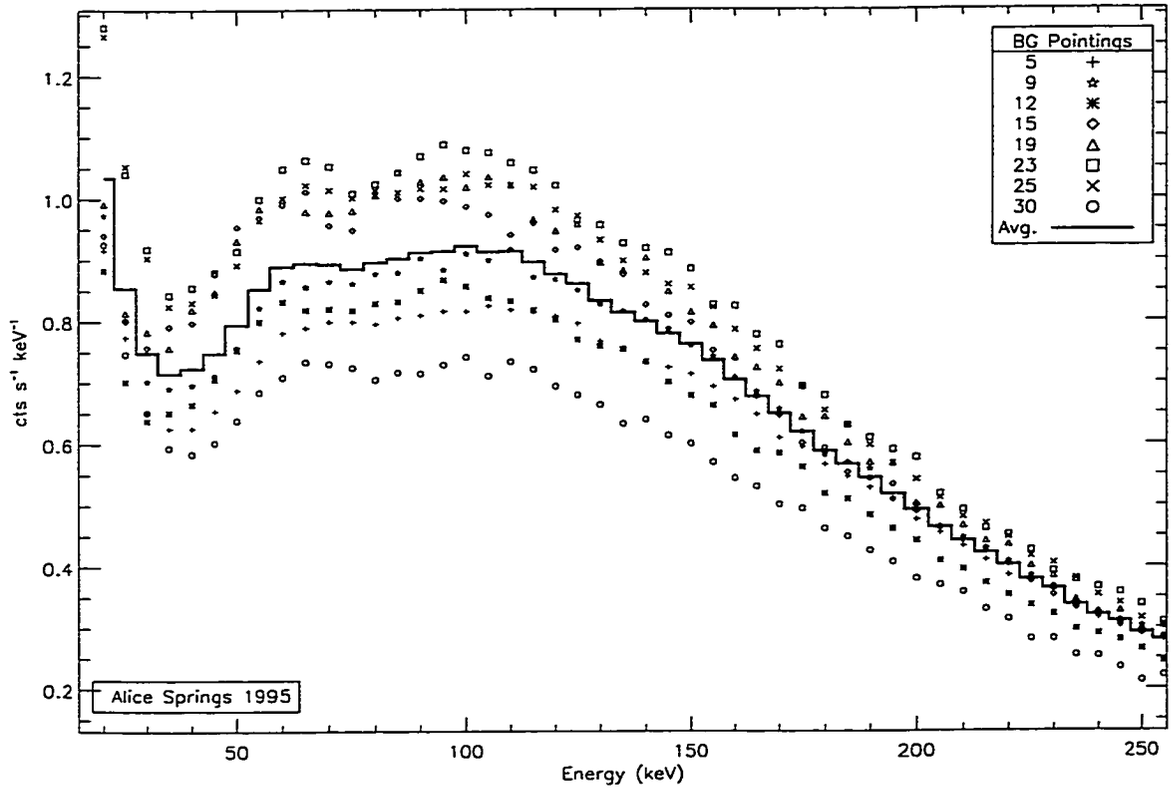

of these in turn.

3.4.1 Diffuse Background

Cosmic Diffuse Background

From §3.4.1, eqn. 3.4, p. 55 we have this expression for the cosmic diffuse flux transmitted through the atmosphere to the telescope as a function of zenith angle and

photon energy:

$$f(E,\theta;d) = \exp\left(-\mu d\frac{a+1}{a+w}\right)\phi(E),\ 0<\theta<\pi/2$$

where d is atmospheric depth, $w = \cos\theta$, θ is the zenith angle, $\mu = \mu(E)$ is the atmospheric absorption coefficient, and $\phi(E)$ is the cosmic diffuse flux above the atmosphere (eqn. 3.1, p. 53).

A good approximation to the absorption coefficient is

$$\mu(E) \approx 5500(E/1\text{ keV})^{-3.1} + 0.9(E/1\text{ keV})^{-0.39}\text{ cm}^2/\text{g} \tag{3.8}$$

This expression is good to better than 10% for $3.5 < E < 3000$ keV and to better than 20% for $3 < E < 50$ MeV— ample for our application.

For the purpose of our Monte Carlo code, we need to integrate the flux expression $f(E,\theta)$ over at least one of the variables[10]:

$$\begin{aligned}
F(E,\theta) &= \int_0^\theta f(E,\theta')\sin\theta' d\theta' \\
&= -\phi(E)\int_1^w \exp\left(-\mu d\frac{a+1}{a+w'}\right)dw',\ 0\le w<1 \\
&= \phi(E)(1+a)\int_1^{\frac{1+a}{w+a}} \exp(-\mu y d)\frac{dy}{y^2} \\
&= \phi(E)(1+a)\left[E_2(\mu d) - \frac{a+w}{a+1}E_2\left(\mu d\frac{a+1}{a+w}\right)\right]
\end{aligned}$$

[10]We omit the trivial azimuthal integral.

$$= \phi(E)(1+a)\Big[\exp(-\mu d) - \frac{a+w}{a+1}\exp(-\mu d\frac{a+1}{a+w})$$
$$-\mu d\Big(E_1(\mu d\frac{a+1}{a+w}) - E_1(\mu d)\Big)\Big]$$

where $w = \cos\theta$. In the last step we have used Abramowitz & Stegun (1972), eqn. 5.1.14.

Results

To simulate the conditions for the GRS 1758–258 observation, we used an atmospheric depth of 3.50 g/cm^2 with an elevation angle of 70°. Figures 3.7 and 3.8 show the source distribution of cosmic diffuse photons as emitted.

Figure 3.7: Zenith-angular distribution of Monte Carlo-produced cosmic diffuse background photons for $E > 7$ keV.

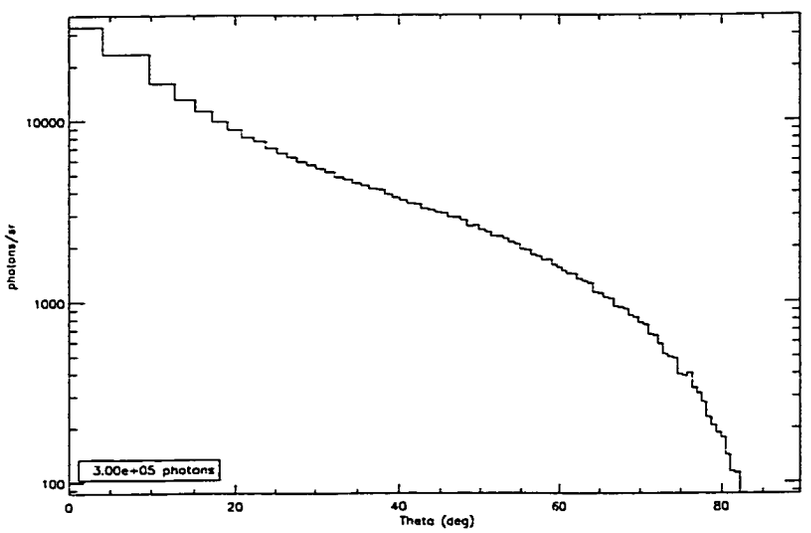

Figure 3.8: Contour plot of distribution of Monte Carlo-produced cosmic diffuse background photons in zenith angle and energy. A minimal smooth has been applied to make the contours more distinguishable.

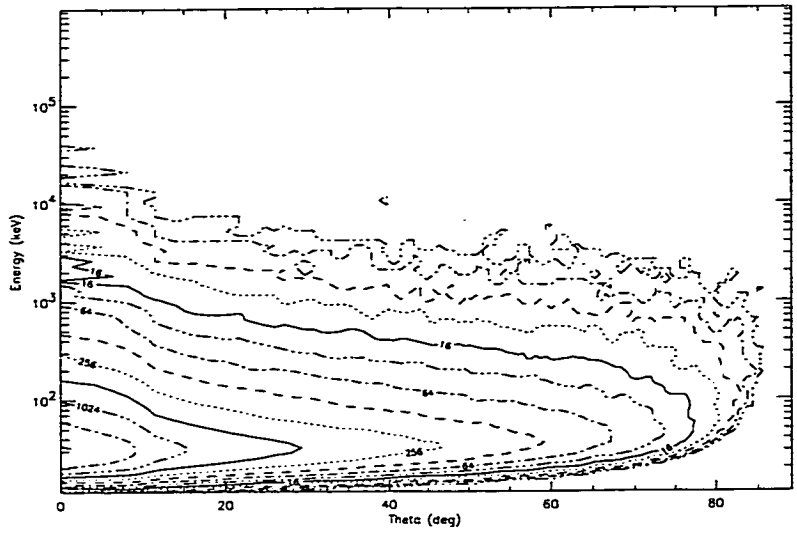

To fit the entire *GRATIS* problem the emitting sphere centered on the crystal plane would have to be at least 400 cm in radius. Unfortunately this required too many photons and too long a run time. To speed the simulation we shrank the gamma-ray emitting sphere to 40 cm (the number of photons required for a given interval of problem time goes as r^2). The side effect was to speed COG (since simplified geometries run faster) by omitting everything except for the tube shield-fine collimator assembly of one tube. The drawback is that the simplified geometry omits some important features of *GRATIS*, most notably the masks and the coarse collimators. To first order the effect of removing the latter is simply to widen the field of view in

the non-imaging direction (cf. eqn. 2.1, p. 16):

$$\arctan\left(\frac{5.7\text{ cm}/2}{32.5\text{ cm}}\right) \times 2 = 10.02^\circ \text{ FWHM}.$$

The COG simulation (cf. appendix) of the cosmic diffuse background ran 3.2×10^8 gamma rays with $E > 7$ keV through one *GRATIS* tube at an atmospheric depth of 3.5 g/cm^2 to simulate 3.2×10^4 seconds (nearly 8.9 hours) of problem time. To get a sense of how the entire tube array would respond, we ran two extreme cases—tubes with mutually orthogonal rotations: numbers 9 & 19 (cf. figure 2.4, p. 15).

Table 3.2 summarizes the results and figure 3.9 compares the spectra. As can be seen from the table, the aperture count rates reflect the fact little diffuse flux enters the detector outside the aperture in the *GRATIS* band. In other words, shields effectively block the diffuse flux below $\sim$ 200 keV.

To calculate the total rate for all tubes, we assume that the count rate (in any energy band) of any given tube, i, with rotation angle ψ_i is

$$r_i = r_9 + (r_{19} - r_9)\cos(\psi_i - \psi_{19}).$$

Thus, we get an all-tube rate of 2.8 cts s^{-1}.

Figure 3.9: Monte Carlo simulated PHA spectra from cosmic diffuse photons. The histograms show the Monte Carlo results for $\theta = 0, 10, 20, 30°$, plotted from top to bottom in the ordering of table 3.2.

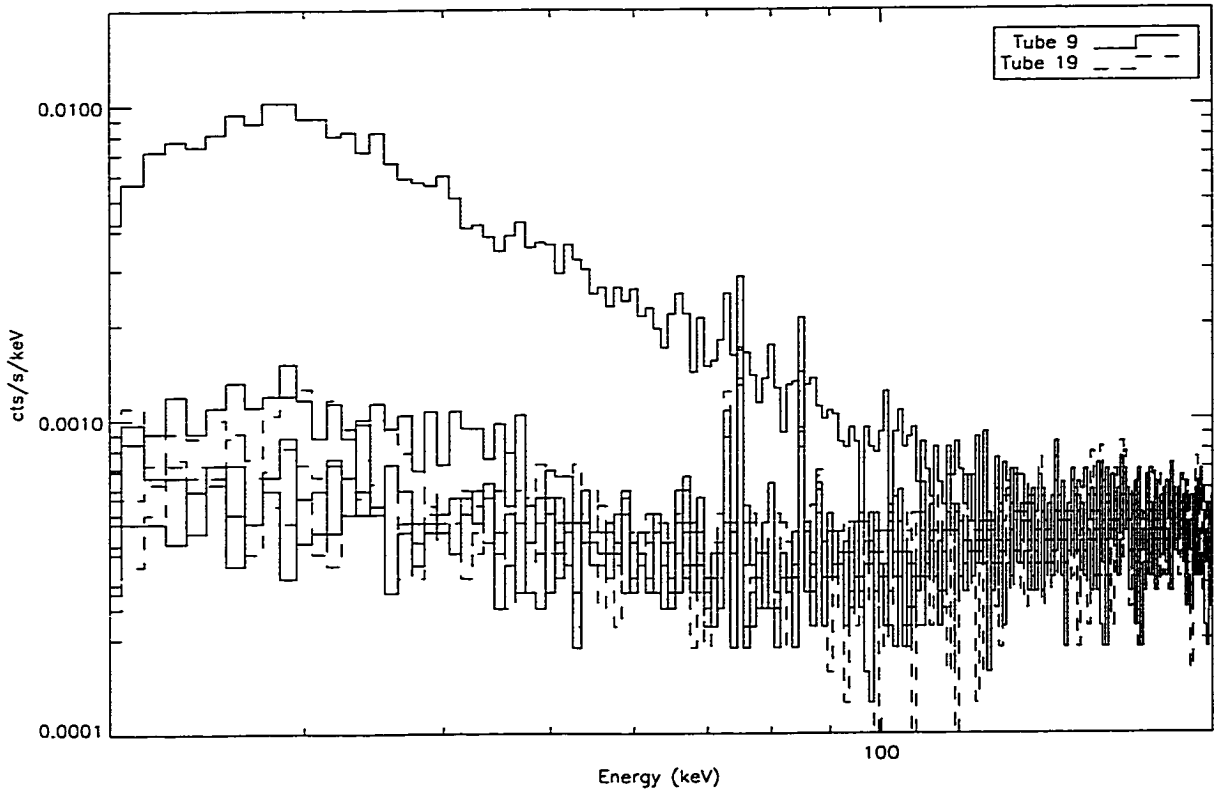

Table 3.2: Results of cosmic diffuse Monte Carlo.

tube no.	zenith angle (degrees)	$E > 7$ keV ct. rate (cts s^{-1})	aperture (%)	$20 \leq E \leq 200$ keV ct. rate (cts s^{-1})	aperture (%)
9	0	$(4.597 \pm 0.038) \times 10^{-1}$	66.5	$(3.391 \pm 0.033) \times 10^{-1}$	81.2
9	10	$(1.896 \pm 0.024) \times 10^{-1}$	18.0	$(9.199 \pm 0.170) \times 10^{-2}$	32.4
19	10	$(1.830 \pm 0.024) \times 10^{-1}$	15.2	$(8.598 \pm 0.164) \times 10^{-2}$	27.3
9	20	$(1.797 \pm 0.024) \times 10^{-1}$	8.8	$(8.116 \pm 0.159) \times 10^{-2}$	16.8
19	20	$(1.832 \pm 0.024) \times 10^{-1}$	8.1	$(8.048 \pm 0.159) \times 10^{-2}$	15.4
9	30	$(1.899 \pm 0.024) \times 10^{-1}$	5.1	$(8.204 \pm 0.160) \times 10^{-2}$	10.0
19	30	$(1.894 \pm 0.024) \times 10^{-1}$	4.9	$(7.841 \pm 0.157) \times 10^{-2}$	9.6

Galactic Diffuse Background

Yamasaki *et al.* (1997) gives the energy spectrum of the Galactic ridge for 1 keV $\leq E \leq$ 100 MeV:

$$\phi(E) = 2.8 \times 10^{-3} \left(\frac{E}{1 \text{ MeV}} \right)^{-2.1} \text{ ph/ cm}^2 \text{ s MeV rad}$$

Valinia & Marshall (1998) give the best fit to the 10–35 keV range of Galactic diffuse emission for observation region R1 (viz. $-45° < l < 45°, -1.5° < b < 1.5°$, see their table 2) as

$$f'(E) = 8.5 \times 10^{-3} \left(\frac{E}{1 \text{ keV}} \right)^{-2.1} \text{ ph keV}^{-1} \text{ cm}^{-2} \text{ s}^{-1}$$

The effective solid angle of *RXTE* is 2.97×10^{-4} sr (V&M, p. 141), thus

$$f(E) = 28.6\left(\frac{E}{1\text{ keV}}\right)^{-2.1}\text{ ph keV}^{-1}\text{ cm}^{-2}\text{ s}^{-1}\text{ sr}^{-1}.$$

Flux from 20 to 200 keV:

$$\begin{aligned} F &= \int_{20}^{200} f(E)dE = \frac{28.6}{1.1}\underbrace{(20^{-1.1} - 200^{-1.1})}_{0.03411} \\ &= 0.8869\text{ ph cm}^{-2}\text{ s}^{-1}\text{ sr}^{-1}. \end{aligned}$$

GRATIS's geometric factor (effective area integrated over its field of view, cf. 2.5, p. 16) is 3.75×10^{-3} cm^2 sr per tube, so the rate received by all 35 tubes (assuming all received the average flux of R1) is

$$\begin{aligned} R &= F \times (3.75\times10^{-3}\text{ cm}^2\text{ sr}) \times 35\text{ tubes} \\ &= 0.116\text{ ph/s}. \end{aligned}$$

So, even assuming 100% detection efficiency, the average Galactic diffuse emission only makes up a small portion of the total *GRATIS* count rate of $\sim$ 160 cts s^{-1}.

Valinia & Marshall deconvolve the detector's latitude response to find the central ridge is made of a combination of thin and broad components. The thin component is $\sim 0.1°$ wide in the 8–35 keV band, and has $\sim$ 2.7 times the average emission in R1. (The broad component contributes less than the average and has a FWHM of $\sim 4.8°$.)

Since this emission is confined to such a small portion of the sky (much smaller than the *GRATIS* field of view), the count rate from this source of background will not even reach this minuscule level for targets along the Galactic ridge. The Galactic background contribution will be even less for GRS 1758–258, since at its latitude of 4.51°, the broad component, not the thin component contributes (cf. §4.1).

3.4.2 Atmospheric gamma-rays

From equation 3.7 (p. 65), our model for atmospheric background:

$$f(E,\theta;d) = \begin{cases} D_0 d E^{D_1}, & 0^\circ \leq \theta \leq 40^\circ \\ D_0 d^{A_1 w + A_2} E^{C_1 w + C_2} e^{B_1 w + B_2} & 40^\circ \leq \theta \leq 110^\circ \\ U_0 E^{U_1} \exp\left[U_2(1+w)\right], & 110^\circ \leq \theta \leq 180^\circ \end{cases}$$

where E is the energy of the incident photons in keV, θ is the zenith angle, d is the atmospheric depth in g/cm^2, and $w = \cos\theta$. Table 3.1 (p. 65) gives the model's parameters.

For all of these expressions, $E_0 = 20$ keV and $E_1 = 37.3$ keV. The primed variables refer to the value of that parameter for $E < E_1$. Because of the observed break in the downward gamma-ray spectrum, these include all parameters in the first two regions, with the exception of those in the exponent of d, viz. A_1 and A_2.

To produce the Monte Carlo code, we must integrate.

Downward: $0° < \theta < 40°$

We first integrate over zenith angle:

$$\int_{0°}^{40} f(E,\theta,d)\sin\theta d\theta = D_0 dE^{D_1}(1-\cos 40°)$$

Now integrating over energy:

$$D_0 d(1-\cos 40°)\left\{\int_{E_0}^{E_1} E^{D_1'}dE + \int_{E_1}^{\infty} E^{D_1}dE\right\}$$

$$= d(1-\cos 40°)\left\{\frac{D_0'}{D_1'+1}(E_1^{D_1'+1} - E_0^{D_1'+1}) - \frac{D_0}{D_1+1}E_1^{D_1+1}\right\}$$

Sampling this distribution is straight-forward using the standard inversion method found in most books on Monte Carlo techniques. The $w = \cos\theta$ coordinate is sampled uniformly, while each E term we sample as a power-law

$$E = E_{\max}\left\{1 + \left[\left(\frac{E_{\min}}{E_{\max}}\right)^a - 1\right]R_2\right\}^{1/a} \tag{3.9}$$

with $a = 1 + \text{PLI}$, $(E_{\min}, E_{\max})$ the minimum and maximum energies, and R_2 a uniform random variate.

Horizontal: $40° < \theta < 110°$

First we integrate over energy:

$$d^{A_1 w+A_2}\left\{\int_{E_0}^{E_1} D_0' E^{C_1' w+C_2'} \exp(B_1' w + B_2') dE + \int_{E_1}^{\infty} D_0 E^{C_1 w+C_2} \exp(B_1 w + B_2) dE\right\}$$

$$= -d^{A_1 w+A_2}\left\{\frac{D_0' \exp(B_1' w + B_2')}{C_1' w + C_2' + 1}\left(E_0^{C_1' w+C_2'+1} - E_1^{C_1' w+C_2'+1}\right)\right.$$

$$\left.+\frac{D_0 \exp(B_1 w + B_2)}{C_1 w + C_2 + 1} E_1^{C_1 w+C_2+1}\right\}$$

Now we integrate over zenith angle to get

$$-d^{A_2}\quad\left\{\frac{D_0' E_1^{C_2'+1} \exp(B_2')}{C_1'} M\left(A_1 \ln d + C_1' \ln E_1 + B_1', \frac{C_2'+1}{C_1'}\right)\right.$$

$$-\frac{D_0' E_0^{C_2'+1} \exp(B_2')}{C_1'} M\left(A_1 \ln d + C_1' \ln E_0 + B_1', \frac{C_2'+1}{C_1'}\right)$$

$$\left.+\frac{D_0 E_1^{C_2+1} \exp(B_2)}{C_1} M\left(A_1 \ln d + C_1 \ln E_1 + B_1, \frac{C_2+1}{C_1}\right)\right\}$$

where

$$M(a,b) = -\int_{\cos 40°}^{\cos 110°} \frac{\exp(aw)}{w+b} dw$$

$$= -\exp(-ab)\int_{x_0}^{x_1} \frac{\exp(aw)}{w} dw$$

$$= \exp(-ab)\left\{\int_{-ax_1}^{\infty} \frac{e^{-t}}{t} dt - \int_{-ax_0}^{\infty} \frac{e^{-t}}{t} dt\right\}$$

$$= e^{-ab}\left\{\mathrm{Ei}(ax_0) - \mathrm{Ei}(ax_1)\right\}$$

and

$$x_1 = \cos 110° + b$$

$$x_0 = \cos 40° + b$$

$$\mathrm{Ei}(z) = -\int_{-z}^{\infty} \frac{e^{-t}}{t} dt = -\int_{-1}^{\infty} \frac{e^{-zt}}{t} dt$$

$$\text{with } |\arg z| < \pi$$

For completeness, here is the integral over zenith angle alone:

$$-\frac{D_0}{a} \left[d^{A_1 w + A_2} E^{C_1 w + C_2} e^{B_1 w + B_2} \right]_{\cos 40°}^{\cos 110°}$$

$$\text{where } a = A_1 \ln d + C_1 \ln E + B_1$$

and the parameters take on the value appropriate (primed or unprimed) to whatever energy is used.

This is the one region whose sampling presents any problem. We remove the constant factors from the flux expression, $f(E, \theta; d)$, for the region:

$$f_{\mathrm{II}} \propto d^{A_1 w} E^{C_1 w + C_2} e^{B_1 w} = e^{\alpha w} E^{C_1 w + C_2}$$

where $\alpha \equiv B_1 + A_1 \ln d$.

We employ the composition technique of Butler (1954), as presented in C140 of Everett & Cashwell (1983, cf. Rubinstein, 1981, ch. 3, ex. 2). First we find a dummy

(or virtual) version, w', of the angular variable:

$$NR_1 = \int_{w_1}^{w'} e^{\alpha w} dw = \frac{1}{\alpha}(e^{\alpha w'} - e^{\alpha w_1})$$

where the normalization $N = \frac{1}{\alpha}(e^{\alpha w_2} - e^{\alpha w_1})$, (w_1, w_2) are the angular limits of this region (viz. $\cos 40°, \cos 110°$), and R_1 is a uniform variate. So

$$w' = \frac{1}{\alpha} \ln(\alpha N R_1 + e^{\alpha w_1})$$

Second we sample E as a power-law as in eqn. 3.9 with constant index $C_1 w' + C_2$, viz. $a = C_1 w' + C_2 + 1$.

Once we have E, we can find the real w:

$$w = \frac{1}{b} \ln(bNR_3 + e^{bw_1})$$

where $b = B_1 + C_1 \ln E + A_1 \ln d$, and R_3 is a uniform random variate.

Upward: $110° < \theta < 180°$

The expression for this region has no depth dependence; the spectral and angular parts are separable.

First we integrate the angular part:

$$-\int_{\cos 110°}^{-1} e^{U_2(1+w)} d(\cos\theta) \;=\; -\frac{1}{U_2}\left[1 - e^{U_2(1+\cos 110°)}\right]$$

Next the spectral part:

$$U_0 \int_{E_0}^{\infty} E^{U_2} dE = \frac{-U_0 E_0^{U_1+1}}{U_1 + 1}$$

Now we combine the two:

$$\frac{U_0 E_0^{U_1+1}}{(U_1+1)U_2} \left[1 - e^{U_2(1+\cos 110^\circ)}\right]$$

Sampling this distribution is straight-forward using the inversion method.

Results

The Monte Carlo simulation of the atmospheric background code produces properly distributed photons much faster than that for the cosmic diffuse simulation, but, reflecting the much greater number of atmospheric gamma-rays in the upper atmosphere than cosmic diffuse gamma-rays, takes much longer to run to simulate the same amount of simulated observation (problem) time. To minimize the run time, I altered the code to produce only photons with $E > 40$ keV. This simplification not only decreased the number of particles the code had to produce for each second of problem time, but it also removed the need to deal with the spectral break, making the code faster for each particle.

Even with this shortcut, the program still had to generate a large number of

photons (7.2×10^4 photons/sec at 3.5 g/cm^2), which requires a lot of computer time. Figures 3.10 and 3.11 show the distribution of atmospheric source photons as emitted.

Figure 3.10: Zenith-angular distribution of Monte Carlo-produced atmospheric background photons for 40 keV $< E <$ 100 MeV.

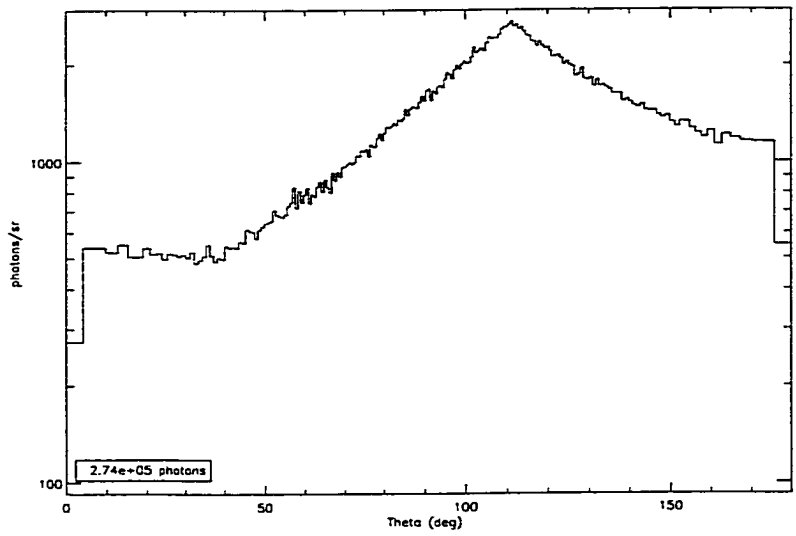

To approximate the conditions for the GRS 1758–258 observation, we used an elevation angle of 70° at an atmospheric depth of 3.50 g/cm^2 for tubes 19 and 9. Recall that tube 19 has its fine collimator slats parallel to $\hat{\phi}$ and tube 9 has its slats parallel to $\hat{\theta}$.

Little flux enters through the apertures, so the results for the two tubes are practically identical. Table 3.3 summarizes our results. Figure 3.12 shows the angular distributions of the detected photons. "Sky coordinates" have the z-axis aligned with

Figure 3.11: Contour plot of the intensity distribution of Monte Carlo-produced atmospheric background photons in zenith angle and energy. A minimal smooth has been applied to make the contours more distinguishable.

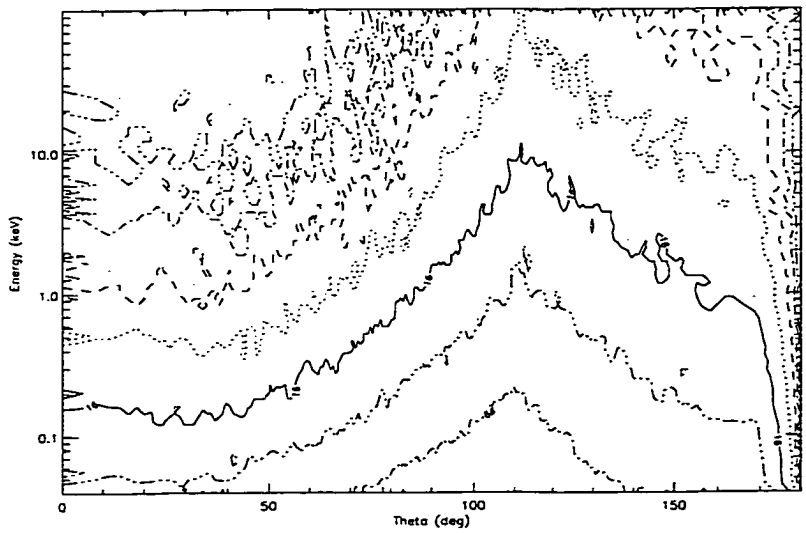

Table 3.3: Results of atmospheric gamma-ray Monte Carlo. "Col'nless" are photons that do not interact before entering the crystal.

tube no.	problem time (sec)	tot. ct. rate (cts s^{-1})	40–200 keV rate (cts s^{-1})	col'nless (%)
9	7.3×10^3	11.60 ± 0.04	3.40 ± 0.02	52
19	4.5×10^3	11.51 ± 0.06	3.40 ± 0.03	52

the sky's zenith and nadir, whereas "problem coordinates" have the z-axis aligned with the tube— in this case rotated 20° from the sky zenith in the y-z plane. Figure 3.13 shows the spectra of the energies deposited in the crystals.

The 73-, 75-, 85-, and 87-keV lines are by and large photons that originate with $200 \lesssim E \lesssim 1000$ keV from all directions (with about the same distribution the total emitted photons, with a maximum at $\theta \approx 110°$) and Compton scatter in the material surrounding the detector 1–3 times before entering the crystal from above ($\theta \lesssim 60°$).

Figures 3.14 show the matrices of in-going and detected background. The general features are about the same for both tubes.

The atmospheric source function was derived for data from Palestine, Texas, which has a cutoff rigidity approximately half of that at Alice Springs, Australia, where our 1995 flight took place. So for Alice Springs we expect count rates half those at Palestine (cf. §3.2).

We extrapolate the 40–200 keV rate down to 20 keV by assuming the average differential rate is the same below 40 keV. Thus we estimate the total 20–200 keV count rate at ~ 68 cts s^{-1}, and the the total flux for $E < 10^5$ keV at ~ 200 cts s^{-1}.

Figure 3.12: Monte-Carlo predicted angular distributions of the detected atmospheric photons.

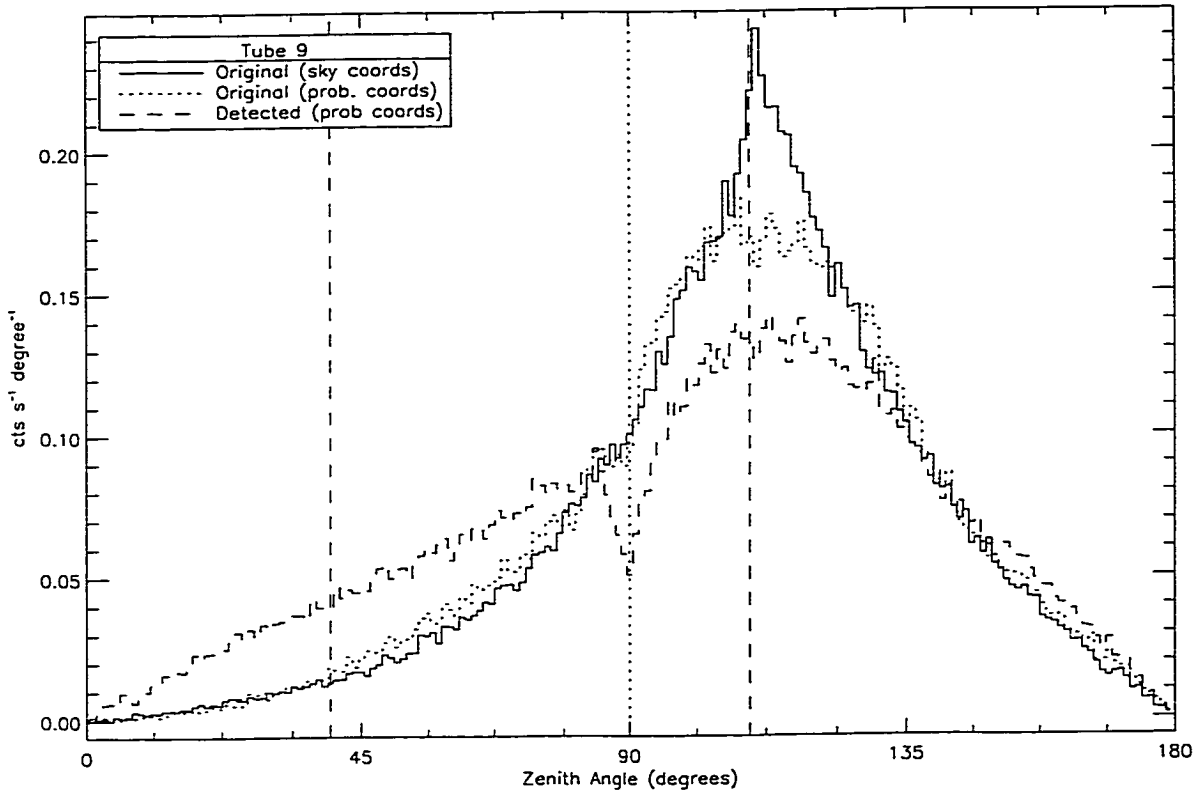

Figure 3.13: Atmospheric gamma-ray spectra from the two tubes. "Compton" are photons that deposit only part of their energy in the crystal.

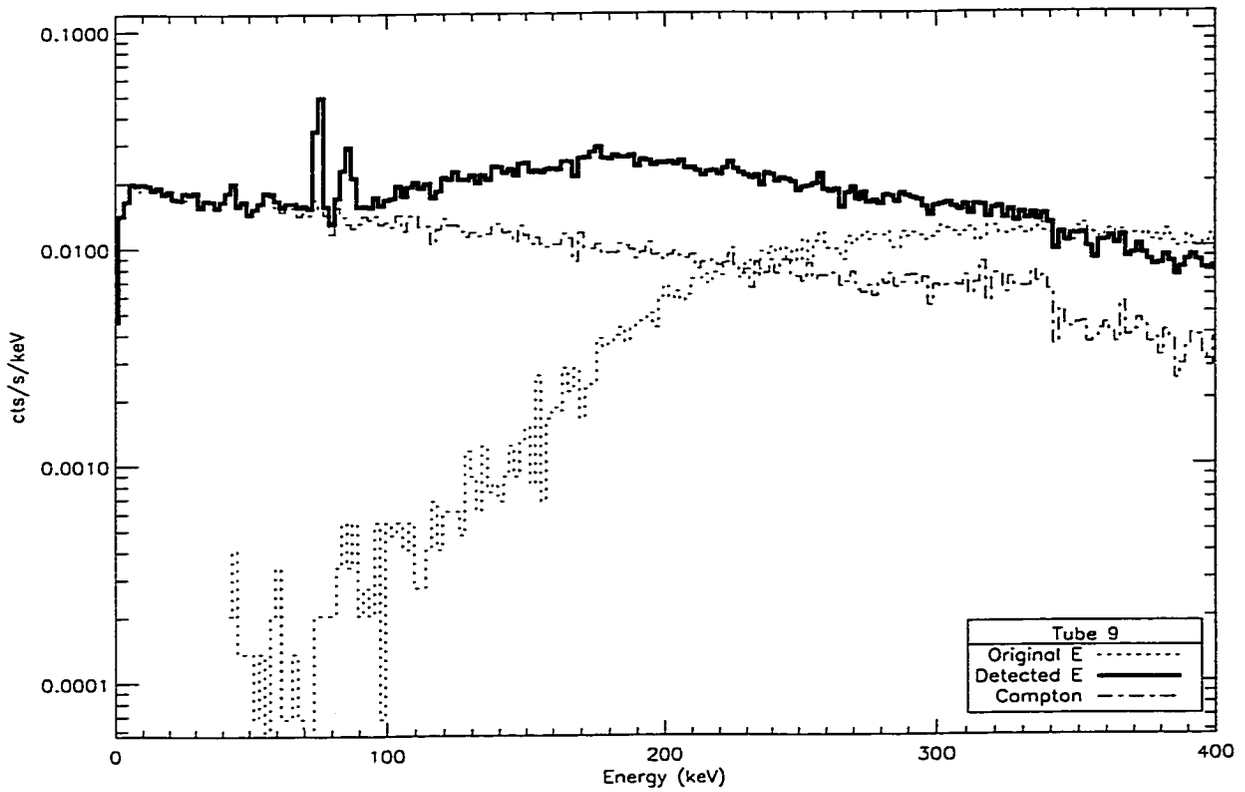

Figure 3.14: Background matrices from the two tubes. The 511-keV line is clearly visible.

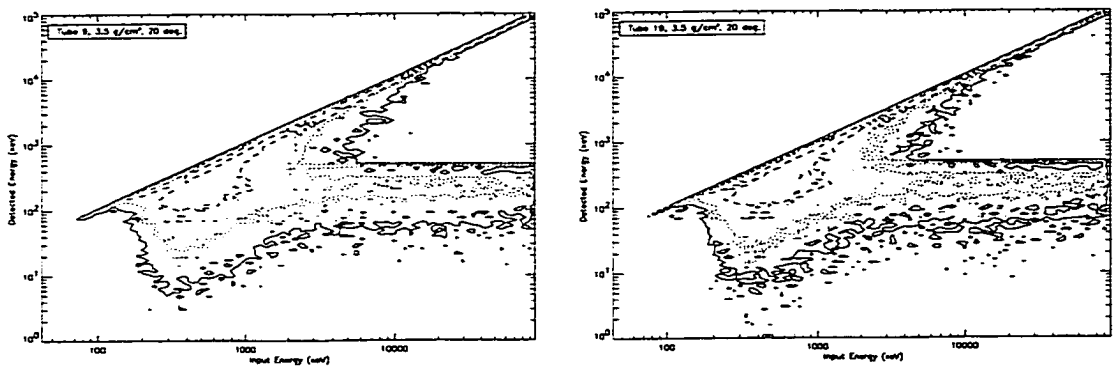

3.4.3 Locally produced photons

The same process that produces gamma-rays in the atmosphere is responsible for the prompt (as opposed to the *delayed*, §3.4.5) gamma-rays produced in the payload.

A reasonable approximation to the cosmic-ray proton spectrum plotted in Groom *et al.* (2000) is in nucleon/m^{-2} s^{-1} sr^{-1} MeV^{-1} (cf. Papini *et al.*, 1996)

$$f(E) = \mathrm{comb}(2.44{\times}10^{-2}E^{0.784}, 1.33{\times}10^{9}E^{-2.68}, 0.35),$$

where E is in MeV and

$$\mathrm{comb}(f_1, f_2, \alpha) = (f_1^{-\alpha} + f_2^{-\alpha})^{-1/\alpha}$$

is the power-law combining function (f_1 and f_2 are the asymptotic forms of the combined spectrum and α controls the sharpness of the knee).

The primary cosmic rays include about a quarter additional nucleons in nuclei of higher atomic number, about 70% of these are bound in helium nuclei. The fractional composition of the primaries is nearly constant with energy. At low residual depths, protons and neutrons constitute the vast majority of cosmic rays, primary or secondary for $E > 1$ GeV, and outnumber the closest rival, electrons, by a hundred-fold. (Groom *et al.*, 2000).

Efforts to integrate a hadronic interaction package into the COG Monte Carlo code that we used to simulate cosmic and atmospheric photons were planned, but had to be shelved because of shifting priorities at Lawrence Livermore National Laboratory (Rich Buck, priv. comm. 2001). So we will have to settle with much rougher estimates of this background.

Recall (§3.2) that in one second somewhere around 174 protons pass through the crystals. These events, of course, are the ones that are vetoed. The events of concern, the unvetoed events, are much less numerous. We now estimate the signal from the unvetoed events.

We trust the designers of *GRATIS* that the CP shield will effectively veto any charged particle that makes it as far as the pressure vessel. Thus we exclude the fine collimator and its shield from consideration as a source of locally generated gamma-

rays. The other two main masses above the detectors are the coarse collimators and the mask. To calculate the gamma-ray flux that these generate, we use the approximation of Dean *et al.* (1991):

$$R = \frac{d_{\text{equiv.}}}{5}\Omega \int_{E_1}^{E_2} f_{\text{atm}}(E, \theta = 0°; d = 1 \text{ g/cm}^2) dE \text{ cts s}^{-1}$$

in photons s^{-1}, where E_1 and E_2 are the bounds of the energy range, f_{atm} is the downward atmospheric flux, $d_{\text{equiv.}}$ is the equivalent depth of the payload masses under consideration, and Ω is the grasp of the detector. Given our model for the downward atmospheric flux (eqn. 3.7), the value of the integral for 20–200 keV is $\boxed{8.76\times10^{-2} \text{ photons cm}^{-2} \text{ s}^{-1} \text{ sr}^{-1}}$.

The mask weighs 250 g and occupies a volume of approximately 100 cm^2, so $d_{\text{mask}} \approx 2.5$ g/cm^2. The grasp of each detector is 3.48×10^{-3} cm^2 sr. So, each mask produces 5.3×10^{-3} photons/sec— a truly minuscule amount, even when multiplied by the 35 tubes.

Each set of coarse collimators weighs 890 g and encloses a volume of approximately 32 cm^2, so $d_{\text{cc}} \approx 28$ g/cm^2. Each detector sees its coarse collimator with a widened field of view, so $\Omega = 2.91\times10^{-2}$ cm^2 sr, which gives 1.41×10^{-2} photons/sec for each tube, or 0.5 photons/sec for all 35 tubes.

We will not bother to estimate the contributions from the minor, purely structural

elements of the payload, the heaviest of which (the "spider" and R^3 pivot that join the payload to the gondola) are outside the field of view of the detectors for all observations, but include these by rounding up our estimation of locally generated background to $\sim$ 1 photon/sec.

3.4.4 Neutron-induced background

Cosmic rays incident on the atmosphere and the payload produce not only electromagnetic cascades, but also neutrons. Significant background can be generated from the gamma-rays of inelastic interactions: excitation (n, γ) and recoil $(n, n'\gamma)$ interactions. The former produces a nucleus excited to $\sim$ 8 MeV, the binding energy of a neutron, above its ground state. Subsequently the nucleus promptly releases four or so de-excitation gamma-rays which can Compton-scatter in the detector. The recoil interaction also excites the nucleus and can release around three de-excitation gamma-rays with mean energies lower than those from the (n, γ) reaction; the photons have low enough energy to be absorbed through photoelectric interactions (Harrison *et al.*, 2001).

Large ambiguities in both the atmospheric neutron flux and the effect of the payload geometry plague the calculation of neutron-induced background. Comparison

of the many measurements and calculations of atmospheric neutrons suggest an overall uncertainty in the energy-integrated flux below $\sim$ 1 MeV of about a factor of two (Harrison *et al.*, 2001). The usual method of calculating neutron flux generated in the payload (local flux) by treating the payload as an equivalent depth of air is fraught with large uncertainties, particularly for a payload, such as *GRATIS*, with large open structures. Additionally the validity of this method is doubtful, since neutron production and moderation are strongly dependent on the atomic weight of the interacting material (Harrison *et al.*, 2001).

Fortunately for *GRATIS* the crystals' mass is small (1.14 kg), so neutrons should have little effect on our observations. A rough estimate of the neutron cross section of our CsI crystals is the area of the nucleons:

$$(1143\text{ g})\times\left(\frac{1\text{ mol}}{260\text{ g}}\right)\times N_A\times\left(\frac{2\text{ atoms}}{\text{molecule}}\right)\times\pi[10^{-13}\text{ cm}\times(\sim 130\text{ nucleons})^{1/3}]^2 = 4.3\text{ cm}^2.$$

So even if the entire 174 particles s^{-1} of CP flux through the crystals (cf. §3.2), along with the $\sim$ 400 cts s^{-1} from the ULD scaler were neutrons, we would see only $570 \times (4.3\text{ cm}^2/1262\text{ cm}^2) = 1.4$ cts s^{-1}— a negligible result compared to the 160 cts s^{-1} in our 20–200 keV bandpass (cf. figure 3.6, p. 67).

Dean *et al.* (1991) give the integral count rate from thermal energies to 10 MeV over Palestine, Texas at 3.5 g/cm^2 of 0.8 neutrons cm^{-2} s^{-1}. In Alice Springs at float,

the rate will be half that. Given the 4.3 cm^2 total nucleonic area of our crystals, that amounts to 1.72 cts s^{-1}, again negligible compared to the total background.

3.4.5 Crystal activation

Cosmic rays incident on the payload convert its component materials into unstable isotopes, thereby activating them. The decay of the activated materials creates a background signal that is delayed, and thus not easily vetoed. Activation of the detector crystals is particularly vexing, as it cannot be shielded.

Naturally, the amount of activation increases with exposure to cosmic rays. Fortunately, the low intensity of the cosmic ray flux prevents the activation from becoming an appreciable source of background, as we now show.

We base our analysis on the summary by Dean, Lei, & Knight (1991, hereafter DLK). Given a proton flux $F_p(t')$ in protons s^{-1}, where t' is some past time, the measured background in cts s^{-1} at time t over the energy range 20–200 keV is

$$W(t) = \int_{20\ \mathrm{keV}}^{200} g(E)dE \int_0^t F_p(t')R(t-t')dt'. \tag{3.10}$$

In this equation we have assumed that $g(E)$, the spectra form of the background radiation from an activated CsI crystal in cts keV^{-1} $proton^{-1}$, is constant in time.

We incorporate the temporal dependence into $R(t')$, the dimensionless time-decay function.

We take $g(E)$ from the empirical work by Carpenter & Dyer (1973). They irradiated a 45.4-cm^3 CsI(Na) crystal with 1.15×10^8 protons ($\equiv 1.09\times10^7$ nuclear interactions) at 155 MeV spread over one minute. Their figure 1 gives the background spectra measured at various intervals after irradiation. Curve (a) is the spectrum after 100 seconds, which we approximate using Hailey's parameterization (notes of May 24, 1992) of DLK's $g(E)$ for $20 \leq E \leq 200$ keV:

$$g(E) = \begin{cases} 8.67(E/20\text{ keV})^{2.06}, & 20 \leq E \leq 30\text{ keV} \\ 20.0, & 30 < E \leq 40\text{ keV} \\ 20.0(E/40\text{ keV})^{-3.29}, & 40 < E \leq 85\text{ keV} \\ 1.67(E/85\text{ keV})^{2.1}, & 85 < E \leq 200\text{ keV} \end{cases} . \tag{3.11}$$

(We have multiplied by a proportionality factor of 6.67×10^9 to match figure 1a.)

DLK reprint the parameterization by Gruber, Jung, & Matteson (1987, conference proceeding) of the time dependent decay function:

$$R(t) = \sum_{i=1}^{6} A_i \exp\left(-t/\tau_i\right) \tag{3.12}$$

The best-fit values for A_i and τ_i are given in table 3.4.

Note that our version of $R(t)$, unlike that of DLK, has already incorporated the

Table 3.4: Parameters of the time-dependent decay function $R(t)$.

i	A_i	τ_i (sec)	$A_i\tau_i$ (sec)
1	18.88	10.90	205.8
2	1.640	102.3	167.8
3	0.3900	673.2	262.6
4	0.02570	3383.	86.94
5	0.01285	1.126×10^4	144.8
6	0.007091	3.842×10^4	272.4
total	20.95	5.386×10^4	1140.

factor[11] $R(t_0) = K_{\rm CsI} = 5.78\times10^6$ into the A_i. Thus, our $R(t)$ is a dimensionless normalization factor that takes on a value of unity at some fiducial time, t_0. For DLK, $t_0 = 3045$ s, but, for the spectrum of Carpenter and Dyer that we have used, $t_0 = 100$ s. This difference only multiplies the τ_i by a factor (100 sec/3045 sec) as we have done, leaving the A_i unaffected.

We now insert the appropriate values from §3.4.3 for *GRATIS* into equation 3.10. For Carpenter and Dyer's crystal of volume 45.4 cm^3, integrating the spectral parameterization over 20–200 keV gives a total count rate of 221 ct/s or 1.92×10^{-6} ct/s/proton. For *GRATIS*'s crystal of volume 252 cm^3 (cf. §3.4.3), that becomes

$$\int_{20\rm keV}^{200} g(E)dE = 1.07\times10^{-5} \text{ ct/s/proton}$$

We approximate the proton flux as constant in time, which allows us to integrate

[11] True to form, DLK's $K_{\rm CsI}$ is high by a factor of 1.30, which we have corrected in the table.

simply $R(t')$:

$$\int_0^t F_p(t)R(t-t')dt' = F_p \sum_{i=1}^{6} A_i\tau_i(1-e^{-t/\tau_i})$$

In the long-term limit ($t \to \infty$), the decay function saturates at $F_p \sum_{i=1}^{6} A_i\tau_i$. We found in §3.2 that the flux through the crystals $F_p \approx 174$ protons s^{-1}. We add to this the ~ 400 protons s^{-1} from the ULD rate.

Assembling the numbers in the original equation (3.10), we find

$$W(\infty) = (570 \text{ protons/sec}) \times (1.07\times10^{-5} \text{ ct/s/proton}) \times (1140 \text{ sec}) = \boxed{3.0 \text{ ct/s}}$$

The background from crystal activation is less than the statistical fluctuations of the full 20–200 keV gamma-ray event rate ($\sqrt{160} \approx 13$ ct/s) alone, and is thus negligible. Even near the beginning of the flight, when the payload passed quickly through the Pfotzer maximum and the CP rate was double that at float, the resultant activation count rate is negligible even in the approximation that this high count rate was sustained throughout a never-ending flight.

We have used the long-term approximation in these arguments. The relatively short duration of balloon flights further reduces the expected activation background far below the level of concern. On top of that, we have treated all charged particles as protons: the actual number of protons would be less by about half.

3.4.6 Summary

Table 3.5: Components of *GRATIS* background

component	20–200 keV (cts s^{-1})
diffuse	~ 2.8
diffuse Galactic	< 0.1
atmospheric	~ 70
local	~ 1
neutron	1.7
activation	$\ll 3$
calculated total	~ 75
observed total	145

Table 3.5 summarizes the results of our background estimation calculations for the *GRATIS* energy band. The dominant component is the atmospheric gamma-rays. Figure 3.15 compares this component to the average observed background spectrum (cf. figure 3.6, p. 67). From this figure, the average observed background rate for $20 \leq E \leq 200$ keV is 145 cts s^{-1}. Keck *et al.* (1996) found that the average 20–200 keV rate was $\sim$ 160cts s^{-1}, assuming the events are Poisson-distributed in time. Our calculations agree in this band to a factor of two with observation (consistent with the less sophisticated simulation of Harrison, 1993) and ranks well among other background estimations in its agreement with observation.

We find excellent agreement in the *GRATIS* band. In a matter of much less

Figure 3.15: Comparison of Monte-Carlo calculated atmospheric background to observed background spectrum (cf. figure 3.6, p. 67) with and without folding through the PSPMT's energy resolution. The calculated spectrum has been halved for Alice Springs.

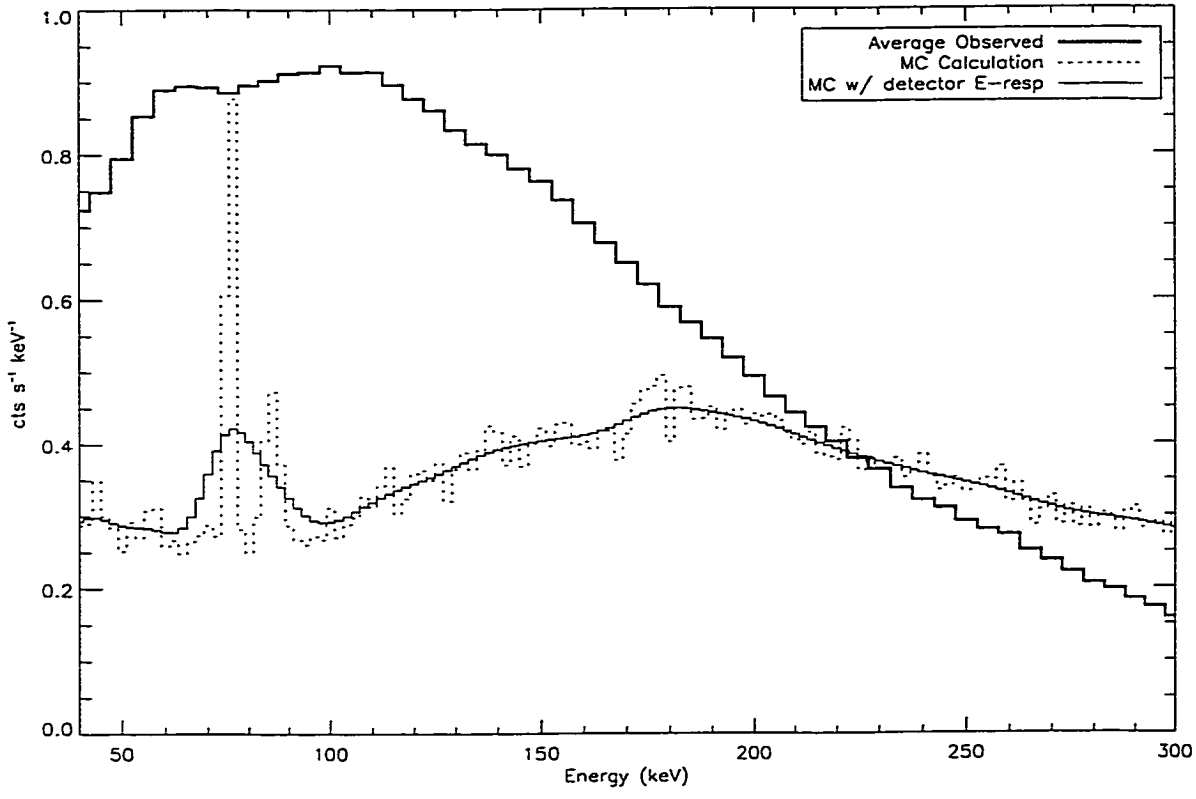

concern, the agreement is not so good for the total observed events. The x-ray scaler rate (all energies) averaged around 1200 cts s^{-1} ($\sim$ 1600 less the ULD's $\sim$ 430 cts s^{-1}), six times higher than the atmospheric simulation's results of $\sim$ 200 cts s^{-1}.

We now turn to possible reasons for the disparities between observation and the Monte-Carlo calculations.

3.4.7 Possible improvements

As previously noted, COG does not propagate electrons (or hadrons) produced in the photon interactions. With effort, COG can be made to interface with the electron-gamma shower (EGS) code to propagate electrons.

Noticeably missing from the background spectrum (figure 3.15) is the characteristic hump from 50–150 keV. A similar hump was observed in the background data of the proportional counter of Ramsey *et al.* (1990).[12] Their Monte Carlo calculations showed that the dominant background component is produced by high energy photons what "have scattered many times in the thick aluminum body. Following their history we see that a typical photon, down-shifted into our energy region, undergoes 3–4 Compton scatters in the aluminum and 0–1 in the tin shields, before being absorbed in the detector, a somewhat surprising result." It is possible that the *GRATIS* simulation is missing just such a component because of the omission of large aluminum structures such as the plate that holds the masks, the supporting structures and possibly the pressure vessel. However, the aluminum in the detector of Ramsey *et al.* (1990) surrounded their detection medium (xenon gas), whereas the aluminum structures of *GRATIS* are more distant, which makes this explanation

[12] A similar hump was seen in the "true detector background" spectrum of Peterson *et al.* (1968), though its origin is not clear.

unlikely to be responsible for many photons.

In retrospect, our approximation of the spectrum at $\theta \approx 110°$ is much too simplistic. Photons from this zenith angle must penetrate very large atmospheric depths ($s(\theta) \geq 1000$). Thus, low-energy photons would tend to scatter into surrounding zenith angles, while the high-energy photons would remain unscattered. The net result is a hardening of the spectrum. This conclusion agrees with the $E > 30$ MeV data of Thompson (1974b), and the simulations of Graser & Schönfelder (1977). Such a high-energy component could easily penetrate the shields and make up the difference between simulation and observation for the total event rate.

Additionally, more higher energy events from the horizontal direction could explain the much smaller discrepancy in the 20–200 keV rate and the lack of the 50–150 keV hump. As noted before (§3.4.2), the $\sim$ 70 and $\sim$ 85-keV lines in the simulated atmospheric gamma-ray spectrum are photons that Compton scatter in the material surrounding the detector before entering the crystal from above ($\theta \lesssim 50°$). A larger presence of these photons in the upper atmosphere could easily account for much of the hump.

Part II

GRS 1758–258

FOR being second only to 1E 1740.7–2942 as the brightest persistent gamma-ray source near the Galactic center, GRS 1758–258 remains something of an enigma. Not only do its remoteness and high column density obscure it, but its relative proximity to GX 5–1, which even now poses a minor obstacle to low-energy ($\lesssim$ 25 keV) observations, delayed its discovery until 1990.

The few established facts about GRS 1758–258 are intriguing. The search for a counterpart in the optical and infrared turned up no distinct result, but only two or more candidates within 1″ (Martí *et al.*, 1998). Even more interestingly, Rodríguez and collaborators, working with the VLA, found not one, but at least three radio sources near the x-ray source that have a roughly jet-like symmetry with respect to it (Rodríguez *et al.*, 1992). This jet-like structure suggests GRS 1758–258, just as its neighbor 1E 1740.7–2942, is a microquasar, but with a lower column density than 1E 1740.7–2942, making it more amenable to observation. GRS 1758–258 also shows similarities to Cyg X-1, in that persistent, low-level hard emission dominates its luminosity.

The *GRATIS* observed GRS 1758–258 in October 1995. In the following chapters, which are an expanded version of Keck *et al.* (2001), we combine data from this observation with published and publicly available data from other high-energy

missions to produce a long-term light curve for the source in the radio and in soft and hard x-rays. We also performed our own re-duction of the VLA data, including several observations without published results. In chapter 4, we enumerate the diverse data sources that we have tapped, and our handling of them. This requires a careful treatment of the 1990–1993 *ROSAT* observations (§4.3), which are the only soft x-ray observations bridging the 1991–1992 hard x-ray dip.

Next we compare the data from the various data sets with each other, and with results of observations of other celestial objects (chapter 5). Most notably, we find (§5.2) no ultra-soft component throughout the twelve years spanned by the soft x-ray observations, which eliminates the possibility that GRS 1758–258 was in the high state at any of those times. We investigate possible correlations of hard x-rays with soft x-rays, hard x-rays with radio, and the hard x-rays with spectral shape.

In chapter 6 we combine the *ROSAT* data with those of *GRANAT* to constrain models of accretion disk emission: the two-temperature model (§6.1), the disk corona model (§6.2), and the ADAF model (§6.3). Finally in §6.4 we show that the ADAF model explains properties of the flux-flux diagram and "X-ray Burster Box" of Barret *et al.* (1996) and evaluate the model in light of the diagram and data of that paper.

Chapter 4

Observations

In figure 4.1 we combine data from many instruments to produce a long-term light curve and spectral index history for the source. The soft x-ray light curve is of unabsorbed flux, that is to say, the flux corrected for interstellar absorption by assuming that the underlying spectrum follows a power-law.

Below we briefly describe each instrument and how the data were derived.

Figure 4.1: Light curve and spectral index history for GRS 1758–258 for 1985–2000. Provenance of miscellaneous data points is given in table 4.1. Photoelectric absorption has been removed from the low-energy x-ray fluxes by assuming the intrinsic spectrum is a power-law that continues to lower energies. Power-law indices with errors greater than 0.4 have been omitted for clarity. The dash-dot lines indicate the "burster-box" boundaries of Barret *et al.* (1996), assuming a distance of 8.5 kpc.

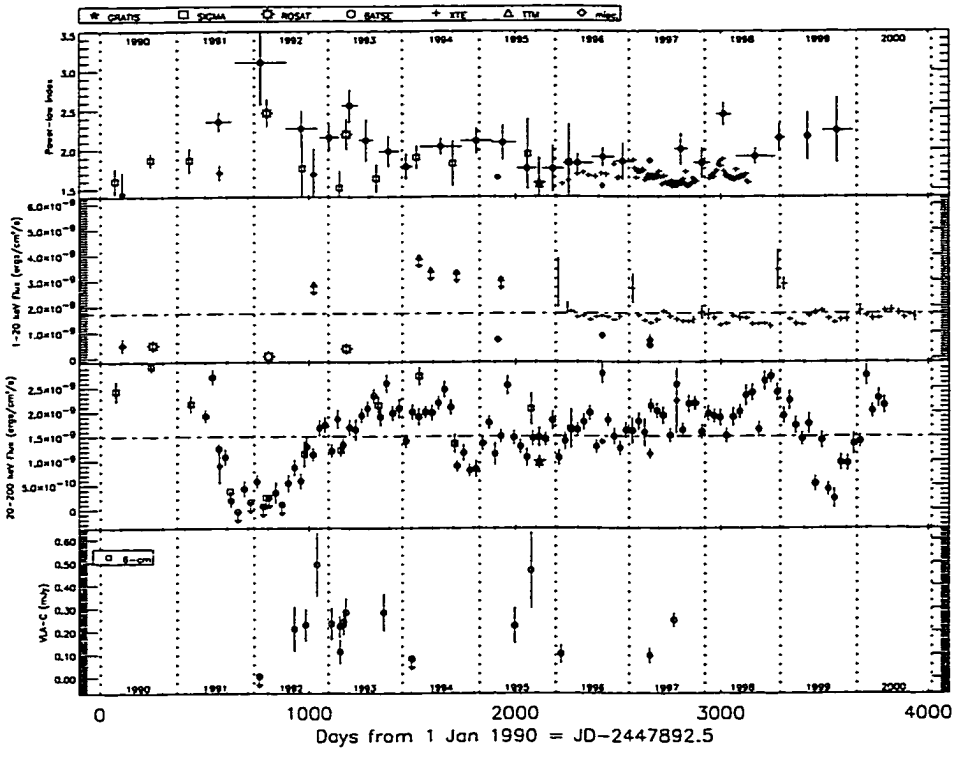

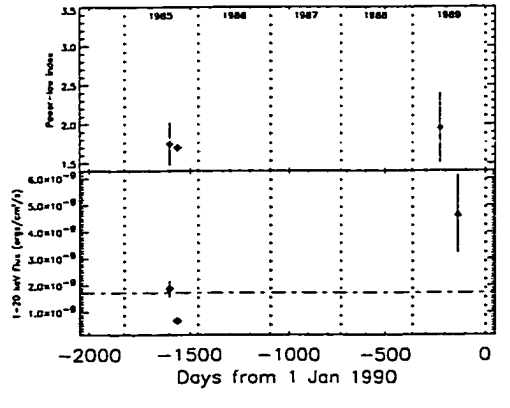

Table 4.1: Miscellaneous data points in figure 4.1

mo	year	day[a]	PLI	err	instrument	citation
Aug	1985	-1599	1.75	0.28	SL2/XRT	Skinner (1990)
Sep	1985	-1562	1.70	0.05	*Exosat*/ME	this work
May	1989	-228	1.95	0.45	POKER	Bazzano *et al.* (1993)
Apr	1990	106	1.44	0.28	*GRANAT*/ART-P	Sunyaev *et al.* (1990b, AIP 232)
Jul	1991	564	1.71	0.10	*CGRO*/OSSE	Jung *et al.* (1993)
Oct	1992	1021	1.69	0.33	KVANT/HEXE	Maisack *et al.* (1993)
Mar	1995	1914	1.65	0.02	*ASCA*/SIS	this work
Aug	1996	2419	1.54	0.04	RXTE	Heindl & Smith (1998)
Apr	1997	2657	1.65	0.02	*BeppoSAX*/LECS	this work
Apr	1997	2657	1.65	0.02	*BeppoSAX*/MECS	this work
Apr	1997	2657	1.86	0.02	*BeppoSAX*/PDS	this work
Aug	1997	2784	1.55	0.04	HEXTE&OSSE	Lin *et al.* (2000)

[a] referenced to 1 Jan 1990 = JD 2447892.5

4.1 *GRATIS*

GRATIS observed GRS 1758–258 from 5:43 to 6:43 hours UT on 17 October 1995. *GRATIS* was launched on its balloon from Alice Springs in the center of the Australian outback at 23.80° S, 133.40° E.

To remove the background contribution, we subtracted the blank-field pointing that immediately preceded this observation (4:43 to 5:43 UT) centered at $\alpha = 17^{\rm h}23^{\rm m}57^{\rm s}, \delta = -37°50'39''$, epoch 2000. This field contains no known high-energy sources. GRS 1758–258 is at $l = 4.51°, b = -1.36°$ whereas the background pointing is at $l = -9.93°, b = -1.03°$. The two fields have comparable contribution from the Galactic diffuse emission, since the longitudinal variation is slow for $l < 10°$ (Iwan

et al., 1982), and the latitudinal variation is nearly flat when $|b| \geq 1°$ (Valinia & Marshall, 1998, figure 2b).

The aspect variables of the on-source and background pointings are very similar. The average GPS-determined altitude of the background pointing was virtually the same as for the on-source, 38.5 km, which corresponds to 3.81 ± 0.08 g/cm^2 residual atmosphere.[1] The elevation angle for background was $\sim 65°$, while the average for the source pointing was 73°. (The slant depth is 3.93 ± 0.09 g/cm^2.) The respective temperatures within the pressure vessel were also similar: temperature of the CAMAC data-collection electronics was 22° C and 25° C and the tube temperatures were approximately 13° C and 15° C for background and on-source respectively (cf. targets 9 & 10 in figure 2.16, p. 43).

We summed and binned the data for 19 tubes (1, 3, 7–9, 12–14, 18, 20–24, 27–28, 32, 33, and 36) for both on-source and background pointings. All of these data were corrected using the extended data pipeline (cf. §2.5.5). We found the source counts by subtracting the background counts (normalized by the ratio of the effective time of each pointing) from the on-source counts. We calculated the effective times of each pointing by histogramming the time interval between events. Since the events are

[1]We have adopted the atmospheric model shown on page 230 of Zombeck (1990). The quoted error is basically the width of the line in that plot.

Figure 4.2: Raw count rate for GRS 1758–258 from *GRATIS* data.

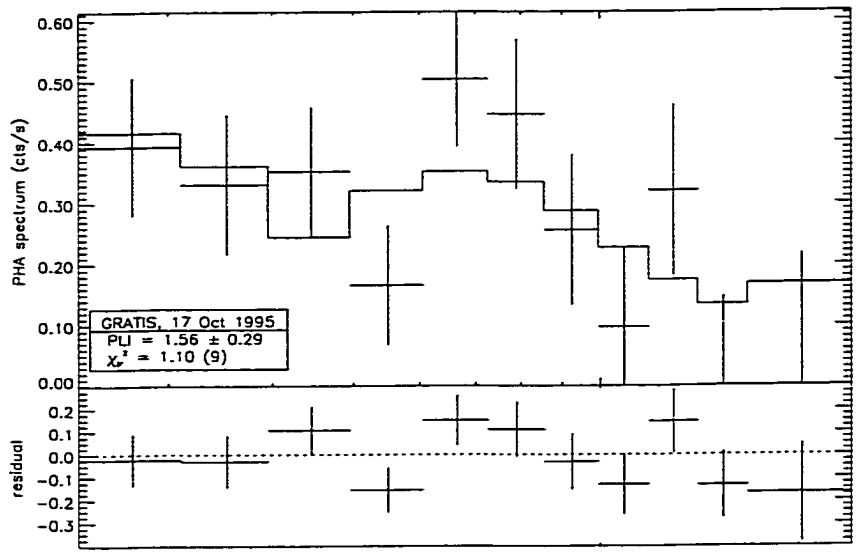

random, the time intervals between them should follow a Poisson distribution:

$$P(n, \Delta t) = \frac{1}{n!} \exp(-\bar{R}\Delta t)(\bar{R}\Delta t)^n$$

is the probability for n events at mean rate $\bar{R}$ in interval of Δt. (In this case $n = 1$.) We fit the histogram to an exponential to find $\bar{R}$, the mean rate for 31.5 μs $< \Delta T <$ 4.00×10^{-2} s (that is, from the x-ray-event dead time to 400 clock ticks). The effective time is then number of events in the pointing divided by the mean rate.

We added the uncertainty in depth to the statistical error of the measured counts by assuming that the source counts originate outside the atmosphere, as we presently

explain.

If $A(E)$ is the on-source pointing count rate at any given energy E and background pointing count rate is $B(E)$, then the source count rate with atmospheric attenuation removed is

$$f(E) \equiv \frac{A-B}{c} \equiv \frac{D}{c}.$$

c is the attenuation factor. The variance is

$$\sigma_f^2 = \frac{\sigma_D^2}{c^2} + \frac{\sigma_c^2 f^2}{c^2}.$$

Now $c(E) = \exp[-\mu(E)x]$, where x is the slant-depth, so $\sigma_c = -\mu\sigma_x c$.

The measured count rate, $g = cf$, and its error do not have the atmospheric attenuation removed, so $\sigma_g^2 = c^2\sigma_f^2$. At last we find the variance of the measured counts that includes the uncertainty in slant-depth:

$$\sigma_g^2 = \sigma_D^2 + \sigma_x^2\mu^2 g^2.$$

GX 5–1 lay just on the edge of the fine-collimator field of view for the source pointing. In principle the rotations of some of the tubes should permit photons from GX 5–1 to fall into the coarse-collimators' $\sim 3°$ field of view. Omitting data counts from these tubes did not significantly alter the 20–132 keV fit.

Figure 4.3: Unfolded spectrum for GRS 1758–258 from *GRATIS* data.

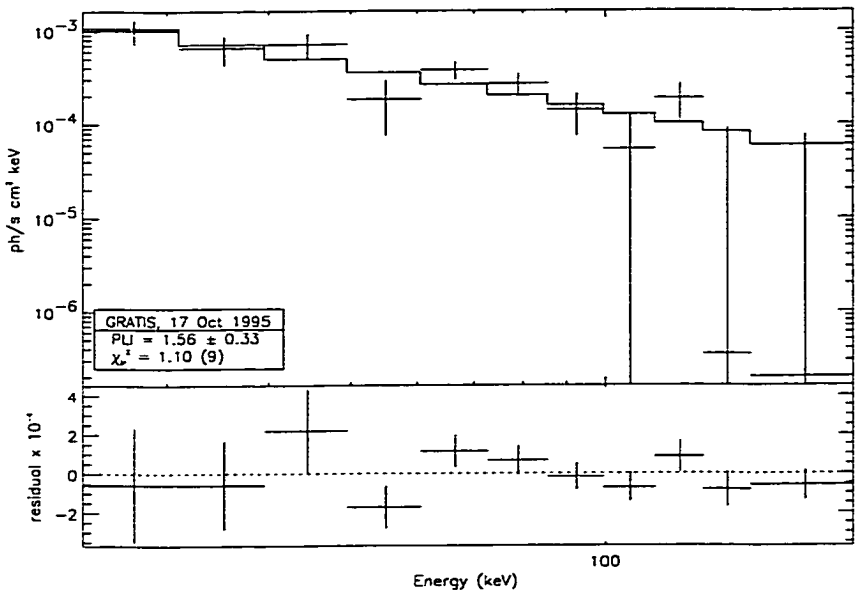

We unfolded the source counts using the standard XSPEC package from NASA's HEASARC. The response matrix (figure 2.14, p. 40) was constructed with a simulation of a *GRATIS* detector using Lawrence Livermore National Laboratory's COG Monte-Carlo photon transport package, as described in §2.6, p. 35ff.

The best-fit power-law model to the data has a photon index of 1.56 ± 0.33 with a reduced χ^2 of 1.08 for nine degrees of freedom, as shown in figure 4.3. The flux was $(9.3 \pm 1.4) \times 10^{-10}$ ergs cm^{-2} s^{-1}. We expect to produce a marginal image of the source, which will be published in Hong (2001) or Hong *et al.* (2001).

4.2 *GRANAT*

The ART-P and SIGMA telescopes on the Russian *GRANAT* satellite discovered GRS 1758–258 in March–April 1990 (Mandrou, 1990, IAUC 5032). *GRANAT* observed the source seasonally through spring 1996.

The French-Russian hard x-ray telescope SIGMA is one of the main instruments on *GRANAT*. SIGMA is a coded mask telescope consisting of a URA coupled to an Anger camera sensitive to photons in the range 30 keV–1.3 MeV. It has an area of 800 cm^2 and a field of view $5° \times 5°$. A more complete description of this instrument is given in Roques *et al.* (1990).

The power-law indices in the plot come from table 1 of Kuznetsov *et al.* (1999). This table contains results of fitting two seasonal spectra a year to a power-law over the range 30–300 keV. Above 150 keV the spectrum decays exponentially. In order to get results comparable to other experiments' fits below 150 keV, we had to band-limit the *GRANAT* photon indices. We fit the spectrum from the sum of their data (shown in their figure 5) below 150 keV in XSPEC to $\alpha = 1.825$, This index is 0.304 less than the power-law index for the full 30–300 keV range. We subtracted this number from each of their table 1 indices to derive the band-limited index for below 150 keV. This

procedure assumes the temporal independence of the spectral shape, an assumption supported by the lack of evidence for change in spectral hardness (Kuznetsov *et al.*, 1999).

The fluxes in the plot were produced by adding to the flux derived from their 40–200 keV luminosities (their table 1), a power-law flux from 20–40 keV, calculated using the just-derived band-adjusted index.

ART-P is another coded-aperture x-ray telescope on *GRANAT*, but sensitive to lower-energy photons: 4–60 keV. Its detectors are four identical position sensitive multi-wire proportional counters. Its field of view is $1.8° \times 1.8°$, and it has an effective area of 1250 cm^2. A fuller description of this instrument is given in Sunyaev *et al.* (1990a). The ART-P data points come from a fit to the 17 April 1990 spectrum published in Sunyaev *et al.* (1990b, AIP 232). As with all of the observations we took from unfolded spectral plots, we fit the data in XSPEC using an identity matrix for the instrument response.

4.3 *ROSAT*

The *Roentgen Satellite* (*ROSAT*) was a cooperative venture of Germany, the U.S., and the U.K launched on June 1, 1990 and deactivated February 12, 1999. Its main

instruments are the Wide Field Camera and the X-ray Telescope. The latter has two focal plane instruments: the Position Sensitive Proportional Counter and the High Resolution Imager.

The Position Sensitive Proportional Counter (PSPC) on board *ROSAT* consists of two units, detector B, used for pointed observations, and detector C, used for the survey. The PSPC has a field of view 2° in diameter and an effective area of 240 cm^2 at 1 keV. It has good sensitivity in the 0.1–2.5 keV range, with energy resolution of $\Delta E/E = 0.43\sqrt{0.93 \text{ keV}/E}$, and time resolution down to $\sim 130\mu$s. A more complete description of this instrument is available in Pfeffermann & Briel (1986). The PSPC was shutdown on September 11, 1994 to conserve scintillation gas and not reactivated until 1997.

The High Resolution Imager (HRI) is composed of two cascaded microchannel plates (MCPs) with a crossed grid position readout system. It has a field of view 38 arcminutes in diameter and an effective area of 80 cm^2 at 1 keV. It has good sensitivity in the same energy range as the PSPC, $\sim$ 2 arcsecond (FWHM) spatial resolution, negligible energy resolution, but timing resolution down to 61μs. The HRI is more fully documented by Zombeck *et al.* (1995).

ROSAT observed GRS 1758–258 in September 1990, March 1992 and spring 1993,

spanning the hard x-ray dip of 1991–1992. In chapter 5, we use these data to constrain the corona models for disk emission and the ADAF model. They are pivotal to our argument that there was no ultrasoft component in 1993 and that the soft and hard x-rays correlated through the 1991–1992 dip.

Two groups have published differing results from their analyses of the *ROSAT*/PSPC's 31 March–2 April 1993 pointed observation of GRS 1758–258: Mereghetti *et al.* (1994) and Grebenev *et al.* (1997, Proc. 2nd Integ. Workshop.).

The original 1994 analysis found a high soft component. The 1997 re-analysis showed a relatively low soft component, and conjectured that the difference comes from "contamination of the field [of the original analysis] by the nearby very bright source GX 5–1." The original analysis took source counts

> from a circular region of radius 18′ centered on the source. Such a large radius is required to collect all the photons scattered by the interstellar dust along the line of sight.... The background has been extracted from five circular regions of radius 13′, located in the external regions of the detector, away from possible contamination by GX 5–1.

On the other hand the 1997 re-analysis "source and background counts were extracted from a circle of radius 5′ and an annulus of radii $10' - 15'$ (both centered at the GRS 1758–258 position)" to exclude contamination by GX 5–1.

Figure 4.4: PSPC image plane. Extracted regions for source and background are circled.

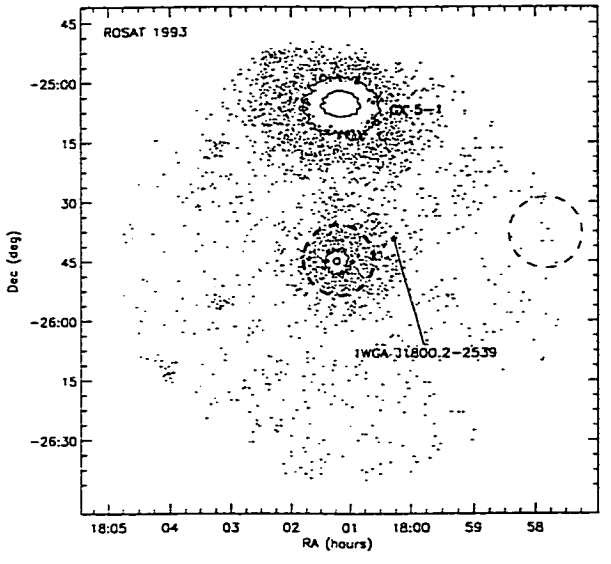

We conducted an independent analysis of the 1993 observation. In order to set the extraction radius for GRS 1758–258 we considered several factors. We wanted to include at least 90% of the photons from the source, taking into account the scattering halo (assumed to scale with that of GX 5–1, Predehl & Schmitt, 1995) while firmly excluding any photons from GX 5–1. In addition we wanted to eliminate any contribution from the brighter background sources, in particular 1WGA J1800.2-2539, located at 13.5 arcminutes from GRS 1758–258. The 18′ source-extraction radius of Mereghetti *et al.* (1994) and in the $10' - 15'$ background-extraction annulus of Grebenev *et al.* (1997) include this source. After examining several trial radii we

compromised on an extraction radius of nine arcminutes, with background selected from a nine-arcminute radius circle centered on GRS 1758–258. To exclude any possible contamination from GX 5–1, we extracted background from an area outside the central ring of the PSPC rather than the usual annular region just outside the central source region. Figure 4.4 shows the PSPC image plane and the extracted regions.

After extraction, the data were fit in XSPEC to a power-law with photoelectric absorption and then to a black-body with absorption, giving the respective best-fit values of $\alpha = 1.75 \pm 0.39$, $N_H = (1.28 \pm 0.13) \times 10^{22}$ cm^{-2} ($\chi^2_\nu = 0.879, \nu = 15$), and $kT = 0.53 \pm 0.06$, $N_H = (0.98 \pm 0.08) \times 10^{22}$ cm^{-2} ($\chi^2_\nu = 0.873, \nu = 15$). Figure 4.5 shows the error contours of our fits. It is noteworthy that the black-body fit is inconsistent at more than the four-sigma level with the standard column ($\sim 1.5 \times 10^{22}$ cm^{-2}) for the source (Mereghetti *et al.*, 1997; Heindl & Smith, 1998; Main *et al.*, 1999). We will more fully address the blackbody fit in §5.2 below, but suffice it to say for now that our fits indicate the black-body component is incompatible with the accepted column for the source.

The count rate for the spring 1993 observation of nearly 7900 seconds was 1.32±.02 cts s^{-1} for 0.1–2.4 keV. The 1990 September 10–12 All-Sky Survey observation of the

Figure 4.5: Confidence contours for fits to March 1993 *ROSAT*/PSPC data: *left* power-law fit; *right* black-body fit.

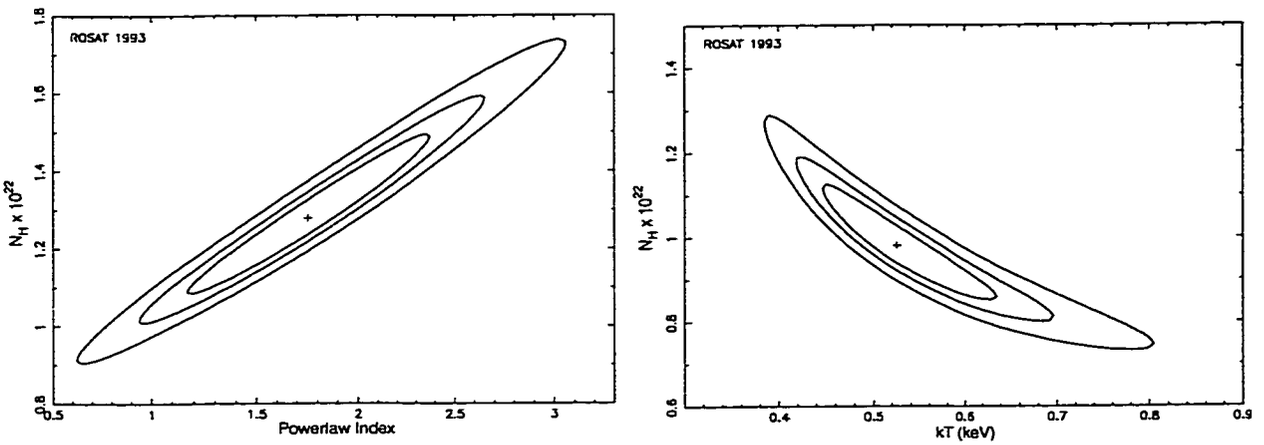

Figure 4.6: Unfolded spectrum from power-law fit to *ROSAT* data.

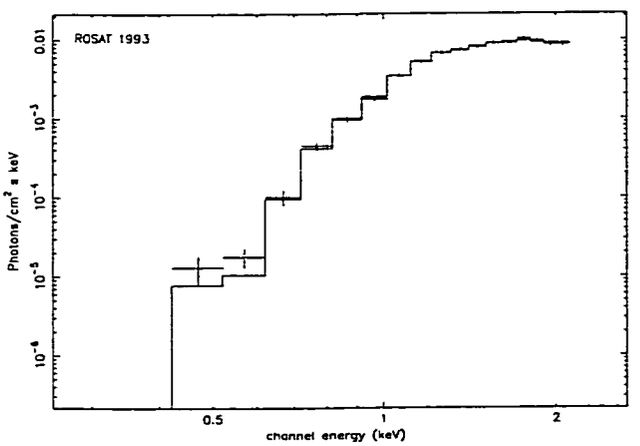

Table 4.2: Unabsorbed 1.0–2.4 keV Fluxes from *ROSAT*
10^{-10} ergs cm^{-2} s^{-1}

Observation Date	Original[a]	Our Re-analysis	Instrument
1990 Sep 10–12	1.4	1.12 ± 0.14	PSPC (survey)
1992 Mar 13	0.76	0.51 ± 0.06	HRI
1993 Mar 31–Apr 2	2.8	$0.82^{+0.11}_{-0.08}$	PSPC

[a] from Mereghetti *et al.* (1994)

source had a slightly higher count rate of $1.81 \pm .12$ cts s^{-1} for the same energy range. This count rate comes from the HEASARC *ROSAT* All-Sky Survey Bright Source Catalog, as revised in 1996, which supersedes the 0.95 ± 0.04 cts s^{-1} reported in Mereghetti *et al.* (1994). The latter paper used that preliminary data to conclude that the "soft and hard spectral components are anti-correlated. Between 1990 September and 1993 March both varied by about a factor of 2, but in opposite directions". Based on the more definitive count rate, we find no anti-correlation, but rather a correlation between the 1990 and 1993 soft and hard x-ray fluxes. The HRI observation 13 March 1992 reported a rate of 0.15 ± 0.01 cts s^{-1}, reasonably close to the 0.18 ± 0.01 cts s^{-1} reported in Mereghetti *et al.* (1994).

No spectral information is available from the 1990 *ROSAT* all-sky survey observation. The HRI data provides no spectral information. Thus we have assumed the 1993 spectral shape for all three observations in deriving the unabsorbed fluxes in table 4.2, which is quite reasonable, given the large error bars on our photon index, which easily encompasses the majority of indices in figure 4.1.

Grebenev *et al.* (1997) found for the 4100-second 5 March 1992 off-axis PSPC observation of GRS 1758–258 a power-law index of 2.47 ± 0.18. In contrast, we consider their flux for this observation to be somewhat suspect since the proper extraction area

is not unambiguous in this distorted region of the focal plane.

In extrapolating *ROSAT* fluxes for figure 4.1, we assume the photon index of 1993 held for 1990 (Mereghetti *et al.* (1994) notes "the source hardness ratios were compatible with those of the 1993 observation"), but we use Grebenev's 2.47 for the 1992 observation.

We performed a power-spectrum analysis of the 1992 off-axis PSPC observation of GRS 1758–258, and the 1993 on-axis PSPC observation (the statistics of the 1990 PSPC and 1992 HRI data were too poor to apply this analysis) using `powerspec` in the FTOOLS package to produce figure 5.3, which is discussed in §5.5 below.

4.4 *CGRO*

The *Compton Gamma-ray Observatory* (*CGRO*) was launched 5 April 1991 and served the astrophysics community for nine years. The mission ended on 4 June 2000, when the spacecraft was directed into the atmosphere after the gyros began to fail. Our analysis used two *CGRO* instruments: BATSE and OSSE.

The Burst and Transient Source Experiment (BATSE) consisted of eight detectors placed on the corners of the *Compton Gamma-ray Observatory* (*CGRO*). The

eight NaI scintillation detectors that constituted BATSE monitored the entire sky for gamma-ray bursts in the 20–1000 keV range.

Accounting for occultation by the earth extends the functionality of the instrument to daily monitoring of bright persistent sources throughout the x-ray sky. BATSE data on GRS 1758–258 was graciously provided by Michael McCollough and Colleen Wilson-Hodge of NASA's Marshall Space Flight Center: the 20–100 keV fluxes and their associated errors were produced by fitting each day's BATSE Earth occultation data to a powerlaw with spectral index 1.8. To extend the energy range of the flux to 200 keV, we ignored the exponential cutoff above $\sim$ 150 keV and simply continued the power-law index of 1.8 out to 200 keV. (We added a 30% correction to better agree with the *GRANAT* fluxes.)

Deriving the photon indices proved more of a challenge. For each viewing period we produced the `.pha` and `.rmf` files with the standard FTOOLS `bod2pha` and `bod2rmf`. We then fit the data from each viewing period to a powerlaw within XSPEC and recorded the results. To give the values plotted in the figure, we performed weighted averages of the spectral indices for each of three periods within each observational cycle. The errors on the indices are large, but their apparent trend is something close to an upside-down cycloid, with a cusp occurring during the hard

x-ray dearth of 1991–1992, and another in the dearth of 1999.

The oriented scintillation spectrometer experiment (OSSE) is made up of four NaI(Tl)-CsI(Na) phoswich detectors sensitive to gamma-rays of energies 50 keV to 10 MeV. Each of the individual 330-mm diameter detectors has a a 3.8° × 11.04° (FWHM) field of view and is independently pointable. More information on OSSE can be found in Johnson *et al.* (1993).

Data for the 12 July 1991 *CGRO*/OSSE observation of GRS 1758–258 were taken from the plot of unfolded flux in figure 4 of Jung *et al.* (1993), whereas those from the 5–19 August 1997 observation came from the HEASARC archive.

4.5 *RXTE*

The *Rossi X-ray Timing Explorer* (*RXTE*) was launched December 30, 1995 and still orbits the earth as a functioning x-ray observatory in the 2–250 keV range.

The *Rossi X-ray Timing Explorer* (*RXTE*) Proportional Counter Array (PCA) is a set of five xenon proportional counters with a 1° FWHM field of view, sensitive to the 2–60 keV energy range with energy resolution of better than 18% at 6 keV. It has a total area of about 6500 cm^2. Further details are given in Jahoda *et al.* (1996).

The PCA power-law indices come from figure 2 of Main *et al.* (1999).

The High Energy X-ray Timing Experiment (HEXTE) consists of two independent clusters of four phoswich scintillation detectors each. It has a total area of approximately 1600 cm^2 and is sensitive to 15–25 keV photons. See Gruber *et al.* (1996); Rothschild *et al.* (1998) for more information on HEXTE.

The All Sky Monitor (ASM) consists of three wide-angle scanning shadow cameras (SSC) equipped with xenon proportional counters. It has a total collecting area of 90 cm^2 and good sensitivity for 2–10 keV. The field of view of each shadow camera is $6° \times 90°$. A more detailed description of the ASM, including its calibration and reduction of its data, is provided in Levine *et al.* (1996). The ASM fluxes presented in figure 4.1 are derived from "quick-look" results provided by the *RXTE*/ASM team and archived at MIT. These light-curves are binned into three energy bands, 1.5–3 keV, 3–5 keV, and 5–12 keV. We converted these to fluxes by comparing the count rates with the average ASM Crab count rates in each channel, and extrapolated to 20 keV using a power-law index from the last two bands. The power-law indices ranged from $\sim 1.7-2$ but have been omitted from the PLI plot because of their large errors (~ 0.8).

4.6 *BeppoSAX*

BeppoSAX is an Italian satellite carrying four narrow field instruments. We use data from three of these. The Medium Energy Concentrator Spectrometers (MECS) are a set of three identical grazing incidence telescopes with position-sensitive gas proportional counters. The counters have an effective area of 150 cm^2 at 6 keV and are sensitive to photons from 1.3–10 keV. The Low Energy Concentrator Spectrometer (LECS) is identical to the MECS telescopes, but with a thin-window proportional counter that allows detection of photons down to 0.1 keV, with effective area 22 cm^2 at 0.25 keV. MECS and LECS detectors have energy resolution of $\Delta E/E = 8/\sqrt{E/6\ \mathrm{keV}}$ FWHM. The collimated Phoswich Detector System (PDS) detects photons in the 15–300 keV band and has an effective area of 600 cm^2 at 80 keV. It has energy resolution $\Delta E/E = 15/\sqrt{E/60\ \mathrm{keV}}$ FWHM.

Data from the 10 April 1997 observation were obtained from the NASA's HEASARC archive and fit in XSPEC to a power-law with (MECS) $N_H = (1.68 \pm 0.05) \times 10^{22}\ \mathrm{cm}^{-2}$, $\alpha = 1.65 \pm 0.02$, $\chi^2_\nu = 1.17$ for $\nu = 95$ and (LECS) $N_H = (1.64 \pm 0.05) \times 10^{22}\ \mathrm{cm}^{-2}$, $\alpha = 1.54 \pm 0.02$, $\chi^2_\nu = 1.13$ for $\nu = 107$. For the PDS data, we found $\alpha = 1.86 \pm 0.02$ with $\chi^2_\nu = 2.19$ for $\nu = 14$. Figure 4.7 shows the unfolded spectra.

Figure 4.7: Unfolded spectra for 10–11 April 1997 *BeppoSAX* observation.

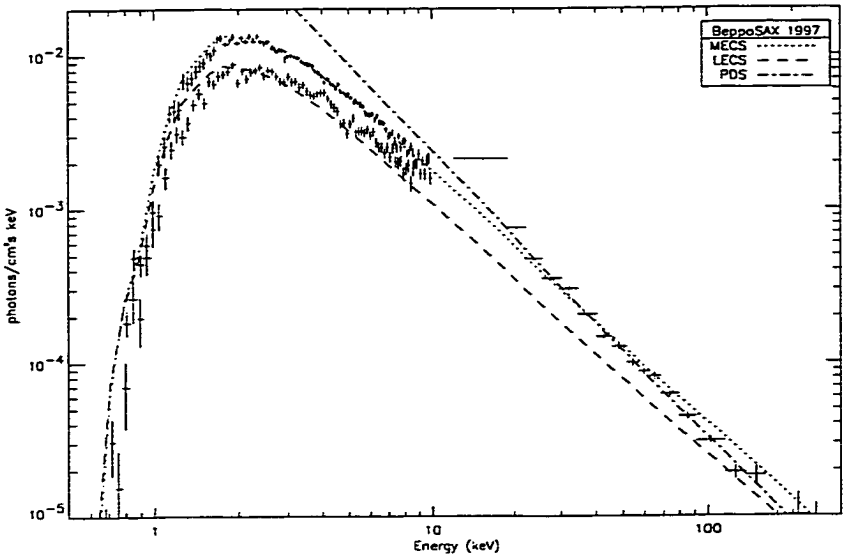

4.7 *Exosat*

The *Exosat*/Medium Energy Proportional Counter (ME) has a 1600 cm^2 area over the 1.2–50 keV range, with $\Delta E/E = 0.2$ at 6 keV. More complete documentation on the ME can be found in Turner *et al.* (1981).

The September 1985 ME data came from the HEASARC archive data for EXO 1757-259, with GRS 1758–258 9.4 arcminutes off-center. The unfolded spectrum is plotted in Skinner (1990). The data file does not list the region of the detector from which the source counts were extracted, but the 45-arcminute field of view (FWHM) of the

ME means that the observation may include contamination from GX 5–1 in addition to the Galactic diffuse emission. Using XSPEC we fit the data to a power-law with absorption: $N_H = (1.79 \pm 0.16) \times 10^{22}$ cm^{-2}, $\alpha = 1.70 \pm 0.05$, $\chi^2_\nu = 0.95$ for $\nu = 61$.

4.8 Other X-ray Data

ASCA is a Japanese mission that consists of four telescopes. Two telescopes focus on the gas imaging spectrometer (GIS), and the other two focus on the solid-state imaging spectrometer (SIS). SIS has a field of view 22″ square and is sensitive to photons from 0.4 to 10 keV with energy resolution of 2% at 5.9 keV. The 285 data points used for the *ASCA*/SIS fit were taken from the plot in Mereghetti *et al.* (1997) and fit in XSPEC with an identity matrix as the response. Our best fit gave us $N_H = (1.46 \pm 0.02) \times 10^{22}$ cm^{-2}, $\alpha = 1.65 \pm 0.01$, $\chi^2_\nu = 1.05$ for $\nu = 282$, which is similar to the $N_H = (1.55 \pm 0.03) \times 10^{22}$ cm^{-2}, $\alpha = 1.70 \pm 0.03$, $\chi^2_\nu = 1.031$ for $\nu = 872$ of Mereghetti *et al.* (1997)

X-ray telescope (XRT) was an instrument flown as part of Spacelab 2 on the space shuttle Challenger 29 July–6 August 1985. XRT used a coded mask to image at energies 2.5–25 keV. Fluxes for Spacelab-2/XRT were calculated with the unfolded flux plot in Skinner (1990). More information on this instrument is available in

Skinner *et al.* (1988).

The TTM telescope aboard the Roentgen Astrophysical Observatory on the Kvant Module of the Russian Mir space station has a geometric area of 655 cm^2 produces coded aperture images in the 2–27 keV band. It has a field of view 15° × 15° and a resolution of 2′. The 1–20 keV flux point and upper limits have been extrapolated assuming a power-law index of 1.8. Our data are taken from the one detection and five upper limits of Aleksandrovich *et al.* (1998).

Also on board the Kvant module on Mir, the High Energy X-ray Experiment (HEXE) consists of four phoswich detectors with a total area of 750 cm^2 and good sensitivity in the range 20–200 keV. The October 17–19, 1992 HEXE observations of GRS 1758–258 come from a fit published in Maisack *et al.* (1993).

For completeness, we mention that the flux of $(0.862 \pm 3.36) \times 10^{-10}$ ergs cm^{-2} s^{-1} and power-law index of 1.95 ± 0.45 from the 15–180 keV POKER instrument (Bazzano *et al.*, 1993). The error bars are far too large to add anything to the plot.

4.9 VLA

Radio fluxes measured by the Very Large Array (VLA) were originally published in Mirabel *et al.* (1992); Mirabel & Rodríguez (1993); Rodríguez *et al.* (1992); Lin *et al.* (2000). As part of our review of the data on GRS 1758–258, we performed our own reduction of the VLA observations of GRS 1758–258, including those in 1994, 1995 and 1996 which have not been previously published. Only in 1997 did the VLA begin observations of GRS 1758–258 at $\lambda = 3.7$ cm, when Lin *et al.* (2000) noted a flat spectral index. We used the classic, 15 October 1999 version of AIPS in our reduction. For all observations the gain calibrator was 1328+307 (a.k.a. 3C 286, 1331+305) and phase calibrator was 1748-253 (1751-253), except for the 3 August 1997 observation, which used 0134+329 (3C 48, 0137+331) for the gain calibrator. The phase calibrator had a boot-strapped flux density in the range 0.47–0.52 Jy.

Our re-analysis is statistically compatible with the previously published results and is summarized in table 4.4. To give a sense of the diffuse "jets" from the source, we have summed the emission in a large enclosing box for observations in those VLA configurations that sample broad spatial frequencies.

Our re-analysis shows that the central source ("VLA-C") persists through obser-

Table 4.3: Previously Published VLA 6-cm data points

date	VLA-C	source
28 Jan–11 Apr 1992	< 0.07[a]	Mirabel *et al.* (1992); Rodríguez *et al.* (1992); Mirabel & Rodríguez (1993)
16 Jul 1992	< 0.11[a]	Mirabel & Rodríguez (1993)[b]
10 Sep 1992	0.48 ± 0.05	Mirabel *et al.* (1992); Mirabel & Rodríguez (1993)
26 Sep 1992	0.58 ± 0.06[c]	Mirabel *et al.* (1992); Mirabel & Rodríguez (1993)
3 Nov 1992	0.30 ± 0.03	Mirabel & Rodríguez (1993)
16 Jan 1993	0.28 ± 0.02	Mirabel & Rodríguez (1993)
27–28 Feb 1993	0.20 ± 0.02	Mirabel & Rodríguez (1993)
19,30 Mar 1993	0.30 ± 0.02	Mirabel & Rodríguez (1993)
3 Oct 1993	0.31 ± 0.02	Mirabel & Rodríguez (1993)
10 Apr 1997	0.09 ± 0.02	Martí (2000)
3–24 Aug 1997	0.14 ± 0.01	Lin *et al.* (2000)
16 Sep 1999	< 0.5	Hjellming (2000) (20-min observation)

[a] 4σ upper limits
[b] The 16 July 1992 flux quoted here supersedes that in Rodríguez *et al.* (1992), according to Luis Rodríguez and Josep Martí (priv. comm., 2000).
[c] Revised to 0.45 ± 0.05 mJy in Martí (1993). The revisions of the remaining flux values in that work are statistically equivalent to those listed here.

vations of any significant duration, excepting the initial 1992 observations during the x-ray dearth. The latter data were taken in the C-configuration, which is insensitive to finer spatial frequencies.

The extended emission is present in all broad-configuration observations (figure 4.8), but the weakness of the source on top of the shifting configurations of the VLA make it difficult to tell how the emission changes or if there is movement among the blobs.

Figure 4.8: Maps from the present data-reduction of VLA observations sensitive to broad spatial frequencies. The large box bounds the region used to sum diffuse emission in table 4.4. The circle is the *ROSAT* error circle. The cross marks VLA-C. Diamonds mark the other field sources. The contours occur at (-1,1,2,4,8,16,32) × 3 × the RMS of the respective map.

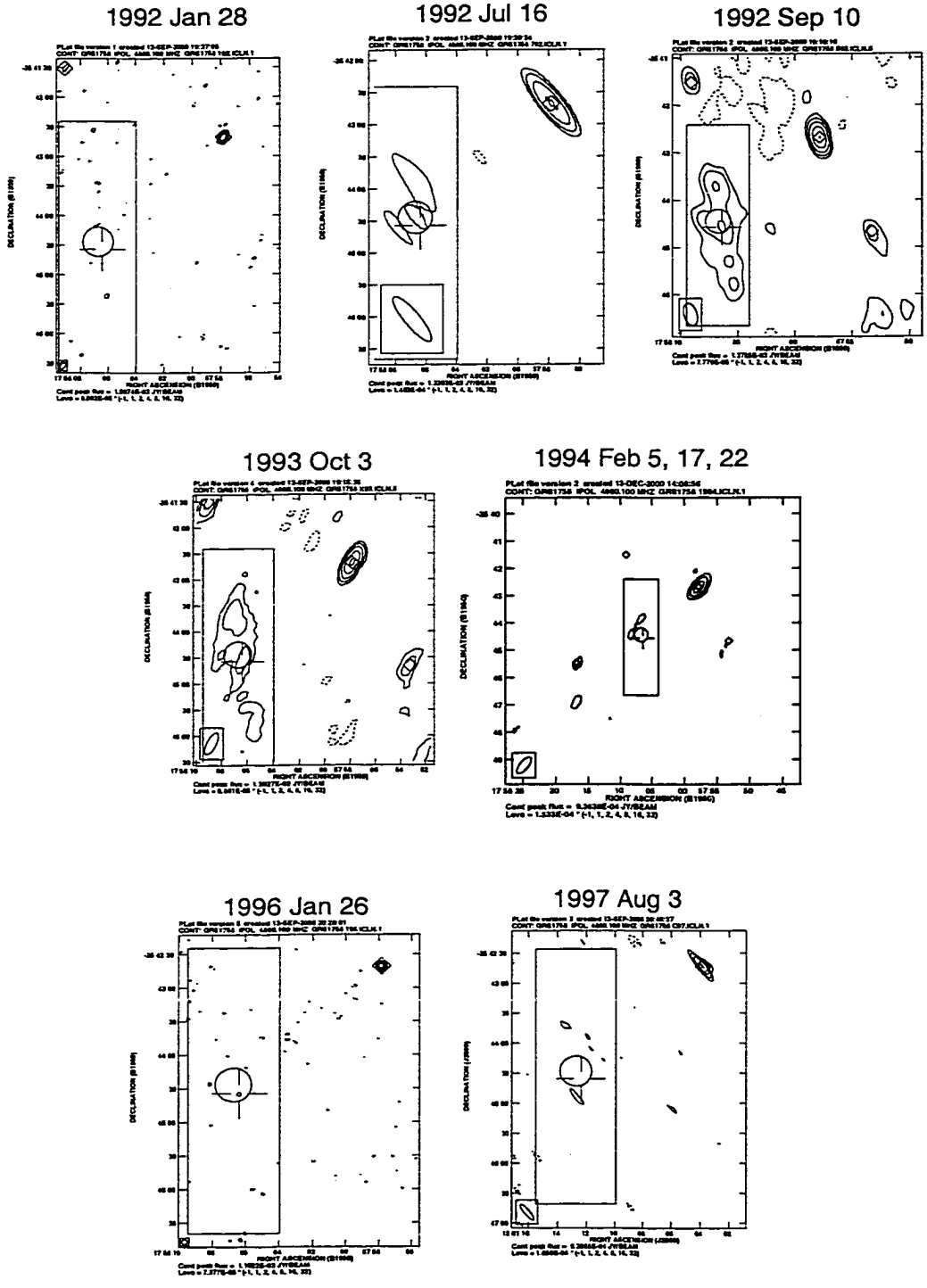

Table 4.4: VLA data points

		Flux Density (mJy at $\lambda = 6$ cm)	
date	VLA config	VLA-C	diffuse[a]
28 Jan 1992	BC	< 0.0048[c]	0.276 ± 0.205
16 Jul 1992	D	0.210 ± 0.098	0.0517 ± 0.177
10 Sep 1992	D	0.228 ± 0.071	0.0601 ± 0.0674
3 Nov 1992	A	0.491 ± 0.139	···
16 Jan 1993	A	0.233 ± 0.071	···
27 Feb 1993	B	0.221 ± 0.047	···
28 Feb 1993	B	0.111 ± 0.052	···
19 Mar 1993	B	0.241 ± 0.055	···
30 Mar 1993	B	0.282 ± 0.064	···
3 Oct 1993	CD	0.282 ± 0.082	0.0548 ± 0.00739
7,13,17 Feb 1994	D	< 0.081[b]	0.0891 ± 0.0263
19 Jun 1995	AD	0.224 ± 0.079	···
5,7 Sep 1995	AB	0.465 ± 0.167	···
26 Jan 1996	BC	0.102 ± 0.041	···
10 Apr 1997	B	0.095 ± 0.034	···
3 Aug 1997	C	0.248 ± 0.032	0.132 ± 0.0863

[a] The value is the sum of the flux densities in a box $85'' \times 25''$ centered at $\alpha = 17^h58^m06.72^s$, $\delta = -25°44'32''$. The error is the magnitude of the negative flux densities in the same box.
[b] The upper limits are the RMS inside a $5'' \times 5''$ box centered at the VLA-C position.

Table 4.5: VLA Map Specifications

date	VLA config	Synthesized Beam size (″)	P.A. (°)	RMS Noise (mJy)
28 Jan 1992	BC	7.79 × 3.96	-26.1	3.20×10^{-2}
16 Jul 1992	D	52.48 × 13.58	38.1	4.98×10^{-2}
10 Sep 1992	D	29.28 × 15.16	15.7	2.59×10^{-2}
3 Nov 1992	A	0.97 × 0.49	20.4	3.22×10^{-2}
16 Jan 1993	A	1.93 × 1.65	18.1	3.58×10^{-2}
27 Feb 1993	B	3.44 × 1.45	-26.0	3.05×10^{-2}
28 Feb 1993	B	2.86 × 1.50	-1.0	3.19×10^{-2}
19 Mar 1993	B	3.15 × 1.59	19.2	2.57×10^{-2}
30 Mar 1993	B	3.16 × 1.61	-20.0	2.51×10^{-2}
3 Oct 1993	CD	27.62 × 10.32	-26.9	2.29×10^{-2}
7,13,17 Feb 1994	D	37.19 × 13.96	-32.8	5.73×10^{-2}
19 Jun 1995	AD	1.41 × 0.84	40.1	4.32×10^{-2}
5,7 Sep 1995	AB	2.38 × 1.62	33.3	6.03×10^{-2}
26 Jan 1996	BC	4.56 × 4.31	74.5	2.46×10^{-2}
10 Apr 1997	B	2.71 × 1.65	3.3	2.37×10^{-2}
3 Aug 1997	C	19.96 × 4.69	37.8	3.50×10^{-2}

Table 4.6: Other Sources in Radio Field

Position (B1950)			
Right Ascension	Declination	location in Field	Typical Integrated Flux Density (mJy)[a]
$17^h57^m57.84^s$	−25°42′40.75″	NW	1.0–1.2
$17^h58^m09.10^s$	−25°41′30.70″	N	0.2–0.5
$17^h57^m53.24^s$	−25°44′39.6″	W	very weak
$17^h58^m16.87^s$	−25°45′28.3″	E	very weak

[a] Uncorrected for primary beam response

Chapter 5

Results

5.1 The Phenomenology of Black Holes

A TYPICAL BLACK-HOLE CANDIDATE (e.g. Cyg X-1, LMC X-3, Nova Muscae) mainly resides in one of two spectral states usually called "high" and "low" in reference to the level of soft x-ray flux. In each of these states one of two components (soft, hard) dominates the luminosity. In the high state, the *ultrasoft* component, with a Planck distribution, dominates the spectrum, accompanied by a high-energy ($\gtrsim$ 10 keV) tail with (break-less) spectral index between 2.5 and 3.5. In the low state, the ultrasoft component subsides and the high-energy tail becomes harder ($1.5 < \alpha < 2.0$) so that the entire spectrum comes to obey a single power-law with a break above 50–200 keV to a softer index (Tanaka & Lewin, 1995; Zhang *et al.*, 1997b).

Many black-hole candidates, such as Nova Muscae and GX 339–4, display a very high state, in which both the soft and hard x-ray components are high. Another common state is the intermediate state, which is transitional between the low and high states, as seen in GX 339–4 and GS 1124–68 and perhaps Cyg X-1 (Méndez & van der Klis, 1997; Belloni *et al.*, 1997, 1996), and has spectral and timing properties similar to the very high state (Belloni *et al.*, 1999). The last paper outlines the timing signatures of the various states, which we will omit here for reasons of space.

The light curves of Nova Muscae 1991 and other transients such as A0620–00, GS 2000+25, and GS 2023+33 (Ebisawa *et al.*, 1994, figure 1) have similar decay time of $\sim$ 30 days. Since it is believed temporary enhancements of accretion rate cause the outbursts of x-ray novae, it is natural to assume that the monotonic decay of the x-ray light curves reflects a gradual decrease in accretion rate $\dot{m}$ (Grebenev *et al.*, 1997). This simple observation allows us to order the spectral states by mass accretion rate, from high to low: very high, high, intermediate, low, quiescent. (The names are fortuitously intuitive.) This is the prescription adopted by the ADAF model, which we will discuss below (§6.3).

Zhang *et al.* (1997b) divides black hole binaries (BHBs) into three categories based on their light curves. Type I, or nova-like, are BHBs that have fast (~days) rise time

and slow (~tens of days) exponential decay. This category has the largest membership and includes A0620–00, GS2000+25, GS1124-68, V404 Cyg (GS2023+23), H1705-250, GROJ0422+32, GROJ1719–24 (GRS1716–249), and GRS1739–278. Type II are transients with multiple outbursts, for example GRS1915+105, GROJ1755-40, and GX339-4. Superluminal jets has been observed in all of these but GX339-4. Finally, type III BHBs have persistent high energy light curves. Examples are Cyg X-1, LMC X-1, and LMC X-3.

For his part, Liang (1998) divides Galactic black-holes into two categories: persistent, such as Cyg X-1 (Zhang *et al.*'s type III); and transient, such as A0620-00 (Zhang *et al.*'s type I). However, he acknowledges that the separation between the categories is not clear and cites GRS1915+105 (Zhang et al.'s type II) as an example of a BHB that straddles his categories. The categories of Liang (1998) essentially agree with those of Zhang *et al.* (1997b), but provide fewer distinctions, so we prefer the latter.

Like the type III BHB's, the emission of GRS 1758–258 is persistent, but like the type II BHBs, it has radio jets, albeit weak.

5.2 Black-body temperatures

Mereghetti *et al.* (1994) claimed to find a soft x-ray excess in 1993 data of GRS 1758–258. Lin *et al.* (2000b) found that a fit to 1997 multi-instrument observation with a power-law with exponential cutoff (PLE) was just as good without the black-body ($\chi^2_\nu = 1.0, \nu = 620$) as with ($\chi^2_\nu = 0.92, \nu = 619$). Mereghetti *et al.* (1997) found that the fits to the *ASCA* data did not require a black-body component as the model of a lone power-law gave an acceptable ($\chi^2_\nu = 1.031, \nu = 872$) fit.

Unlike the 1994 paper, but in agreement with the latter two papers, we find that a black-body component is redundant in the *ROSAT* data and in the observations of other soft x-ray missions.

As we mentioned in §4.3, the typically observed column density for GRS 1758–258 of $\sim 1.5\times10^{22}$ cm^{-2} (Mereghetti *et al.*, 1997; Heindl & Smith, 1998; Lin *et al.*, 2000b) lies far outside the three-sigma contour for our black-body fit to the 1993 *ROSAT*/PSPC data, shown in figure 4.5. Our best-fit column with this model ($N_H = (0.98 \pm 0.08)\times10^{22}$ cm^{-2}) is inconsistent with the usual column at the four- or five-sigma level. Additionally the power-law model provides a good fit consistent with the standard column ($\chi^2_\nu \approx 0.97$, see figure 4.5).

Table 5.1: Black-body temperatures

date	BB temp. (keV)	BB norm (10^{-4})	model[a]	χ^2_ν	χ^2_ν w/o BB	instrument
Sep 1985	0.2370 ± 0.6229	6.0	PL	1.095 (32)	1.037 (34)	*Exosat*/ME ($\alpha = 1.70 \pm 0.10$)
Sep 1985	1.063 ± 0.1112	9.8	PL	1.048 (32)	1.037 (34)	*Exosat*/ME ($\alpha = 1.32 \pm 0.41$)
Sep 1985	0.2603 ± 0.09307	17	CompST	0.993 (57)	0.985 (38)	*Exosat*/ME
Mar 1993	0.5734 ± 0.4028	10	PL	0.998 (13)	0.879 (15)	*ROSAT*/PSPC
Mar 1993	0.6488 ± 1.034	7.9	CompST	1.091 (12)	0.947 (14)	*ROSAT*/PSPC
Mar 1995	0.5374 ± 0.0265	7.1	PL	0.971 (280)	1.051 (282)	*ASCA*/SIS
Mar 1995	0.5292 ± 0.03627	5.8	CompST	0.974 (279)	1.029 (281)	*ASCA*/SIS
Apr 1997	0.8710 ± 0.1429	3.0	PL	1.321 (78)	1.335 (80)	*BeppoSAX*/LECS
Apr 1997	0.8744 ± 0.1281	3.1	CompST	1.341 (77)	1.357 (79)	*BeppoSAX*/LECS

[a] In addition to BB model. "CompST" abbreviates the Sunyaev-Titarchuk Comptonization model, as implemented in XSPEC.

We also fit the data of other soft x-ray missions over twelve years. The spectra from all of these observations are very similar to the ASCA spectrum in figure 3 of Mereghetti *et al.* (1997). Table 5.1 shows χ^2_ν's that result with and without a black-body component added to the powerlaw fit. The respective results are comparable, indicating that the ultrasoft component is redundant. As discussed above, the black-body component is characteristic of the high state, so the lack of it seems to indicate that none of these observations occurred in that state.

Mereghetti *et al.* (1997) estimated that to hide an ultrasoft component behind a hot corona requires a relatively large scattering opacity $\tau \sim 2 - 5$.

As expected, the black-body temperatures fall in the range $0.2 \sim 1.0$ keV. For comparison, the black-body plus power-law fit to the 1995 *ASCA* data in Mereghetti *et al.* (1997) found a black-body temperature around 0.4–0.5 keV. The best-fit HT model of Lin *et al.* (2000b) to the 1997 August *XTE* data gave a black-body temper-

ature $T_{BB} \approx 1.18$ keV.

5.3 High- and Low-energy Fluxes & Flux-Flux Diagram

Whereas an anti-correlation between the hard and soft x-ray fluxes is the usual sign of the transition between a low (hard) state and a high (soft) state, the correlation of the the *ROSAT* data with the *GRANAT* data through the 1991–1992 dip indicates that such a transition did not take place.

Figure 5.1 illustrates the correlations, or lack of, between the hard x-ray (20–200 keV) luminosity and the soft x-ray (1–20 keV) in the manner of Barret, McClintock, & Grindlay (1996, hereafter BMG).

The *RXTE*/ASM data does not show any significant correlation, positive or negative, to the hard x-ray dip in 1999. Except for the two-month spike at the end of 1998 and beginning of 1999, the ASM data is flat as shown in figure 4.1, and in the individual bands. There is no sign of the oscillation from late February to September 1999 noted by Smith *et al.* (1999, IAUC 7266). It is difficult to tell if the flatness is meaningful, or the result of inclusion of the Galactic diffuse emission or other discrete sources in the ASM's large field of view. It might be possible to subtract the diffuse

Figure 5.1: Barret, McClintock, and Grindlay-Style flux-flux diagram for GRS 1758–258 at an assumed distance of 8.5 kpc. The open plotting symbols represent points whose soft and hard coordinates are only approximately co-eval. The ADAF model is scaled to $M_1 = 10.6\ M_\odot$ and is discussed in section 6.3.

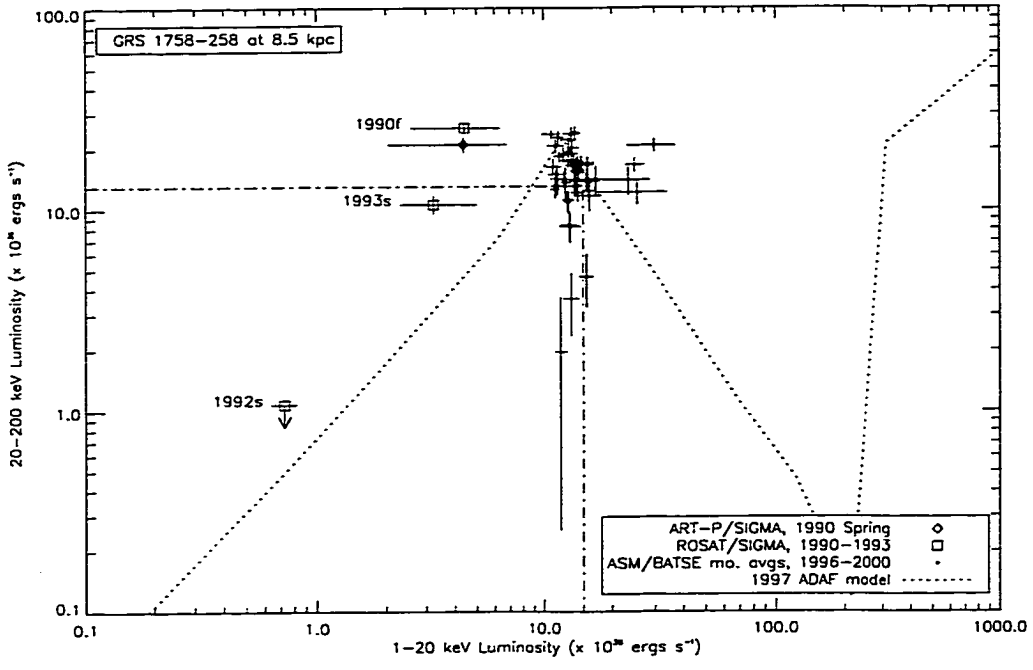

emission, but unfortunately, the sky coordinates and position angle of each pointing are not readily available.

5.4 Spectral Intensity and Shape

Many black-hole candidates (e.g. Cyg X-1) display spectral pivoting, so that the flux in a narrow energy band ($\sim$ 10 keV) remains relatively constant in time, while the

fluxes at higher and lower energies anti-correlate. This phenomenon occurs between the high and low states, in what is known as the intermediate state. A consequence of spectral pivoting is that while the bolometric luminosity remains relatively constant (Zhang *et al.*, 1997a), a correlation is established between the flux and power-law index in any given band above or below the pivot.

The error bars on the ASM power-law indices are larger than the fluctuations in their values, and the ASM 1.5–12 keV fluxes are largely compatible with a constant flux, so it is no surprise that it not possible to see any correlation between the two.

The *GRANAT* photon indices are consistent with a constant spectral slope because of the large error bars. We see a suggestion of a correlation between BATSE fluxes and spectral indices in figure 4.1. For example the flux dip of 1991–1992, has a higher index and therefore a softer spectrum.

We wanted to test for a correlation between the photon index and the flux, but calculation of flux assumes an index. Such a method can bias the results or exaggerate any correlation between intensity and shape.

Hardness ratio and count rate are next-door neighbors to photon index and flux, and are independent of one another. It is difficult to compare raw count rates across

Figure 5.2: Hardness ratio *vs.* total count rate for 1990-2000 BATSE data. The crosses are averages binned with boundaries at (A) 500 & 1000, (B) 1000 & 1700, (C) 1700 & 2600 (D) 2600 & 3400, (E) 3400 & 3700 days from 1 Jan 1990.

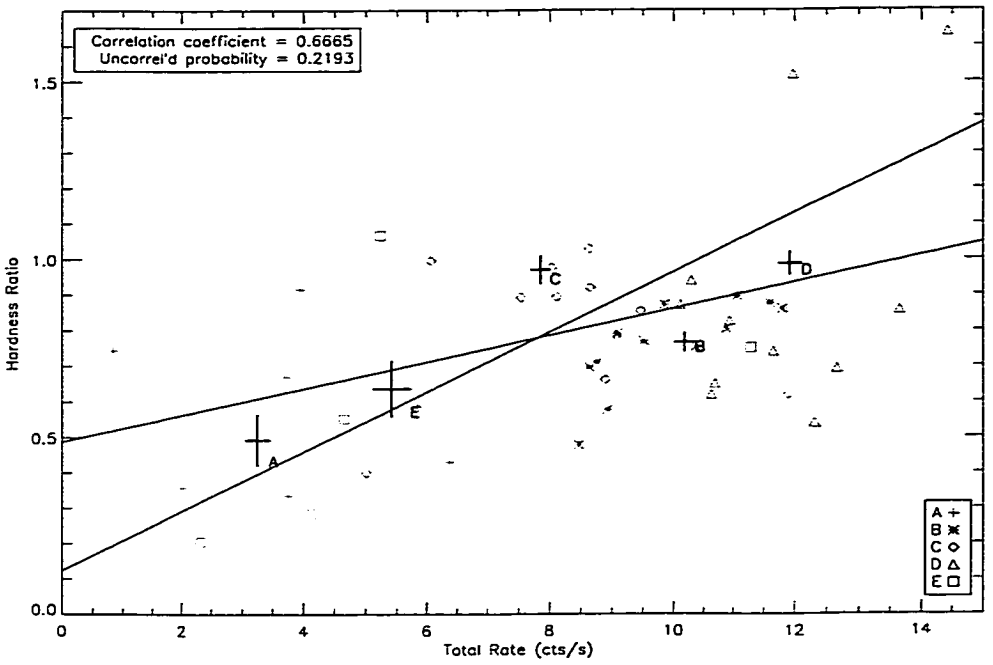

instruments, so we restrict our analysis to BATSE data, which has the longest temporal baseline.

We plot the hardness ratio (ratio of counts above and below 78 keV) against the total BATSE count rate in figure 5.2. The boundary between high and low counts is chosen to give a hardness ratio ~ 1 on average. The thick crosses represent averages over five periods that have similar total count rate throughout. From the slopes of linear fits to the averaged data, we find a linear-correlation coefficient $r = 0.67$ (cf.

Bevington & Robinson, 1992, pp. 198–200, §11.2). The probability of an uncorrelated parent distribution having a coefficient that big or bigger is only $\sim 22\%$, so there is a weak correlation between shape and intensity. Consequently we expect lower fluxes to have higher, softer photon indices, a conclusion that agrees with the predictions of the ADAF theory, discussed below (§6.3).

We considered the possibility that the drift of the source in the field of view as the space-craft is re-oriented over time could bias the correlation. We lack in-depth knowledge of the BATSE response matrices, but the close tracking of the count-rate with the unfolded flux alleviates these concerns.

5.5 Timing Analysis

Lin *et al.* (2000a) performed a power density spectral analysis of XTE data over 2.2–40.2 keV for Cyg X-1, GX 339–4, GRS 1758–258, and 1E 1740.7–2942. They found a general anti-correlation between integrated RMS amplitude and x-ray flux intensity and energy dependences in the aperiodic variability. This anti-correlation varied from source to source. They also found the shape of the power-density spectrum (PDS) to be energy-independent for all but Cyg X-1, and flat below a break frequency— ~ 0.2 Hz for GRS 1758–258.

We decided to analyze the *ROSAT* data similarly in order to compare XTE energy dependence results to those in the lower *ROSAT* energy band. The additional 5 March 1992 off-axis PSPC observation allows us to test through the putative high-low transition for any flux-dependence in the amplitude or shape of the PDS. Unfortunately the PSPC data lack statistics for analysis in sub-bands.

Figure 5.3: Power spectra for 1992 and 1993 *ROSAT*/PSPC observations. White noise has been subtracted. For comparison, the PDS from Lin *et al.* (2000a) for the 1997 August *RXTE*/PCA observation is underplotted.

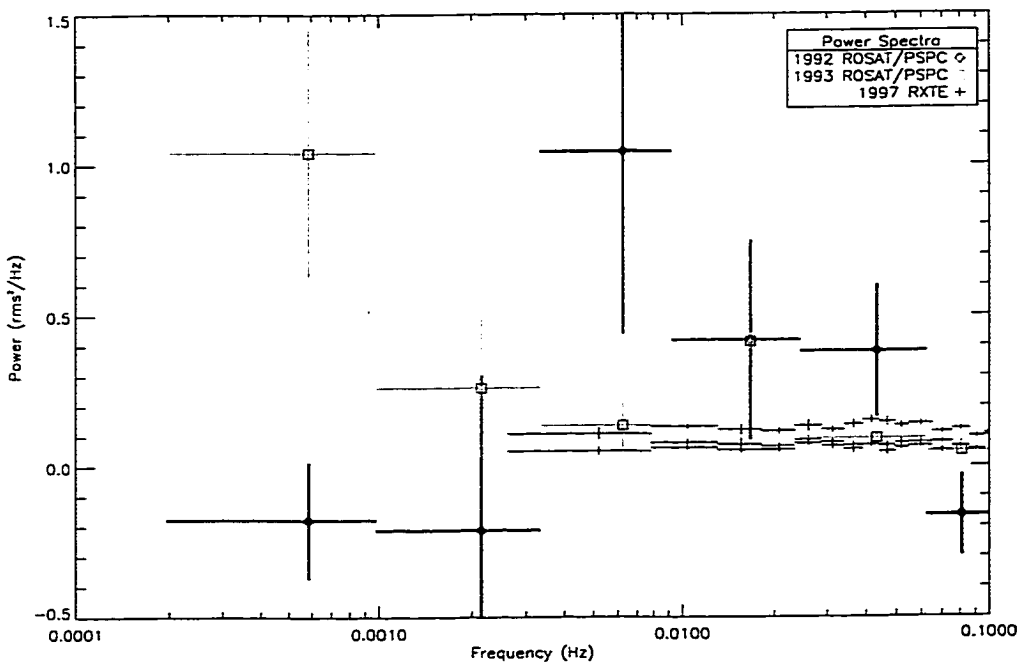

Figure 5.3 shows the result of our timing analysis of the full 1992 and 1993 PSPC data sets using `powerspec` in the FTOOLS package. White noise has been subtracted.

The uncertainties in the data are large, and the figure shows the power spectra of the two observations are consistent with the XTE results—namely that the variability is constant in energy and flux level, and that has a flat distribution below the break.

In summary, the power spectrum in March 1993 has 0.136 ± 0.0979 rms^2/Hz at 6.25 ± 2.92 mHz; that for March 1992 has 1.044 ± 0.608 rms^2/Hz at 6.25 ± 2.92 mHz; the results agree within two sigma with each other, and with that at higher energies found in Lin *et al.* (2000a). The *ROSAT* data is compatible with no flux- and no energy-dependence in the power spectrum at low energies, as predicted by shot models (Lin *et al.*, 2000a). Admittedly these are weak statements because the *ROSAT* error bars are so large.

5.6 Radio and X-ray

Radio and hard x-ray emission have been seen to correlate with each other and anti-correlate with soft x-rays in Cyg X-1 (Tananbaum *et al.*, 1972; Braes & Miley, 1976; Zhang *et al.*, 1997a), GX 339-4 (Fender *et al.*, 1999; Corbel *et al.*, 2000), GRS 1915+105 and GRO J1655-40 (Hannikainen *et al.*, 1998). Correlation of the radio and hard x-ray has also been seen in Cyg X-3 (McCollough *et al.*, 1999). Ejection of radio-emitting plasma from GRS 1915+105 correlates with dips in hard x-ray

emission (Harmon *et al.*, 1997), and similar coincidence has been seen in GRO J1655-40 (Zhang *et al.*, 1997b). Corbel *et al.* (2000) established the x-ray/radio correlation in GX 339-4 and found a possible link to jet emission. There is no clear theoretical link between the x-rays and radio, but Zhang *et al.* (1997b) propose that some of the Comptonizing electrons are scattered at high energies from the inner regions of the disk and produce incoherent synchrotron radiation.

Figure 5.4: Radio/hard X-ray flux-flux diagram. The upper limits for the old-reduction points are 4σ, while those for the present reduction are 1σ.

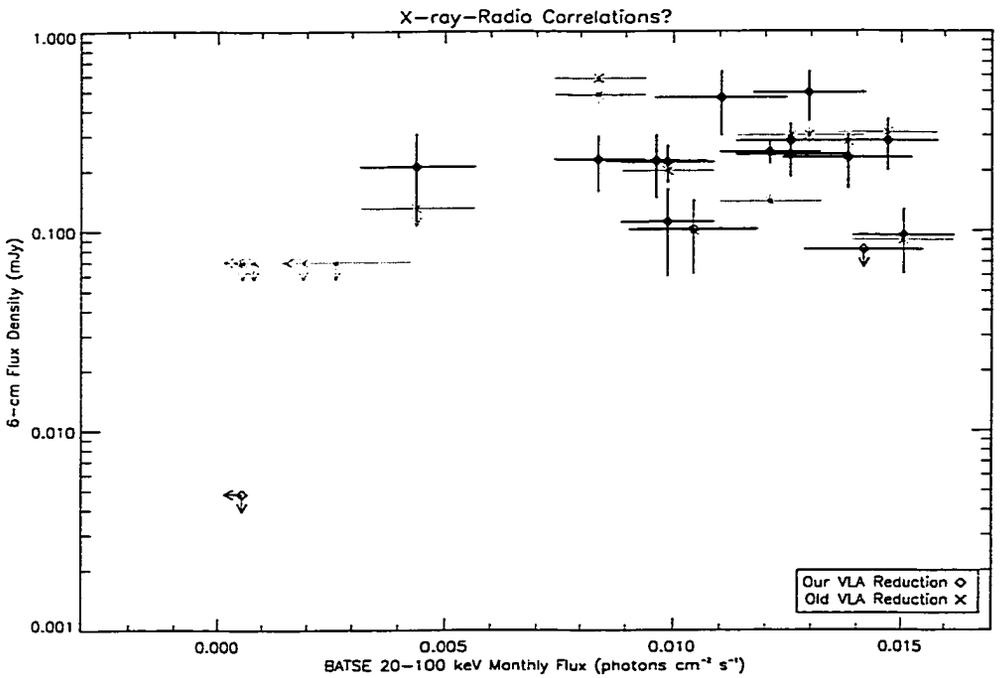

Figure 5.4 plots the radio flux density against the BATSE hard x-ray average for the same month. If we ignore the early non-detection of the source, we find in the

data that we re-analyzed no apparent correlation with the x-ray data. It is hard to say anything definitive as the observations are sparse and the weakness of the source constrains the detections to the two- or three-sigma level. We find no new radio-x-ray correlation to support VLA-C as the radio counterpart of GRS 1758–258.

Martí (1993) fit his own spherical plasmon model to a re-reduction of the same GRS 1758–258 data through early 1993 with apparently good results, but no quoted χ^2. (The same work also fits the same shark-finned-profile model to data from LSI+60°303, SS 433, and Cyg X-3.)

We noticed in the original reduction light curve a burst-like pattern in late 1992 just after emergence from the x-ray dip. The synchrotron bubble model (Hjellming & Han, 1995), which has fit events from transients A0620–00, Cen X–4, GS2000+35, Aql X–1, V404 Cyg, and Nova Muscae, has too many parameters to fit meaningfully the ~three data points in this putative event. The profile bears a passing resemblance to the May blip following initial March 1971 turn-on of Cyg X-1 (Hjellming, 1973) and the time scales are similar (~ 60 days), but the 1971 event follows an initial above-baseline turn-on and the maximal flux densities are quite different (0.02535 Jy *vs.* 0.58 mJy). The difference in distance ((1.9 kpc/8.5 kpc)^2) accounts for all but a factor of two in the latter, which could be a product of the sparseness of GRS 1758–

Figure 5.5: Putative bursts in radio data for Cyg X-1 (Hjellming, 1973) and GRS 1758–258 (table 4.3).

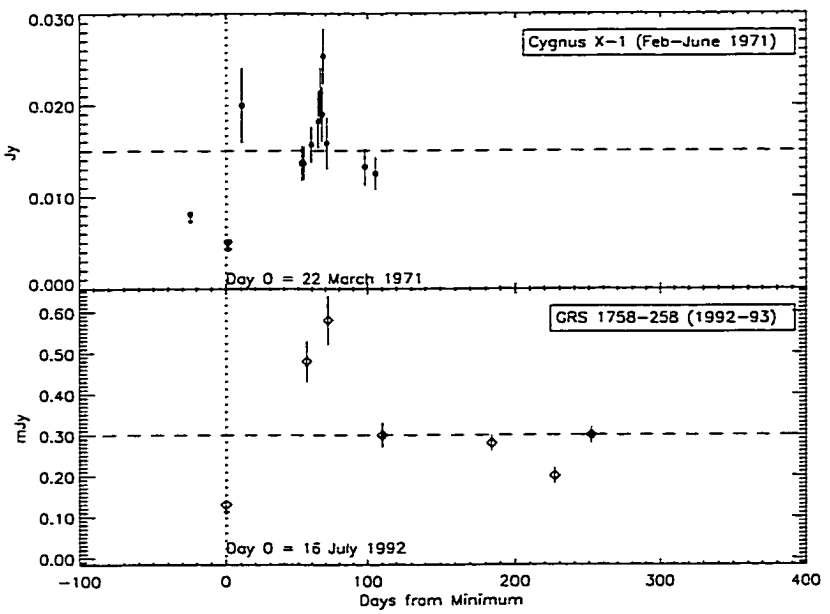

258 observations. With so few data points, it is difficult not to read one's hopes into the data. In any event, no burst is visible in flux values from the *present* re-analysis because of the large error bars.

Sadly the GRS 1758–258 observing program at the VLA was not sustained through the 1999 x-ray dip. The one observation in 1999 was too short to do anything but set an insignificant upper limit of 0.5 mJy (Hjellming, 2000), and no observations were conducted in 2000.

Chapter 6

Discussion

HERE we describe three models to account for the observed emission from GRS 1758–258. In all of these models, the soft x-ray emission comes from the disk and the hard x-ray emission comes from the corona or hot-electron cloud. The first two are standard Keplerian accretion models. The last is the advection dominated accretion flow model, which we apply in a novel way.

In all of these models, we explain the correlation between the hard and soft x-rays as a consequence of the Comptonization of soft x-rays into hard x-rays by the corona. The accurate determination of the *ROSAT* fluxes is critical here, as we extrapolate the soft x-rays from that data.

In our discussions of the first two models, we assume the argument of Shapiro

Figure 6.1: Schematic cross-sectional diagrams of the corona models described in §§6.1,6.2: (a) Two-temperature model and (b) the Disk corona model.

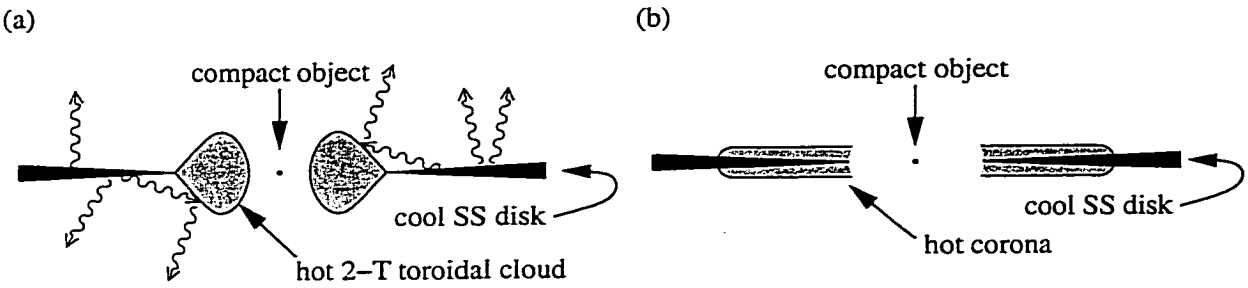

et al. (1976) that the seed photons range in energy from 0.05 keV to 5 keV. (The exact mechanism of emission is not important, but possibilities include black-body emission from the disk and synchrotron radiation from disk electrons, as explained in Shapiro *et al.* (1976); Zhang *et al.* (1997).)

6.1 Comptonizing Donut Model

We apply the data to the two-temperature model of Shapiro, Lightman, & Eardley (1976, hereafter SLE). As depicted in figure 6.1a, the inner part of the Shakura-Sunyaev (SS) disk expands to form a hot, donut-shaped, optically thin, two-temperature cloud. (The drawback of this model is that the disk is thermally unstable, Liang, 1998, .) The disk emits soft x-rays with luminosity L_{soft}. We will use the *ROSAT* and *GRANAT* data to derive the fraction of the soft photons ζ that must be upscattered

by the optically thin cloud to produce the observed hard photons.

Some of the disk's soft emission passes through the cloud unabsorbed ($L_{soft,obs}$) or does not even intersect it, while some (L_{seed}) is Compton scattered:

$$L_{soft} = L_{soft,obs} + L_{seed} = (1-\zeta)L_{soft} + \zeta L_{soft}.$$

where ζ is the scattering fraction, which depends on the optical depth and geometry. The scattered luminosity $L_{seed} = \zeta L_{soft}$ is Comptonized with gain $A(y, E_{seed}) = L_{hard}/L_{seed} = L/\zeta L_{soft}$, where $y = \frac{kT}{m_e c^2}\max(\tau, \tau^2)$ is the usual Compton y-parameter, E_{seed} is the energy of the seed photons, and L_{hard} is the total scattered luminosity.

SLE have numerically integrated the steady-state Kompaneets equation to produce curves of the gain factor $A(y)$ for various seed-photon energies.

Now

$$p = \alpha - 1 = -\frac{3}{2} + \sqrt{\frac{9}{4} + \frac{4}{y(1+f)}}$$

where $f \approx 2.5\frac{kT}{m_e c^2}$ is a relativistic correction to the (non-relativistic) Kompaneets equation, and y is as above (SLE, eqn. 16).

We then find that the ratio of the scattered and unscattered photons, $\Gamma = \frac{\zeta}{1-\zeta}$, can be derived from quantities that are either observable or the result of numerical

integration:

$$\Gamma = \frac{L_{hard}}{AL_{soft,obs}}$$

which allows us to evaluate easily the fraction of scattered soft photons:

$$\zeta = \frac{\Gamma}{1+\Gamma} = \left(1 + \frac{AL_{soft,obs}}{L_{hard}}\right)^{-1}.$$

The best fits to the spring 1993 observations data from *ROSAT* and *GRANAT* give $\alpha_{soft} = 2.2 \pm 0.2$, and $\alpha_{hard} \approx 1.5 \pm 0.2$. We use these indices to extrapolate the hard and soft fluxes measured by these missions to the required energy bands: $F_{hard}(5 - 150 \text{ keV}) = (1.30 \pm 0.19) \times 10^{-9}$ ergs cm^{-2} s^{-1} and $F_{soft,obs}(0.05 - 5 \text{ keV}) = (3.4 \pm 1.6) \times 10^{-10}$ ergs cm^{-2} s^{-1}. So $L_{soft,obs}/L_{hard} = 0.26 \pm 0.13$.

We estimate the gain factor from the curves in figure 1 of SLE, once we derive y from the power-law index and SLE's equation 16. Combining the model's assumed cloud temperature with $\alpha_{hard} = 1.5 \pm 0.2$, we obtain $\tau = 2.0$ and $y = 1.5$. So, $A \approx 15 \pm 5$ and the scattering fraction $\zeta \approx (20 \pm 12)\%$. So less than a third of the soft x-rays need be upscattered by a Comptonizing cloud that pushes the bounds of optical thinness to give the hard x-ray ($\gtrsim 5$ keV) spectrum in spring 1993. This result is consistent with the $\sim$ 10% SLE found by applying their model to Cyg X-1. Our simple analytic results agree with the broad conclusions of others concerning general model parameters.

Other observational results appear to be in agreement with our derived optical depth and assumed temperature. Kuznetsov *et al.* (1999) fit the 1990–1997 *GRANAT* data to a Comptonized disk model and found $\tau \approx 1.2$ and $T \approx 41$ keV. On the other hand the best-fit HT (Titarchuk, 1994; Hua & Titarchuk, 1995) plus black-body model of Lin *et al.* (2000b) to the 1997 August *XTE* data gave $\tau \approx 3.4$ with an electron (cloud) temperature $T \approx 52$ keV.

6.2 Partial Disk Corona

We now consider the disk corona model discussed in Liang (1998) and depicted in our figure 6.1b. In this model the corona is adjacent to the disk and sandwiches it from above and below like an undersized hamburger bun. The model was first proposed by Liang & Price (1977) and Bisnovatyi-Kogan & Blinnikov (1977) as an alternative to the two-temperature model that would stabilize the disk. It originally specified a corona that completely covered the disk, but this requirement was dropped in light of observed non-correlations between soft and hard x-rays, and lack of the predicted "Compton-reflection hump" at tens of keV (Liang, 1998). Additionally the lag of the hard x-rays behind the soft found by Miyamoto *et al.* (1993) in Nova Muscae and GX 339–4 in the very-high state support the physical separation of the hard and soft emitting regions.

As with the previous model, the disk emits soft x-rays L_{soft} which are then Compton up-scattered to produce the hard x-rays L_{hard}. The corona covers some fraction, ξ, of the disk, so $(1-\xi)$ of the original photons have no chance of interacting with it. If the corona's optical depth is τ, another $\xi e^{-\tau}$ of the original photons pass through the corona unaffected. So the surviving photons that do not interact with the corona have observed luminosity

$$L_{soft,obs} = L_{soft}(1-\xi) + L_{soft}\xi e^{-\tau} = L_{soft}(1-\xi+\xi e^{-\tau}).$$

The seed-photons have luminosity $L_{seed} = \xi L_{soft}(1-e^{-\tau})$ before upscattering. From this point, it is easily to see that the formalism for deriving the covering fraction in terms of observables is identical to that of the previous model, with $\zeta = \xi(1-e^{-\tau})$. The covering fraction is then

$$\xi = \frac{1}{1-e^{-\tau}}\left(1+\frac{AL_{soft,obs}}{L_{hard}}\right)^{-1}.$$

The extrapolated luminosity ratio (150 : 5.0 : 0.05 keV) from the spring 1993 *ROSAT* and *GRANAT* data remains $L_{soft,obs}/L_{hard} = 0.26\pm0.13$. From the *GRANAT* spring 1993 Comptonized disk model temperature of ≈ 85 keV and $\alpha_{hard} = 1.5\pm0.2$, we find $y \approx 1.6$ and $\tau \approx 2.4$. For this y, we get the same amplification factor as for the previous model, $A \approx 15 \pm 5$, so the covering fraction $\xi \approx \zeta/(1-\exp(-\tau)) = 9$–$35\%$.

So less than about a third of the emitting region of the disk is covered by a corona in spring 1993. Several measurements using different techniques obtained comparable results. Lin *et al.* (2000a), which found that the lack of PDS steepening with increasing photon energy eliminated the $\zeta \sim 1$ model investigated by Böttcher & Liang (1998). Maccarone & Coppi (2001) found a $\sim 25\%$ reprocessing fraction by interpreting the soft x-ray lags in XTE J 1748–2848 with a radiative feedback model.

6.3 Advection-Dominated Accretion Flow

We now take up the advection-dominated accretion flow (ADAF) model. This is the most mature model of black-hole accretion, in that its proponents have published spectral predictions (Esin *et al.*, 1997, 1998). Thus we decided to seize the opportunity to test the model in detail for GRS 1758–258, and to scout out the theory-testing terrain that upcoming observational developments will open to detailed exploration.

Ichimaru (1977) was the first to notice the importance of advection-dominated accretion in understanding BHBs, but his paper was lost in the shuffle of history. The current ADAF model is a generalization by Honma *et al.* (1991), Abramowicz *et al.* (1995), Narayan & Yi (1994), and Narayan & Yi (1995) of the SLE optically thin solution to include advection terms. The accretion flow has two zones: an inner

advection-dominated flow, and an outer thin accretion disk. The inner ADAF accretes into the black hole as a quasi-spherical two-temperature corona, while the thin disk is Keplerian (cf. figure 6.2).

The advection-dominated inflow-outflow solutions (ADIOS) of Blandford & Begelman (1999) have many of the same properties as the ADAF solutions, but much of the inflowing energy is ejected with an outflowing wind instead of being advected into the compact object. The observational consequences are unclear for black holes: the cleanest test is for neutron stars, whose surfaces would provide a clear indication of whether the inflowing matter is being accreted or ejected.

Later work by some of the ADAF authors (Narayan *et al.*, 2000; Igumenshchev *et al.*, 2000) and others (Quataert & Gruzinov, 2000; Agol, 2000) on convective accretion flows are irrelevant to our discussion here: these flows explain low viscosity parameters $\alpha \lesssim 0.05$ that give rise to quiescent-state spectra, a conceptual and physical regime far removed from the 1997 and 1998 papers.

The present model resembles the two-temperature model of Shapiro *et al.* (1976, just discussed) with the difference that the transition radius between the quasi-spherical and Keplerian zones, $r_{\rm tr}$, changes with accretion rate. The low state has low accretion rates with $r_{\rm tr} = R_{\rm tr}/R_{\rm G} \sim (10^2 - 10^4)$ (where $R_{\rm G}$ is the Schwarzschild

Figure 6.2: ADAF model states adapted from figure 1 of Esin, McClintock, & Narayan (1997) to incorporate the changing r_{tr} in the low state. The small dots represent the quasi-spherical (ADAF) flow and the thick bars represent the Keplerian disk.

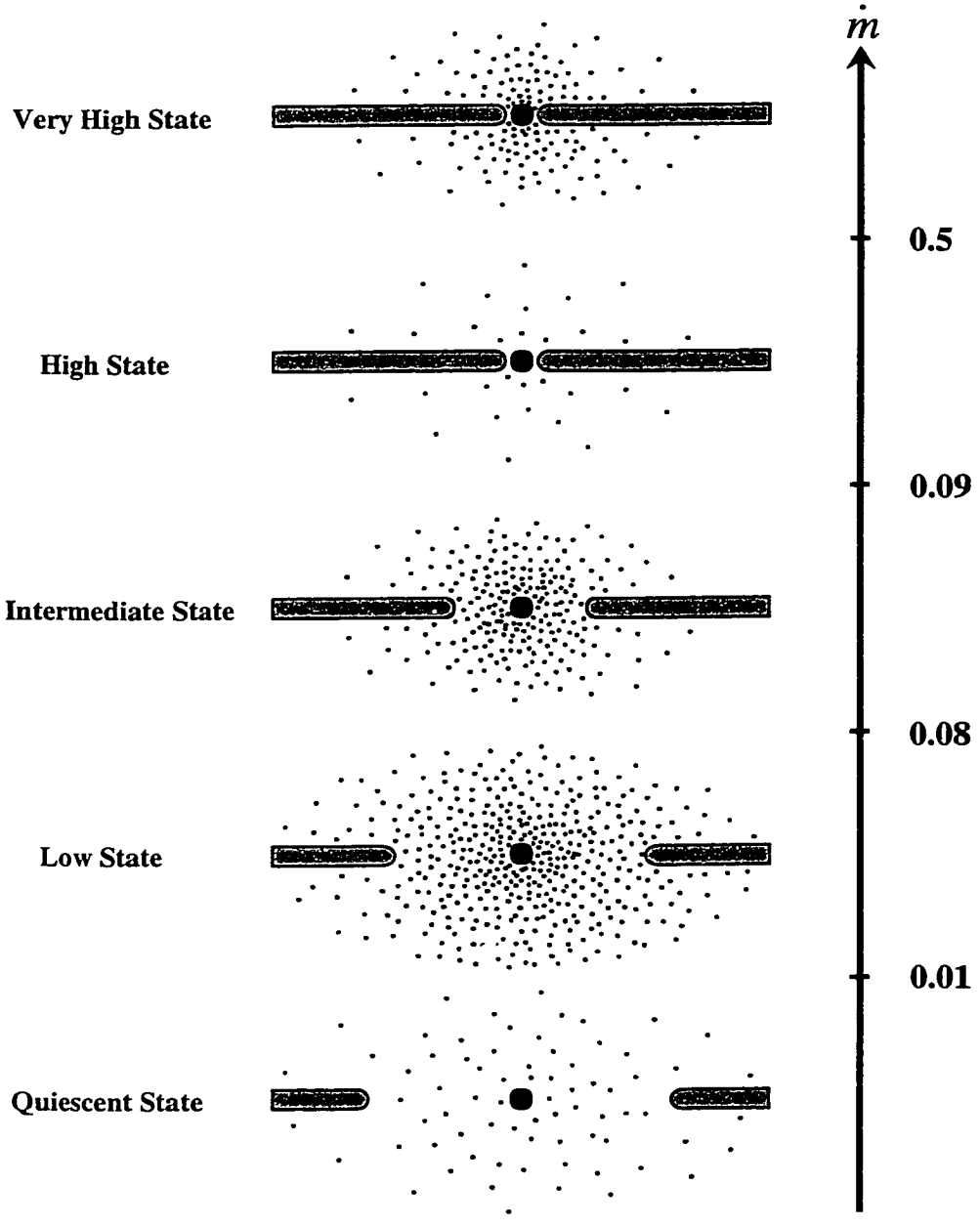

radius) and the soft and hard x-ray emission increase with increasing $\dot{m}$. Most of the energy of the corona is advected into the hole. When $\dot{m} > \dot{m}_{\rm crit}$, the flow enters an intermediate state: the transition radius shrinks and the spectrum changes from predominantly hard to soft emission. When $\dot{m}$ becomes sufficiently high, the thin disk reaches down to the last marginally stable orbit ($r_{\rm tr} \sim 3$) and the ADAF exists only above and below the disk since it cannot be inside this orbit. The flow is now in the high state. (The model has only a tentative explanation of the very high state, proposing a parameter η that controls the fraction of disk viscous energy dissipated directly in the corona.) The states are illustrated schematically in figure 6.2.

The most notable characteristic of the model is that the state of a black hole accretion is controlled by one parameter, the mass accretion rate $\dot{m} \equiv \dot{M}/\dot{M}_{\rm Edd}$, where $\dot{M}_{\rm Edd} \equiv L_{\rm Edd}/0.10c^2$. The last definition assumes a ten percent radiative conversion efficiency. (This assumption is restricted to this definition; the radiative efficiency, ϵ, of the model itself varies with $\dot{m}$.)

In other words

$$\dot{m} = \left(\frac{L}{\epsilon(\dot{m})c^2}\right)\left(\frac{0.10c^2}{L_{\rm Edd}}\right)$$

or

$$L \propto \dot{m}\epsilon(\dot{m})L_{\rm Edd}$$

Another significant feature of the ADAF theory is the scale invariance of the states: the theory is the same for black holes of any size, from Galactic to supermassive (Narayan & Yi, 1995), which means the radiative efficiency is independent of black-hole mass, that is $\epsilon \neq \epsilon(M_1)$. Since the Eddington luminosity scales with the primary's mass, the luminosity of any given state also scales with mass, thus establishing a correlation between black hole mass and luminosity at known $\dot{m}$:

$$L_{\rm Edd} \propto M_1 \Rightarrow \boxed{L = L(\dot{m}) \propto M_1}.$$

(Either the incompleteness of our reading or the humility of the theory's authors has prevented our finding a mention of this correlation in the literature.) At a given $\dot{m}$, we can compare the model luminosity $L_{\rm model}$ to measured luminosity $L_{\rm emp}$ to find M_1, the mass of the observed black hole:

$$\frac{L_{\rm emp}}{L_{\rm model}} = \frac{M_1}{M_{\rm model}}$$

We now use the mass-luminosity correlation and the observed flux extremes to constrain the mass of GRS 1758–258. Since the ADAF models scale with primary mass, the scale factor that best allows the model to fit the data fluxes is the same factor that must multiply the model's assumed mass. In theory, the model's mass scaled by the factor is then the mass of the primary. In reality, other model parameters such

as the binary's inclination angle i, viscosity α, and the fraction of the total pressure due to gas (as opposed to magnetic) pressure β also effect the luminosity, though they do not effect all energies and all states uniformly, as does the primary mass M_1. Additionally, since the model predicts *luminosities* while we measure *fluxes*, our technique only gives us the primary mass at an assumed distance d_0, so instead of M_1, we find $M_1/(d/d_0)^2$.

We take the ADAF model from the νL_ν curves of EMN for $M = 6\ M_\odot$, $i = 60°$, $\alpha = 0.25$, $\beta = 0.5$ for Nova Muscae, and of Esin *et al.* (1998, figure 1b) for $M = 9\ M_\odot, i = 40°, \alpha = 0.3, \beta = 0.5$ for Cyg X-1. The luminosities of the high-state spectra for the 1997 model are not exactly correct because the high-state curves in figure 10 of EMN do not extend out to 200 keV. To overcome this limitation, we have replaced the $\dot{m} = 0.40$ curve with its suitably renormalized counterpart from Figure 1a of Esin *et al.* (1998); the two curves agree to a constant factor for those energies in common. The remaining high-state hard luminosities are integrated from linear extrapolations, which may make them slightly high, though not by much, judging from the extrapolation of the $\dot{m} = 0.4$ curve.

The 1998 model is an incremental improvement to the 1997 model. Observational evidence from Życki *et al.* (1997) that the transition radius varies in the low state and

not exclusively in the intermediate state moved the model's authors to incorporate this feature. Other changes reflect that a different source is being modeled. Figure 4a of EMN makes it clear that $i = 30°$ instead of $i = 60°$ increases the flux $\sim 25\%$ in both soft and hard x-ray bands, at least for the low state. The change in α is more complicated, as its value effects the value of $\dot{m}_{\rm crit}$. For $\alpha = 0.25$, $\dot{m}_{\rm crit} \approx 0.082$, while for $\alpha = 0.3$, $\dot{m}_{\rm crit} \approx 0.11$ and the flux shifts to harder energies at the critical value, according to EMN's figure 4b. The 1998 theory models Cyg X-1, but the authors do not make clear how its wind-driven nature effects the model.

We want to find the minimum scaling factor for the model fluxes to produce the maximum observed hard x-ray fluxes. For consistency, we can check that the *GRANAT* and *ROSAT* minima from the 1991–1992 dip are still possible with this multiplicative factor; we can also check the coeval photon indices. Figure 6.3 plots each model integrated over hard and soft energy bands along with the observed flux extremes in those bands. The ordinate is $\mathrm{p}\dot{m} \equiv -\log \dot{m}$, so higher $\dot{m}$ is to the left. The boundaries between the high, intermediate, and low states are indicated by dotted vertical lines. The fluxes in both plotted bands are monotonic functions of $\dot{m}$ for the low and quiescent states. Note that the hard x-ray power-law indices increase with decreasing flux, in agreement with the intensity-shape correlation we saw in the BATSE data (§5.4).

Figure 6.3: Results of simple calculation of the multiplicative factor for the 1997 model. The 1990 and 1997 *GRANAT* fluxes are taken from figure 1 of Kuznetsov *et al.* (1999), and the power-law indices from their table 1. The one-sigma 1992 *GRANAT* upper-limit is calculated from data of table 2 of Gilfanov *et al.* (1993).

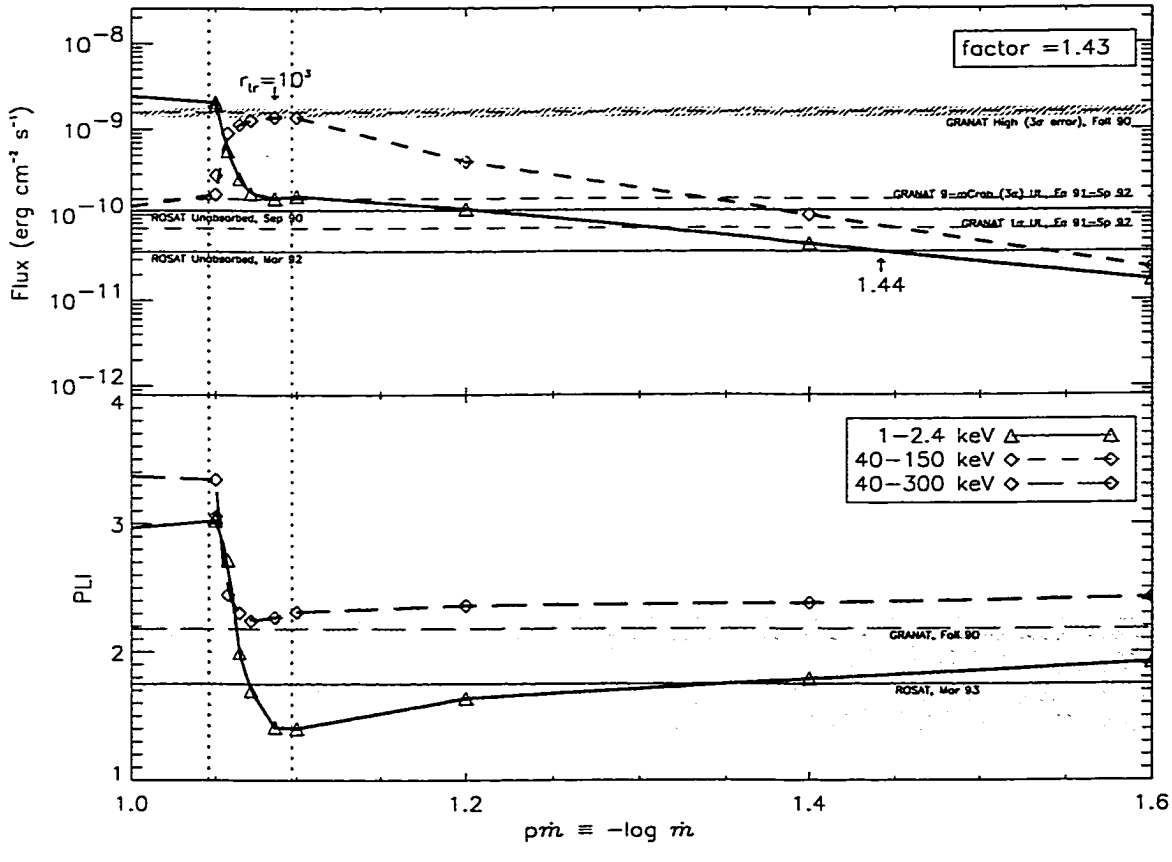

We find that the theory is consistent with the *GRANAT* and *ROSAT* observations. The scaling factor multiplying the maximum hard model flux is just enough to reproduce the maximum *GRANAT* flux in 1990 of 92.5 ± 3.8 mCrab at the three-sigma lower-limit. The factor also allows the soft model flux to match the 1992 *ROSAT* observed flux minimum at the same $p\dot{m}$ as the hard model flux falls below the coeval *GRANAT* upper limit. In the lower panel we see that the model's hard photon index just brushes against the top error-bar of the *GRANAT* 1990 index at approximately the same $p\dot{m}$ at which the 1990 *GRANAT* max occurs. At the $p\dot{m}$ of the 1992 flux minima, the model's soft photon index is well within the error bar what we assume to be the coeval *ROSAT* index. So we find that the ADAF theory can reproduce the *GRANAT* flux maximum and the *ROSAT* minimum at the same time as it predicts a hard x-ray flux that falls below the *GRANAT* upper-limit.

Furthermore, if we attribute the multiplicative factor to primary mass alone, then to agree with the *GRANAT* fall 1990 high at the three-sigma level, we must have $M_1/(d/8.5 \text{ kpc})^2 \gtrsim 8.6\ M_\odot$.

We could achieve a more sophisticated constraint on the factor by folding all of the *ROSAT* and *GRANAT* flux and photon index data into a chi-squared analysis, but the authors of the theory warn that "the uncertainties in the model are still too

large to draw meaningful quantitative conclusions" (Esin *et al.*, 1998), so such an analysis is unwarranted with the theory as it now stands.

This lower-limit is similar to the mass of Cyg X-1 which is interesting because Cyg X-1 usually remains in the low state with only occasional forays into the high. Unlike Cyg X-1, which has a massive companion and accretes via wind, the non-detection of an optical companion for GRS 1758–258 constrains its mass to $\lesssim 4\ M_{\odot}$ (Chen *et al.*, 1994), so the primary must accrete by Roche-lobe overflow. The other dynamically confirmed BHBs with identifiable secondaries also accrete by Roche-lobe overflow, but most of them have also been seen in a very high state (cf. figure 6.4, discussed in §6.4), whereas we have found GRS 1758–258 does not even cross into the high state.

6.4 Further Inquiries with the ADAF Model

We will now explore the ADAF model in the context of the flux-flux diagram of Barret, McClintock, & Grindlay (1996, BMG). We find that the ADAF model explains the boundaries of the "burster-box" and reveals a gap in the diagram's differentiation of black-holes from neutron stars.

In figure 6.4 we re-present figure 13 of Barret *et al.* (2000) overlaid with the tracks

of the ADAF models of Esin *et al.* (1997, EMN) and Esin *et al.* (1998). To make the comparison meaningful, we have scaled the luminosities of each black hole binary by 3 $M_\odot/M_1$, and the respective 1997 and 1998 models by 3 $M_\odot$/6 $M_\odot$ and 3 $M_\odot$/9 $M_\odot$. So assuming scale invariance of the ADAF model holds, we normalize the luminosities to $M_1 = 3\ M_\odot$.

With one exception, all of the black hole binaries (BHBs) are in reasonable agreement with the theory (though, since BMG's data lacks error bars, it is difficult to tell what reasonable means). The solid points show the BHBs at their highest observed hard luminosities, so it is no surprise that the plot catches them either at the corner that represents $\dot{m}_{\rm crit}$ or in the very-high state (cf. figure 6.2). The 1996 paper flags A0620-00 as having a somewhat doubtful hard x-ray tail. With that one exception, the models appear to have good agreement with the theory, including the very high state theory. No one value for fraction of disk energy dissipated directly in the corona, η, stands out as a runaway winner, but $\eta = 0.5$ is reasonably close to three BHB points, whereas the other two values of η have only one each. It is remarkable that the 1998 theory, which was constructed for Cyg X-1, predicts soft x-rays that are not only over-luminous in both low and high states, but that are both over-luminous by the same factor of ~ 1.8. A similar factor obtains for GRS 1009-45, whose mass has only recently been measured (Filippenko *et al.*, 1999).

Remarkably the 1998 theory places the transition between low and intermediate states, which is the first simultaneous maxima of soft and hard x-rays, at the corner of the burster box. Notice that the neutron-star binaries (NSBs), which have not been renormalized by mass, lie along the theory's low-state line (which runs roughly parallel to the $y = x$ line along which the luminosity points scale with Md^2). Consequently the BMG plot does not distinguish *low-state* BHBs from NSBs. Since NSBs would likely show a black-body component (Narayan *et al.*, 1997) and this component appears in BHBs only with the onset of the intermediate and high states, perhaps the presence or absence of the black-body component would distinguish NSBs from BHBs within the box. This criterion falls short if the 1997 model is the more accurate, because the model predicts that intermediate-state and some high-state black holes fall in the box. It is possible that a third axis is necessary to distinguish BHBs from NSBs uniquely, or perhaps a restriction of the energies included in the luminosities of the hard axis, since NSBs usually lack a hard tail.

BMG's figure 3 shows the plot for four observations of GX 339–4 at an assumed distance of 4.0 kpc. The points in the plot are labeled from left to right "Low state," "High state II," "High state I," "Very high state." (The nomenclature is apparently different from that of the ADAF papers.) In figure 6.5 we compare this data to the ADAF models at minimal (3 $M_\odot$) black-hole mass. We see that the high-state

Figure 6.4: Plot of Barret *et al.* (2000, cf. BMG). The neutron star luminosities are unabridged, but the black hole luminosities have all been renormalized to 3 $M_{\odot}$. Overplotted for comparison is the ADAF model of Esin *et al.* (1997) and Esin *et al.* (1998) normalized to that same mass. Small unfilled circles are based on the second distance estimate in BMG. The numbers in the polygons are the model $\dot{m}$'s at each point.

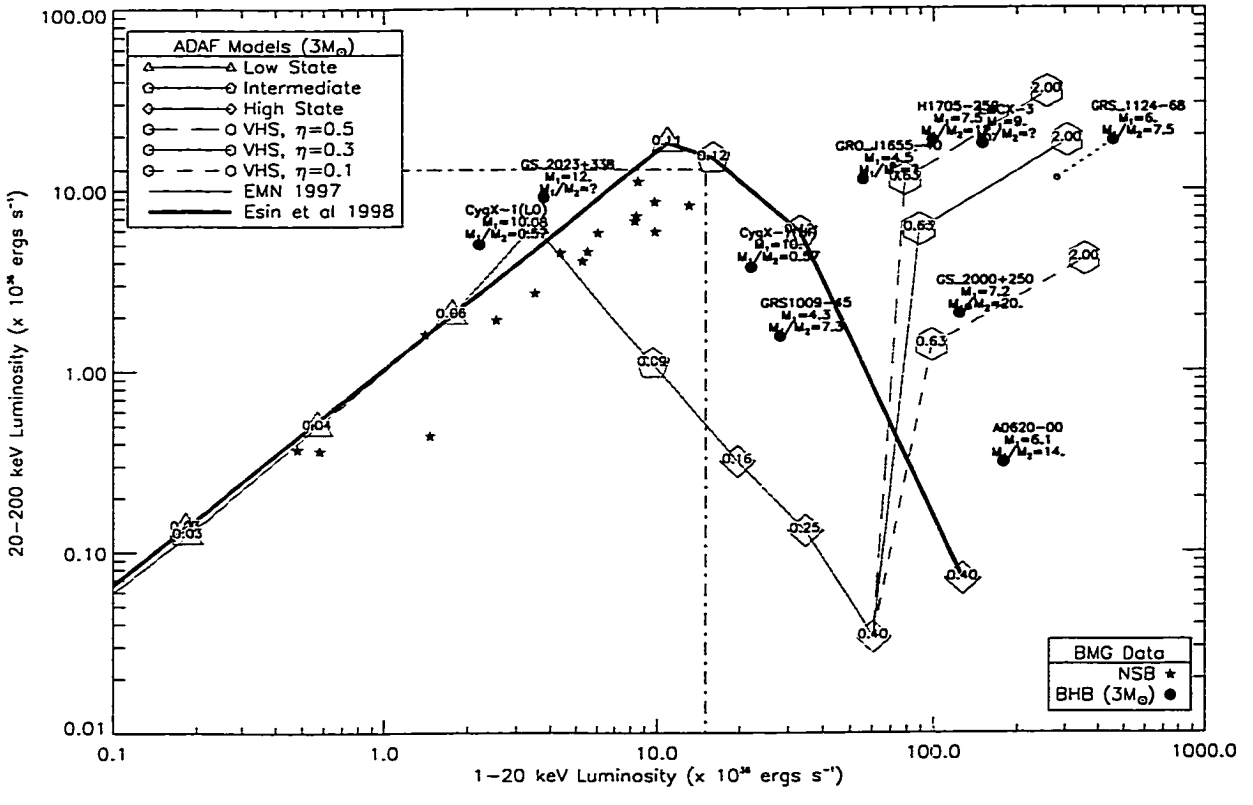

segment of the 1997 $\alpha = 0.25$ model agrees reasonably well with the data, but that the "high-I data point" (third from left) is somewhat distant from both the high and the very-high state segments. EMN caution that their very-high state is speculative. Esin *et al.* (1998) do not treat this state for Cyg X-1, so we do not know how the very-high-state theory changes with the change in parameters between the papers, but it is safe to assume that it cannot change without losing agreement with the BHB points on the BMG plot of figure 6.4. This part of the theory comes reasonably close to the data, as well as giving good agreement between the data and the 1998 $\alpha = 0.30$ model for the low and high states, on the assumption that GX 339–4 is a factor of $\sim \sqrt{3}$ more distant, in closer proximity to the Galactic center ($\sim$ 7 kpc). The typical absorption column to the source (1—9$\times 10^{21}$ cm^{-2}; Belloni *et al.*, 1999; Méndez & van der Klis, 1997) is consistent with this conclusion. Of course, any agreement with the ADAF theory presumes that the source is in fact a black hole, a premise which is not without dissent (e.g. Cowley *et al.*, 1987). The same authors estimate the 4.0 kpc distance to the source from its color and by assuming its interstellar line velocity is due to differential rotational in the Galactic plane.

BMG's figure 2 shows the plot for ten points from the burst of Nova Muscae 1991 (GRS 1124-68) after its x-ray maximum 16 January of that year. In figure 6.6 we compare this data to the ADAF models at (6 $M_\odot$) black-hole mass. Recall that the

Figure 6.5: Data from Barret, McClintock, & Grindlay (1996, BMG), figure 3. Overplotted for comparison are the ADAF models of Esin, McClintock, & Narayan (1997, EMN) and Esin *et al.* (1998) renormalized to $M_1 = 3\ M_\odot$. The state names are those of BMG and are somewhat different than in the ADAF model.

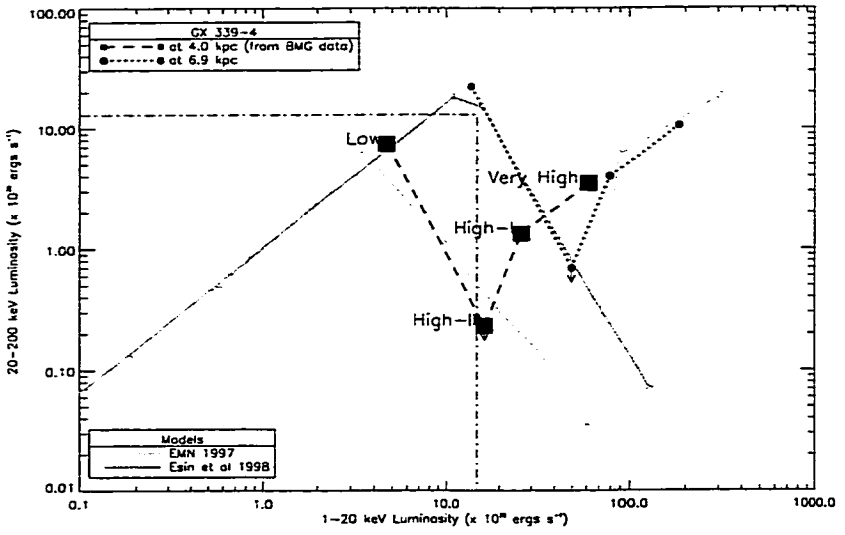

model of EMN (1997) was constructed to fit this source. It is not surprising that the EMN model fails to fit the very high state data, since the model's authors ventured only a tentative proposal for that state. What is surprising is that the high-state model is so far removed from the data, as figure 12 of EMN primed us to expect that the model was in much better agreement with this state.

Figure 6.6: Data from Barret, McClintock, & Grindlay (1996), figure 2. Underlaid for comparison are the ADAF models of Esin, McClintock, & Narayan (1997) and Esin *et al.* (1998) renormalized to the mass of Nova Muscae, 6 $M_{\odot}$. The numbers enclosed in the circles represent the day of the year 1991 for each point; the dotted line is only to guide the eye.

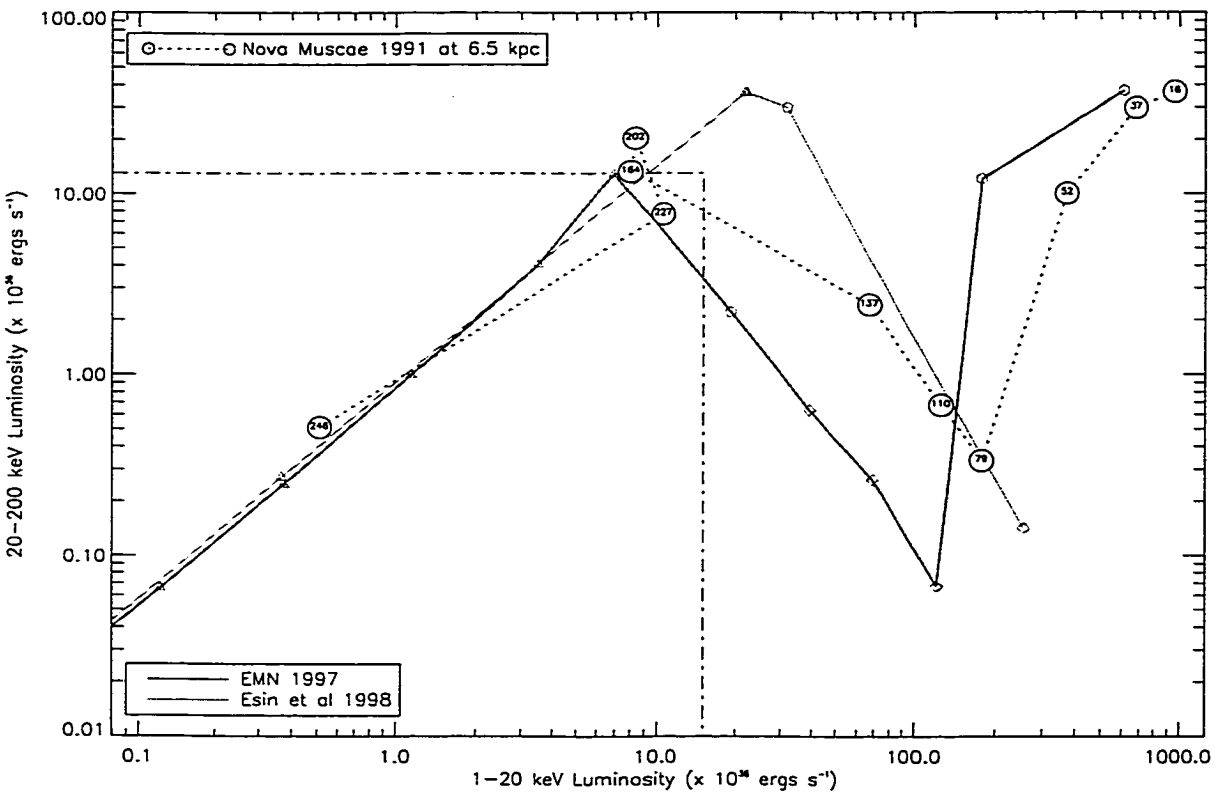

6.5 Conclusion

We have seen that the preponderance of the data indicates that GRS 1758–258 was in a low state in the early 1990's, since there was no black-body component (§5.2) and the soft and hard x-rays were correlated (§5.3). (Lack of dependable soft x-ray data prevents us from speaking about the 1999 x-ray dearth.) We found a correlation between the hard x-ray spectral intensity and shape.

We performed a power-spectral analysis on data bridging the 1991–1992 x-ray dip for *ROSAT*/PSPC, which probes lower energies than *RXTE* data (§5.5), and we found that the *ROSAT* data is compatible with no flux- and no energy-dependence in the power spectrum at low energies, but the error bars are so large it is not possible to say anything meaningful here.

We found no significant correlation between the hard x-ray and radio fluxes, other than the long-known radio turn-on when the hard x-rays were coming up out of their 1991–1992 slump (§5.6). The hard x-ray correlation with radio is seen in other BHC systems, and, again, large error bars prevent us from seeing any correlation in any but the largest flux shifts.

We applied the data to three models of accretion disk emission and used it to

constrain the geometries of the Comptonizing torus (§6.1) and the disk-corona models (§6.2). In the former, two-temperature model, less than a fifth of the soft photons are upscattered to give the observed hard emission, while the latter disk-corona model would say that less than a quarter of the disk is covered by a $\tau \approx 2$ corona, consistent with the $\sim 10\%$ found by SLE in applying their theory to Cyg X-1.

In §6.3 we found that the coeval *GRANAT* and *ROSAT* data were consistent with the ADAF theory for an accreting black hole that spends most of its time in the low state, but perhaps occasionally sidles up into the intermediate state. The correlation between the hard x-ray intensity and spectral shape observed in the BATSE data (§5.4) further supports the theory. We then introduced a new technique for constraining the mass of the primary and applied it to GRS 1758–258. With the present data we constrained the mass of the black hole primary $M_1/(d/8.5 \text{ kpc})^2 \gtrsim 8.6\ M_\odot$.

In §6.4 we critically assessed the ADAF model against the flux-flux diagram of Barret *et al.* (1996, BMG). We found that the ADAF model explains the high-luminosity corner of the "burster-box" but also raises the possibility that the box includes not only the advertised neutron stars, but also some low-luminosity black holes. Furthermore we found differences between the ADAF model and BMG's data for Nova Muscae 1991 and GX 339-4. The discrepancy for the latter appears to be overcome

by positing a distance of 6.9 kpc instead of 4.0 kpc.

For a more critical test of the ADAF theory along this same line, additional data from binaries in various states is necessary. Continuous all-sky monitoring in both the soft and hard x-ray bands, such as would be provided by EXIST (Grindlay *et al.*, 2000; Grindlay & EXIST Science Working Group, 2000), would be key to this effort, and the luminosity's mass-scaling allows us to compare directly the tracks of black holes of diverse masses.

With timing signatures for the various states established (cf. Belloni *et al.*, 1999) and sharpened, intrinsic measurements of state along with luminosity at a single point in time could in principle give us the black hole mass. Once the ADAF model is refined far enough, we may well find that it to be only the first-order mass dependence of accretion disk luminosity, and higher-order corrections will explain more subtle differences, such as the x-ray hump ($10 \sim 100$ keV) seen in the spectra of Seyfert nuclei (cf. Liang, 1998).

References for Chapter 1

Butterfield, H. 1957, *The Origins of Modern Science, 1300-1800* (Free Press)

Hafner, P. 1996, The Pope's Physicist, *Sursum Corda*, 66

Jaki, S. 1990, *Science & Creation* (University Press of America)

Longair, M. 1992, *High Energy Astrophysics* (Cambridge University Press)

Meadows, A. 1984, The Origins of Astrophysics (Cambridge University Press), 3–15

Motz, L. & Weaver, J. H. 1995, *The Story of Astronomy* (Plenum Press)

Shapiro, S. & Teukolsky, S. 1983, *Black Holes, White Dwarfs, and Neutron Stars* (John Wiley & Sons)

Tucker, W. & Giacconi, R. 1985, *X-Ray Universe* (Harvard University Press)

References for Chapter 2

Buck, R. & Lent, E. 1993, COG: A New, High-Resolution Code for Modeling Radiation Transport, *LLNL Energy and Technology Review*

Craig, W. W., Mclean, R., & Hailey, C. J. 1998, Sub-arcminute pointing from a balloon borne platform, *Proc. SPIE*, 3365, 87

Harrison, F. 1993, Development of a High Resolution Imaging Capability for Observing Cosmic Sources in the Hard X-ray/Soft Gamma-ray Band, PhD thesis, U.C. Berkeley

Hong, J. 2001, Development of Neutron Shields for Gamma-Ray Telescopes in Space and Observation of Hard X-ray Binary 4U 1700–377 by the Balloon-Borne Gamma-Ray Telescope, *GRATIS*, PhD thesis, Columbia University

Keck, J., Craig, W., Hailey, C., Hong, J., Kahn, S., McLean, R., Pivovaroff, M., Sprehn, G., Wurtz, R., Ziock, K., Jernigan, G., Harrison, F., Lubin, P., & Seiffert, M. 1996, Gamma-ray Background in the GRATIS Balloon-borne Payload, in *American Astronomical Society Meeting*, Vol. 189, 10110+

Shaw, J. A. 1996, The PID Control Algorithm (*www.jashaw.com/pid/description.htm*), World-wide Web

—. 2001, *johnshaw.terrashare.com/pid.html*, World-wide Web

Wilcox, T.P., J. & Lent, E. 1989, COG - A Particle Transport Code Designed to Solve the Boltzmann Equation for Deep-Penetration (Shielding) Problems. Vol. 1: User Manual, Tech. Rep. M-221-1, Lawrence Livermore National Laboratory

References for Chapter 3

Abramowitz, M. & Stegun, I. A. 1972, *Handbook of Mathematical Functions* (Dover)

Agrinier, B., Lavigne, J. M., & da Costa Ferreira Neri, J. A. 1992, Measurement of atmospheric and diffuse radiation using a time-of-flight telescope, *Journal of Geophysics Research*, 97, 1541

Ahluwalia, H. S. 1978, Long term changes in the parameters of cosmic ray daily harmonics, in *International Cosmic Ray Conference, 15th, Plovdiv, Bulgaria, August 13-26, 1977, Conference Papers. Volume 11. (A79-44583 19-93) Sofia, B'lgarska Akademiia na Naukite, 1978, p. 298-303.*, Vol. 11, 298–303

Ahluwalia, H. S. 1997, Galactic cosmic ray intensity variations at a high latitude sea level site 1937-1994, *Journal of Geophysics Research*, 102, 24229

Ait-Ouamer, F., Zych, A. D., & White, R. S. 1988, Atmospheric neutrons at 8.5-GV cutoff in the Southern Hemisphere, *Journal of Geophysics Research*, 93, 2499

Beuermann, K. P. 1971, Secondary Electrons and Photons in the Upper Atmosphere, *Journal of Geophysics Research*, 76, 4291

Butler, J. 1954, Machine Sampling from Given Probability Distributions, in *Symposium on Monte Carlo Methods*, ed. Meyer, H.A. (John Wiley & Sons Inc.), 249–264

Carpenter, G. & Dyer, C. 1973, Spectra of Radioactivity Induced in Caesium Iodide Scintillator Crystals by 155 MeV Protons, *Astrophysics and Space Science*, 24, 95

Costa, E., Massaro, E., Salvati, M., & Appolloni, A. 1984, An Approximate Analytical Representation of the Atmospheric Gamma-Ray Flux at Balloon Altitudes, *Astrophysics and Space Science*, 100, 165

Cranshaw, T. E. 1963, *Cosmic rays* (Clarendon Press: Oxford)

Daniel, R. & Stephens, S. 1974, Cosmic-Ray-Produced Electrons and Gamma Rays in the Atmosphere, *Reviews of Geophysics and Space Physics*, 12, 233

Dean, A., Lei, F., & Knight, P. 1991, Background in Space-borne Low-energy γ-ray Telescopes, *Space Science Reviews*, 57, 109

Duldig, M. L. 1994, Cosmic ray transient variations observed from the Earth, *Proceedings of the Astronomical Society of Australia*, 11, 110

Dvornikov, V. M., Sdobnov, V. E., Sergeev, A. V., Danilova, O. A., & Tyasto, M. I. 1985, Diurnal variations of cosmic ray geomagnetic cut-off threshold rigidities, in *5th International Cosmic Ray Conference*, Vol. 5, 359–362

Everett, C. J. & Cashwell, E. D. 1983, A Third Monte Carlo Sampler, Tech. Rep. LA-9721-MS, Los Alamos National Laboratory

Fichtel, C., Kniffen, D., & Ogelman, H. 1969, Results of Gamma-ray Balloon Astronomy, *Astrophysical Journal*, 158, 193

Gehrels, N. 1985, Instrumental Background in Balloon-borne Gamma-ray Spectrometers and Techniques for its Reduction, *Nuclear Instruments & Methods*, A239, 324

Graser, U. & Schönfelder, V. 1977, Theoretical Zenith Angle Distribution of Atmospheric MeV Gamma Radiation at High Balloon Altitudes, *Journal of Geophysics Research*, 82, 1055

Groom, D., Aguilar-Benitez, M., Amsler, C., Barnett, R., Burchat, P., Carone, C., Caso, C., Conforto, G., Dahl, O., Doser, M., Eidelman, S., Feng, J., Gibbons, L., Goodman, M., Grab, C., Gurtu, A., Hagiwara, K., Hayes, K., Hernández, J., Hikasa, K., Honscheid, K., Kolda, C., Mangano, M., Manohar, A., Masoni, A., Mönig, K., Murayama, H., Nakamura, K., Navas, S., Olive, K., Pape, L., Piepke, A., Roos, M., Tanabashi, M., Tornqvist, N., Trippe, T., Vogel, P., Wohl, C., Workman, R., & Yao, W.-M. 2000, Particle Data Review, *The European Physical Journal*, C15, 1+

Gruber, D., Jung, G., & Matteson, J. 1987, in *Conference on High Energy Radiation Background in Space*

Harrison, F. 1993, Development of a High Resolution Imaging Capability for Observing Cosmic Sources in the Hard X-ray/Soft Gamma-ray Band, PhD thesis, U.C. Berkeley

Harrison, F., Hailey, C., Hong, J., Wong, A.-S., & Cook, W. 2001, Background in Balloon-Borne Hard X-ray/Soft Gamma-ray Cadmium Zinc Telluride Detectors, *Nuclear Instruments & Methods*, 286, accepted

Hayakawa, S. 1969, *Cosmic ray physics. Nuclear and astrophysical aspects* (Interscience Monographs and Texts in Physics and Astronomy, New York: Wiley-Interscience, 1969)

Imhof, W., Nakano, G., & Reagan, J. 1976, High-Resolution Measurements of Atmospheric Gamma Rays From a Satellite, *Journal of Geophysics Research*, 81, 2835

Keck, J., Craig, W., Hailey, C., Hong, J., Kahn, S., McLean, R., Pivovaroff, M., Sprehn, G., Wurtz, R., Ziock, K., Jernigan, G., Harrison, F., Lubin, P., & Seiffert, M. 1996, Gamma-ray Background in the GRATIS Balloon-borne Payload, in *American Astronomical Society Meeting*, Vol. 189, 10110+

Kinzer, R., Johnson, W., & Kurfess, J. 1978, A Balloon Observation of the Diffuse Cosmic X-Radiation above 20 keV, *Astrophysical Journal*, 222, 370

Kinzer, R. L., Jung, G. V., Gruber, D. E., Matteson, J. L., & Peterson, L. E. 1997, Diffuse Cosmic Gamma Radiation Measured by HEAO 1, *Astrophysical Journal*, 475, 361+

Ling, J. 1974, Spectra and Angular-distributions of Low-energy Atmospheric Gamma-rays at the Geomagnetic Latitude Lambda = 40 Degrees, PhD thesis, U.C. San Diego

—. 1975, Semiempirical Model for Atmospheric γ Rays From 0.3 to 10 MeV at $\lambda = 40°$, *Journal of Geophysics Research*, 80, 3241

National Geophysical Data Center/NOAA. 1997, *ftp.ngdc.noaa.gov*, FTP Archive

Papini, P., Grimani, C., & Stephens, S. A. 1996, An estimate of the secondary-proton spectrum at small atmospheric depths, *Nuovo Cimento C Geophysics Space Physics C*, 19, 367

Peterson, L., Schwartz, D., & Ling, J. 1973, Spectrum of Atmospheric Gamma Rays to 10 MeV at $\lambda = 40°$, *Journal of Geophysics Research*, 78, 7942

Peterson, L. E., Jacobsen, A. S., Pelling, R. M., & Schwartz, R. M. 1968, Observations of cosmic X-ray sources in the 10–250 keV range, *Canadian Journal of Physics*, 46, S437

Ramsey, B. D., Bower, C. R., Dietz, K. L., & Weisskopf, M. C. 1990, The background in a balloon-borne fluorescence-gated proportional counter, *Proc. SPIE*, 1344, 82

Rubinstein, R. Y. 1981, *Simulation and the Monte Carlo Method* (John Wiley & Sons)

Ryan, J., Dayton, B., Moon, S., Wilson, R., Zych, A., & White, R. 1977, Atmospheric Gamma Ray Angle and Energy Distributions from Sea Level to 3.5 g/cm^2 and 2 to 25 MeV, *Journal of Geophysics Research*, 82, 3593

Ryan, J., Jennings, M., Radwin, M., Zych, A., & White, R. 1979, Atmospheric Gamma Ray Angle and Energy Distributions from Sea Level to 3.5 g/cm^2 and 2 to 25 MeV, *Journal of Geophysics Research*, 84, 5279

Schönfelder, V., Gaml, F., & Penningsfield, F.-P. 1980, The Vertical Component of 1–20 MeV Gamma Rays at Balloon Altitudes, *Astrophysical Journal*, 240, 350

Schönfelder, V., Graser, U., & Daugherty, J. 1977, Diffuse Cosmic and Atmospheric MeV Gamma Radiation from Balloon Observations, *Astrophysical Journal*, 217, 306

Shea, M. & Smart, D. 1975, A five by fifteen degree world grid of calculated cosmic-ray vertical cutoff rigidities for 1965 and 1975, in *14th International Cosmic Ray Conference*, 1298–1303

Thompson, D. 1974a, A Three-Dimensional Study of 30- to 300-MeV Atmospheric Gamma Rays, *Journal of Geophysics Research*, 79, 13090

—. 1974b, A Three-Dimensional Study of 30- to 300-MeV Atmospheric Gamma Rays, *Journal of Geophysics Research*, 79, 13090

Thompson, D. J., Simpson, G. A., & Özel, M. E. 1981, SAS 2 observations of the earth albedo gamma radiation above 35 MeV, *Journal of Geophysics Research*, 86, 1265

Valinia, A. & Marshall, F. E. 1998, RXTE Measurement of the Diffuse X-Ray Emission from the Galactic Ridge: Implications for the Energetics of the Interstellar Medium, *Astrophysical Journal*, 505, 134

White, R., Dayton, B., Moon, S., Ryan, J., Wilson, R., & Zych, A. 1977, Cosmic diffuse gamma rays from 2 to 25 MeV, *Astrophysical Journal*, 218, 920

White, R., O'Neill, T., Tumer, O., & Zych, A. 1988, The gamma ray north-south effect, *Journal of Geophysics Research*, 93, 14719

Yamasaki, N. Y., Ohashi, T., Takahara, F., Yamauchi, S., Koyama, K., Kamae, T., Kaneda, H., Makishima, K., Sekimoto, Y., Hirayama, M., Takahashi, T., Yamagami, T., Gunji, S., Tamura, T., Miyazaki, S., & Nomachi, M. 1997, Hard X-Ray Emission from the Galactic Ridge, *Astrophysical Journal*, 481, 821+

Zombeck, M. 1990, *Handbook of Space Astronomy and Astrophysics* (Cambridge University Press)

References for Chapter 4

Aleksandrovich, N. L., Borozdin, K. N., Emel'Yanov, A. N., Sunyaev, R. A., & Skinner, G. K. 1998, Upper limits on the fluxes from x-ray transients of the galactic-center region in the off state, *Astronomy Letters*, 24, 742

Barret, D., McClintock, J. E., & Grindlay, J. E. 1996, Luminosity Differences between Black Holes and Neutron Stars, *Astrophysical Journal*, 473, 963+

Bazzano, A., Cocchi, M., La Padula, C., Sood, R., & Ubertini, P. 1993, Hard X-ray observation of GRS 1758-258, *Astronomy & Astrophysics Supplement Series*, 97, 169

Grebenev, S. A., Pavlinsky, M. N., & Sunyaev, R. A. 1997, Hard X-ray sources 1E1740.7-2942, GRS1758-258 and SLX1735-269 in the Galactic center field, in *Proc. of the 2nd INTEGRAL Workshop "The Transparent Universe" (held in St. Malo, France, Sept. 16-20, 1996, eds. Winkler, C.; Courvoisier, T.; Durouchoux, Ph.), ESA SP-382, pp. 183-186*, 183–186

Gruber, D., Blanco, P., Heindl, W., Pelling, M., Rothschild, R., & Hink, P. 1996, The high energy X-ray timing experiment on XTE., *AAps*, 120, C641

Heindl, W. A. & Smith, D. M. 1998, The X-Ray Spectrum of SAX J1808.4-3658, *Astrophysical Journal*, 506, L35

Hjellming, R. 2000, priv. comm.

Hong, J. 2001, Development of Neutron Shields for Gamma-Ray Telescopes in Space and Observation of Hard X-ray Binary 4U 1700–377 by the Balloon-Borne Gamma-Ray Telescope, *GRATIS*, PhD thesis, Columbia University

Hong, J., Craig, W., Hailey, C., Keck, J., McLean, R., Pivovaroff, M., Ziock, K., Harrison, F., Lubin, P., & Seiffert, M. 2001, Hard X-ray Observations of 4U 1700–377 and Other Gamma-Ray Sources, *Astrophysical Journal*, in preparation

Iwan, D., Shafer, R., Marshall, F., Boldt, E., Mushotzky, R., & Stottlemyer, A. 1982, A large scale height galactic component of the diffuse 2-60 keV background, *Astrophysical Journal*, 260, 111

Jahoda, K., Swank, J., Giles, A., Stark, M., Strohmayer, T., Zhang, W., & Morgan, E. 1996, In-orbit performance and calibration of the Rossi X-ray Timing Explorer (RXTE) Proportional Counter Array (PCA), *Proc. SPIE*, 2808, 59

Johnson, W., Kinzer, R., Kurfess, J., Strickman, M., Purcell, W., Grabelsky, D., Ulmer, M., Hillis, D., Jung, G., & Cameron, R. 1993, The Oriented Scintillation Spectrometer Experiment - Instrument description, *Astrophysical Journal Supplement*, 86, 693

Jung, G., Kurfess, J., Johnson, W., Strickman, M., Kinzer, R., Purcell, W., Grabelsky, D., & Ulmer, M. 1993, OSSE Observations of the Galactic Center Region–Emission from Discrete Sources, in *The Second Compton Symposium: AIP Conference Proceedings*, ed. Fichtel, C. and Gehrels, N. and Norris, J.P., Vol. 304, 427–430

Keck, J., Craig, W., Hailey, C., Harrison, F., Hong, J., Kahn, S., Lubin, P., McLean, R., Pivovaroff, M., Seiffert, M., Wurtz, R., & Ziock, K. 2001, Long-term Multiwavelength Observations of GRS 1758–258, *Astrophysical Journal*, 477, submitted March 2001

Kuznetsov, S. I., Gilfanov, M. R., Churazov, E. M., Sunyaev, R. A., D'Yachkov, A. V., Khavenson, N. G., Novikov, B. S., Kremnev, R. S., Goldoni, P., Goldwurm, A., Laurent, P., Paul, J., Roques, J. ., Jourdain, E., Bouchet, L., & Vedrenne, G. 1999, Long-term variability of the hard X-ray source GRS 1758-258: GRANAT/SIGMA observations, *Astronomy Letters*, 25, 351

Levine, A., Bradt, H., Cui, W., Jernigan, J., Morgan, E., Remillard, R., Shirey, R., & Smith, D. 1996, First Results from the All-Sky Monitor on the Rossi X-Ray Timing Explorer, *Astrophysical Journal Letters*, 469, L33

Lin, D., Smith, I. A., Liang, E. P., Bridgman, T., Smith, D. M., Martí, J., Durouchoux, P., Mirabel, I. F., & Rodríguez, L. F. 2000, Simultaneous Observations of GRS 1758-258 in 1997 by VLA, IRAM, SEST, RXTE, and OSSE: Spectroscopy and Timing, *Astrophysical Journal*, 532, 548

Main, D. S., Smith, D. M., Heindl, W. A., Swank, J., Leventhal, M., Mirabel, I. F., & Rodríguez, L. F. 1999, Long-Term X-Ray Monitoring of 1E 1740.7-2942 and GRS 1758-258, *Astrophysical Journal*, 525, 901

Maisack, M., Kendziorra, E., Kretschmar, P., Kunz, M., Staubert, R., Döbereiner, S., Pietsch, W., Reppin, C., Efremov, V., Kaniovsky, S., & Sunyaev, R. 1993, HEXE Observations 1991/1992, in *The Second Compton Symposium: AIP Conference Proceedings*, ed. Fichtel, C. and Gehrels, N. and Norris, J.P., Vol. 304, 451–455

Mandrou, P. 1990, Galactic Center, *IAU Circular*, 5032, 1+

Martí, J. 1993, Radio emitting X-ray binaries, PhD thesis, , University of Barcelona, (1993)

—. 2000, priv. comm.

Martí, J., Mereghetti, S., Chaty, S., Mirabel, I. F., Goldoni, P., & Rodríguez, L. F. 1998, Search for the optical and infrared counterpart of GRS 1758-258, *Astronomy & Astrophysics*, 338, L95

Mereghetti, S., Belloni, T., & Goldwurm, A. 1994, Evidence for a soft X-ray excess in the spectrum of GRS 1758-258, *Astrophysical Journal*, 433, L21

Mereghetti, S., Cremonesi, D. I., Haardt, F., Murakami, T., Belloni, T., & Goldwurm, A. 1997, ASCA Observations of the Galactic Bulge Hard X-Ray Source GRS 1758-258, *Astrophysical Journal*, 476, 829+

Mirabel, I. F., Cordier, B., Paul, J., Lebrun, F., & Duc, P. A. 1992, Galactic Center, *IAU Circular*, 5655, 1+

Mirabel, I. F. & Rodríguez, L. F. 1993, Time variations in the Radio Emissions from 1E1740.7-2942 and GRS1758-258, in *The Second Compton Symposium: AIP Conference Proceedings*, ed. Fichtel, C. and Gehrels, N. and Norris, J.P., Vol. 304, 413–420

Pfeffermann, E. & Briel, U. 1986, Performance of the position sensitive proportional counter of the ROSAT telescope, *Proc. SPIE*, 597, 208

Predehl, P. & Schmitt, J. H. M. M. 1995, X-raying the interstellar medium: ROSAT observations of dust scattering halos., *Astronomy & Astrophysics*, 293, 889

Rodríguez, L. F., Mirabel, I. F., & Martí, J. 1992, The radio counterpart of the hard X-ray source GRS 1758-258, *Astrophysical Journal*, 401, L15

Roques, J., Mandrou, P., Paul, J., & Lebrun, F. 1990, The Sigma mission on the GRANAT satellite, *Advances in Space Research*, 10, 223

Rothschild, R., Blanco, P., Gruber, D., Heindl, W., MacDonald, D., Marsden, D., Pelling, M., Wayne, L., & Hink, P. 1998, In-Flight Performance of the High-Energy X-Ray Timing Experiment on the Rossi X-Ray Timing Explorer, *Astrophysical Journal*, 496, 538+

Skinner, G. 1990, The Position of GRS1758-258, in *Gamma-ray Line Astrophysics: AIP Conference Proceedings*, ed. P. Durouchoux & N. Prantzos, Vol. 232, 358–360

Skinner, G., Harper, P., Herring, J., & Ramsey, B. 1988, The Spacelab 2 XRT Xenon-filled Position-sensitive Proportional Counter, *Nuclear Instruments & Methods*, 273, 682

Sunyaev, R., Babichenko, S., Goganov, D., Tabaldyev, S., & Iamburenko, N. 1990a, X-ray telescopes ART-P and ART-S for the GRANAT project, *Advances in Space Research*, 10, 233

Sunyaev, R., Churazov, E., Gilfanov, M., Pavlinsky, M., Grebenev, S., Dekhanov, I., Kuznetsov, A., Yamburenko, N., Ballet, J., Laurent, P., Paul, J., Salotti, L., Natalucci, L., Niel, M., Roques, J., & Mandrou, P. 1990b, GRANAT Images of the Galactic Center Region in 4-1300 keV Band: Locaization of the Possible Candidate for the 511 keV Source, in *Gamma-ray Line Astrophysics: AIP Conference Proceedings*, ed. P. Durouchoux & N. Prantzos, Vol. 232, 29–41

Turner, M., Smith, A., & Zimmermann, H. 1981, The medium energy instrument on Exosat, *Space Science Reviews*, 30, 513

Valinia, A. & Marshall, F. 1998, RXTE Measurement of the Diffuse X-Ray Emission from the Galactic Ridge: Implications for the Energetics of the Interstellar Medium, *Astrophysical Journal*, 505, 134

Zombeck, M., David, L., Harnden, F., & Kearns, K. 1995, Orbital performance of the high-resolution imager (HRI) on ROSAT, *Proc. SPIE*, 2518, 304

References for Chapter 5

Barret, D., McClintock, J. E., & Grindlay, J. E. 1996, Luminosity Differences between Black Holes and Neutron Stars, *Astrophysical Journal*, 473, 963+

Belloni, T., Méndez, M., van der Klis, M., Hasinger, G., Lewin, W., & van Paradijs, J. 1996, An Intermediate State of Cygnus X-1, *Astrophysical Journal Letters*, 472, L107

Belloni, T., Méndez, M., van der Klis, M., Lewin, W., & Dieters, S. 1999, A State Transition of GX 339-4 Observed with the Rossi X-Ray Timing Explorer, *Astrophysical Journal Letters*, 519, L159

Belloni, T., van der Klis, M., Lewin, W., van Paradijs, J., Dotani, T., Mitsuda, K., & Miyamoto, S. 1997, Energy dependence in the quasi-periodic oscillations and noise of black hole candidates in the very high state., *Astronomy & Astrophysics*, 322, 857

Bevington, P. R. & Robinson, D. K. 1992, *Data Reduction and Error Analysis for the Physical Sciences* (McGraw-Hill, Inc.)

Braes, L. & Miley, G. 1976, Another correlated X-ray-radio transition in Cygnus X-1, *Nature*, 264, 731+

Corbel, S., Fender, R., Tzioumis, A., Nowak, M., McIntyre, V., Durouchoux, P., & Sood, R. 2000, Coupling of the X-ray and radio emission in the black hole candidate and compact jet source GX 339-4, *Astronomy & Astrophysics*, 359, 251

Ebisawa, K., Ogawa, M., Aoki, T., Dotani, T., Takizawa, M., Tanaka, Y., Yoshida, K., Miyamoto, S., Iga, S., Hayashida, K., Kitamoto, S., & Terada, K. 1994, Spectral evolution of the bright X-ray nova GS 1124-68 (Nova MUSCAE 1991) observed with GINGA, *Proc. Astron. Soc. Japan*, 46, 375

Fender, R., Corbel, S., Tzioumis, T., McIntyre, V., Campbell-Wilson, D., Nowak, M., Sood, R., Hunstead, R., Harmon, A., Durouchoux, P., & Heindl, W. 1999, Quenching of the Radio Jet during the X-Ray High State of GX 339-4, *Astrophysical Journal Letters*, 519, L165

Grebenev, S. A., Sunyaev, R. A., & Pavlinsky, M. N. 1997, Spectral states of galactic black hole candidates: results of observations with ART-P/Granat, *Advances in Space Research*, 19, 15

Hannikainen, D., Hunstead, R., & Campbell-Wilson, D. 1998, MOST radio observations of GX 339/-4, GRS 1915+105 and GRO J1655/-40, *New Astronomy Review*, 42, 601

Harmon, B., Deal, K., Paciesas, W., Zhang, S., Robinson, C., Gerard, E., Rodriguez, L., & Mirabel, I. 1997, Hard X-Ray Signature of Plasma Ejection in the Galactic Jet Source GRS 1915+105, *Astrophysical Journal Letters*, 477, L85

Heindl, W. A. & Smith, D. M. 1998, The X-Ray Spectrum of SAX J1808.4-3658, *Astrophysical Journal*, 506, L35

Hjellming, R. 1973, Radio Variability of HDE 226868 (Cygnus X-1), *Astrophysical Journal Letters*, 182, L29

—. 2000, priv. comm.

Hjellming, R. & Han, X. 1995, Radio properties of X-ray binaries, in *X-Ray Binaries*, ed. W. Lewin, J. van Paradijs, & E. van den Heuvel (Cambridge University Press), 308–330

Liang, E. 1998, Multi-wavelength signatures of galactic black holes : observation and theory., *Phys. Rep.*, 302, 67

Lin, D., Smith, I. A., Böttcher, M., & Liang, E. P. 2000a, The Energy Dependence of the Aperiodic Variability for Cygnus X-1, GX 339-4, GRS 1758-258, and 1E 1740.7-2942, *Astrophysical Journal*, 531, 963

Lin, D., Smith, I. A., Liang, E. P., Bridgman, T., Smith, D. M., Martí, J., Durouchoux, P., Mirabel, I. F., & Rodríguez, L. F. 2000b, Simultaneous Observations of GRS 1758-258 in 1997 by VLA, IRAM, SEST, RXTE, and OSSE: Spectroscopy and Timing, *Astrophysical Journal*, 532, 548

Martí, J. 1993, Radio emitting X-ray binaries, PhD thesis, , University of Barcelona, (1993)

McCollough, M., Robinson, C., Zhang, S., Harmon, B., Hjellming, R., Waltman, E., Foster, R., Ghigo, F., Briggs, M., Pendleton, G., & Johnston, K. 1999, Discovery of Correlated Behavior between the Hard X-Ray and the Radio Bands in Cygnus X-3, *Astrophysical Journal*, 517, 951

Méndez, M. & van der Klis, M. 1997, The EXOSAT Data on GX 339-4: Further Evidence for an "Intermediate" State, *Astrophysical Journal*, 479, 926+

Mereghetti, S., Belloni, T., & Goldwurm, A. 1994, Evidence for a soft X-ray excess in the spectrum of GRS 1758-258, *Astrophysical Journal*, 433, L21

Mereghetti, S., Cremonesi, D. I., Haardt, F., Murakami, T., Belloni, T., & Goldwurm, A. 1997, ASCA Observations of the Galactic Bulge Hard X-Ray Source GRS 1758-258, *Astrophysical Journal*, 476, 829+

Smith, D. M., Heindl, W. A., & Swank, J. H. 1999, GRS 1758-258, *IAU Circular*, 7266, 2+

Tanaka, Y. & Lewin, W. H. 1995, Black-hole Binaries, in *X-Ray Binaries*, ed. W. Lewin, J. van Paradijs, & E. van den Heuvel (Cambridge University Press), 126–164

Tananbaum, H., Gursky, H., Kellogg, E., Giacconi, R., & Jones, C. 1972, Observation of a Correlated X-Ray Transition in Cygnus X-1, *Astrophysical Journal Letters*, 177, L5

Zhang, S., Cui, W., Harmon, B., Paciesas, W., Remillard, R., & van Paradijs, J. 1997a, The 1996 Soft State Transition of Cygnus X-1, *Astrophysical Journal Letters*, 477, L95

Zhang, S., Mirabel, I., Harmon, B. A., Kroeger, R., Rodríguez, L., Hjellming, R., & Rupen, M. 1997b, Galactic Black Hole Binaries: Multifrequency Connections, in *Proceedings of the Fourth Compton Symposium*, ed. C. Dermer, M. Strickman, & J. Kurfess (American Institute of Physics), 141–162

References for Chapter 6

Abramowicz, M., Chen, X., Kato, S., Lasota, J., & Regev, O. 1995, Thermal equilibria of accretion disks, *Astrophysical Journal Letters*, 438, L37

Agol, E. 2000, Sagittarius A* Polarization: No Advection-dominated Accretion Flow, Low Accretion Rate, and Nonthermal Synchrotron Emission, *Astrophysical Journal Letters*, 538, L121

Barret, D., McClintock, J. E., & Grindlay, J. E. 1996, Luminosity Differences between Black Holes and Neutron Stars, *Astrophysical Journal*, 473, 963+

Barret, D., Olive, J., Boirin, L., Done, C., Skinner, G., & Grindlay, J. 2000, Hard X-Ray Emission from Low-Mass X-Ray Binaries, *Astrophysical Journal*, 533, 329

Belloni, T., Méndez, M., van der Klis, M., Lewin, W., & Dieters, S. 1999, A State Transition of GX 339-4 Observed with the Rossi X-Ray Timing Explorer, *Astrophysical Journal Letters*, 519, L159

Bisnovatyi-Kogan, G. & Blinnikov, S. 1977, Disk accretion onto a black hole at subcritical luminosity, *Astronomy & Astrophysics*, 59, 111

Blandford, R. D. & Begelman, M. C. 1999, On the fate of gas accreting at a low rate on to a black hole, *Monthly Notices of the Royal Astronomical Society*, 303, L1

Böttcher, M. & Liang, E. 1998, Comptonization Signatures in the Rapid Aperiodic Variability of Galactic Black Hole Candidates, *Astrophysical Journal*, 506, 281

Chen, W., Gehrels, N., & Leventhal, M. 1994, On the optical counterparts, long-term variabilities, radio jets, and accretion sources in 1E 1740.7-2942 and GRS 1758-258, *Astrophysical Journal*, 426, 586

Cowley, A., Crampton, D., & Hutchings, J. 1987, GX 339-4 - Black hole or neutron star X-ray binary?, *Astronomical Journal*, 93, 195

Esin, A., McClintock, J., & Narayan, R. 1997, Advection-dominated Accretion and the Spectral States of Black Hole X-Ray Binaries: Application to Nova MUSCAE 1991, *Astrophysical Journal*, 489, 865+

Esin, A., Narayan, R., Cui, W., Grove, J., & Zhang, S. 1998, Spectral Transitions in Cygnus X-1 and Other Black Hole X-Ray Binaries, *Astrophysical Journal*, 505, 854

Filippenko, A., Leonard, D., Matheson, T., Li, W., Moran, E., & Riess, A. 1999, A Black Hole in the X-Ray Nova Velorum 1993, *Proc. Astron. Soc. Pacific*, 111, 969

Gilfanov, M., Churazov, E., Sunyaev, R., Khavenson, N., Novikov, B., Dyachkov, A., Kremnev, R., Sukhanov, K., Bouchet, L., Mandrou, P., Roques, J. P., Vedrenne, G., Cordier, B., Goldwurm, A., Laurent, P., & Paul, J. 1993, Three Years of Monitoring GRS 1758-258: an Extremely Hard X-Ray Source near GX 5-1, *Astrophysical Journal*, 418, 844+

Grindlay, J., Bildsten, L., Chakrabarty, D., Elvis, M., Fabian, A., Fiore, F., Gehrels, N., Hailey, C., Harrison, F., Hartmann, D., Prince, T., Ramsey, B., Rothschild, R., Skinner, G., & Woosley, S. 2000, EXIST: A High Sensitivity Hard X-ray Imagining Survey Mission for ISS, in *Proceedings of the Fifth Compton Symposium*, ed. M. L. McConnell & J. M. Ryan (American Institute of Physics), 141–162

Grindlay, J. & EXIST Science Working Group. 2000, Proposed to EXIST: Deep Hard X-ray Imaging All Sky Survey, *AAS/High Energy Astrophysics Division*, 32, 2004+

Honma, F., Kato, S., Matsumoto, R., & Abramowicz, M. 1991, Stability of slim, transonic accretion disk models, *Proc. Astron. Soc. Japan*, 43, 261

Hua, X. & Titarchuk, L. 1995, Comptonization Models and Spectroscopy of X-Ray and Gamma-Ray Sources: A Combined Study by Monte Carlo and Analytical Methods, *Astrophysical Journal*, 449, 188+

Ichimaru, S. 1977, Bimodal behavior of accretion disks - Theory and application to Cygnus X-1 transitions, *Astrophysical Journal*, 214, 840

Igumenshchev, I., Abramowicz, M., & Narayan, R. 2000, Numerical Simulations of Convective Accretion Flows in Three Dimensions, *Astrophysical Journal Letters*, 537, L27

Kuznetsov, S. I., Gilfanov, M. R., Churazov, E. M., Sunyaev, R. A., D'Yachkov, A. V., Khavenson, N. G., Novikov, B. S., Kremnev, R. S., Goldoni, P., Goldwurm, A., Laurent, P., Paul, J., Roques, J. ., Jourdain, E., Bouchet, L., & Vedrenne, G. 1999,

Long-term variability of the hard X-ray source GRS 1758-258: GRANAT/SIGMA observations, *Astronomy Letters*, 25, 351

Liang, E. 1998, Multi-wavelength signatures of galactic black holes : observation and theory., *Phys. Rep.*, 302, 67

Liang, E. & Price, R. 1977, Accretion disk coronae and Cygnus X-1, *Astrophysical Journal*, 218, 247

Lin, D., Smith, I. A., Böttcher, M., & Liang, E. P. 2000a, The Energy Dependence of the Aperiodic Variability for Cygnus X-1, GX 339-4, GRS 1758-258, and 1E 1740.7-2942, *Astrophysical Journal*, 531, 963

Lin, D., Smith, I. A., Liang, E. P., Bridgman, T., Smith, D. M., Martí, J., Durouchoux, P., Mirabel, I. F., & Rodríguez, L. F. 2000b, Simultaneous Observations of GRS 1758-258 in 1997 by VLA, IRAM, SEST, RXTE, and OSSE: Spectroscopy and Timing, *Astrophysical Journal*, 532, 548

Maccarone, T. J. & Coppi, P. S. 2001, On the Discovery of Soft Time Lags in the Very High State of XTE J 1748-2848, *Astrophysical Journal Letters*, submitted

Méndez, M. & van der Klis, M. 1997, The EXOSAT Data on GX 339-4: Further Evidence for an "Intermediate" State, *Astrophysical Journal*, 479, 926+

Miyamoto, S., Iga, S., Kitamoto, S., & Kamado, Y. 1993, Another canonical time variation of X-rays from black hole candidates in the very high flare state?, *Astrophysical Journal Letters*, 403, L39

Narayan, R., Garcia, M., & McClintock, J. 1997, Advection-dominated Accretion and Black Hole Event Horizons, *Astrophysical Journal Letters*, 478, L79

Narayan, R., Igumenshchev, I., & Abramowicz, M. 2000, Self-similar Accretion Flows with Convection, *Astrophysical Journal*, 539, 798

Narayan, R. & Yi, I. 1994, Advection-dominated accretion: A self-similar solution, *Astrophysical Journal Letters*, 428, L13

—. 1995, Advection-dominated Accretion: Underfed Black Holes and Neutron Stars, *Astrophysical Journal*, 452, 710+

Quataert, E. & Gruzinov, A. 2000, Convection-dominated Accretion Flows, *Astrophysical Journal*, 539, 809

Shapiro, S., Lightman, A., & Eardley, D. 1976, A two-temperature accretion disk model for Cygnus X-1 - Structure and spectrum, *Astrophysical Journal*, 204, 187

Titarchuk, L. 1994, Generalized Comptonization models and application to the recent high-energy observations, *Astrophysical Journal*, 434, 570

Zhang, S., Mirabel, I., Harmon, B. A., Kroeger, R., Rodríguez, L., Hjellming, R., & Rupen, M. 1997, Galactic Black Hole Binaries: Multifrequency Connections, in *Proceedings of the Fourth Compton Symposium*, ed. C. Dermer, M. Strickman, & J. Kurfess (American Institute of Physics), 141–162

Życki, P., Done, C., & Smith, D. 1997, Relativistically Smeared X-Ray Reprocessed Components in the GINGA Spectra of GS 2023+338, *Astrophysical Journal Letters*, 488, L113

Appendix A

Monte Carlo Simulations

We simulated the high-energy photon environment of *GRATIS* using the COG Monte Carlo code developed at Lawrence Livermore National Laboratory (Buck & Lent, 1993; Wilcox & Lent, 1989). We used version 8.0 and followed only photons, not neutrons. (Electrons are produced but not followed.) We set the option for electron-positron pair-production to result in two annihilation gammas that are transported, and for bremsstrahlung to be produced.

The COG code allows the user to specify an arbitrary three-dimensional geometry for a problem via an ASCII input file. To compose our input file, we measured the important dimensions of the *GRATIS* payload and entered these as variables into an IDL procedure. Specifying *GRATIS*'s dimensions as variables allowed us more easily to alter input files as we refined our knowledge of *GRATIS*'s geometry. The IDL procedure, `make_gratis.pro`, performed the calculations and converted the dimensions of *GRATIS* into the COG input file that specifies the source, the pseudo-surfaces that bound that various sections of *GRATIS*, and the materials that compose each section.

COG provides a few common source specifications, but also allows the user to write his own source routines. Our FORTRAN code for the cosmic diffuse gamma-ray source is `CDGSo.F`, and `AtmBGSo.F` is our code for simulating atmospheric background.

COG's standard output provides very little information about the direction and origin of each detected photon. Fortunately COG allows the user to define his own detector routines, as we have done with `astrodet.F`, to provide more comprehensive output:

`t`	= detector (region) number
`x,y,z`	= location of last interaction in detector
`e`	= energy deposited in detector
`e1`	= energy of photon before entering crystal
`wate`	= statistical weight of photon
`theta1,phi1`	= direction angles of photon before entering crystal
`noc1`	= number of collisions before entering crystal
`x0,y0,z0`	= origin of photon
`e0`	= original energy of photon
`theta0,phi0`	= original direction angles of photon
`seq`	= sequence number of source photon

We turn to the COG mock-up of *GRATIS* and the results of the Monte Carlo simulations.

A.1 The COG version of *GRATIS*

We incorporated into the COG model all of the lead, tin, and copper elements of the telescope, as well as the thicker aluminum elements, such as the walls of the pressure vessel. We also included the aluminum window on the crystal because of its proximity to the detecting crystal. Figure A.1 shows a cross section from the side of the detector shields.

For background models, we simplified the geometry to fit it within a 40-cm-radius sphere. Thus we could only include one detector and its fine collimator, as depicted in the figure.

Figure A.1: Cross-sectional views of COG model of *GRATIS* tube shielding and fine collimator assembly. Inset are two views taken from cross-sections perpendicular to the main image. The coordinates refer to the tube's coordinates, which are identical to the problem coordinates only for tube 19 (cf. figure 2.4, p. 15).